Open Sea Operating Experience to Reduce Wave Energy Costs

Deliverable D4.2

Shoreline OWC wave power plant control algorithms

Lead Beneficiary	TECNALIA
Delivery date	2018-07-27
Dissemination level	Public
Status	Approved
Version	1.0
Keywords	Wave energy, OWC, PTO control, algorithm, Mutriku

This project has received funding from the European Union's Horizon 2020 research and innovation programme under grant agreement No 654444

Disclaimer

This Deliverable reflects only the author's views and the Agency is not responsible for any use that may be made of the information contained therein

Document Information

Grant Agreement Number	654444
Project Acronym	OPERA
Work Package	WP4
Task(s)	T4.3
Deliverable	D4.2
Title	Shoreline OWC wave power plant control algorithms
Author(s)	François-Xavier Faÿ, Ainhoa Pujana, Pablo Ruiz-Minguela (Tecnalia), James Kelly (UCC), Markus Mueller (EXE), João Henriques, Luís Gato, Ana Carrelhas, Bárbara Lopes (IST), Endika Aldaiturriaga (Oceantec)
File Name	OPERA_D4.2_Shoreline OWC wave power plant control algorithms_v1_IST_20180809_APG3.docx

Change Record

Revision	Date	Description	Reviewer
0.1	17-05-2018	Initial outline	Tecnalia
0.2	06-06-2018	First draft	WP4 partners
0.5	11-07-2018	Draft for peer review	David Crooks (UEDIN)
1.0	10-08-2018	Reviewed version for submission	EC

EXECUTIVE SUMMARY

The main objective of WP4 is the implementation at sea of innovative algorithms for controlling the Power Take Off (PTO) of wave energy converters that would increase the power production and device reliability. This will lead to a decrease of the LCOE, improving so wave energy prospects.

This goal has been realised through the implementation and testing six (CL1 – CL6) of seven dedicated control laws (CLs) summarised in Table 1 in the shoreline Mutriku Wave Power Plant. All were previously validated through simulations and dry-lab tests. Unfortunately, the validation of the CL7 has not been possible because it requires a more accurate estimation of the incoming waves than available. The conversion of energy in this installation is made by means of oscillating water column technology, using the novel biradial air turbine developed in WP3.

TABLE 1. SUMMARY OF CONTROL LAWS

Control Law #	Partner	Adaptive/ Predictive	Controls …	Based on …
CL1	IST	Adaptive	Generator torque	Rotational speed
CL2	UCC	Adaptive	Generator torque	Chamber pressure
CL3	UCC	Adaptive	PTO damping, valve open-close timings	Hourly sea-state data
CL4	IST	Adaptive	Valve open-close timings and position	Rotational speed, chamber pressure and valve position
CL5	UNEXE	Adaptive	Generator torque	Next wave information + output power+ rotational speed
CL6	TEC	Predictive	Generator torque	Water column motion in the chamber (position and speed) Pressure in chamber Turbine speed Wave elevation in front of the plant
CL7	IST	Predictive	Valve open-close timings and position	12-24 sec future wave information, rotational speed and chamber pressure and valve position

The controllers are classified into two main families: adaptive controllers use operational data to decide the best instantaneous control action and predictive controllers that perform an online optimisation along with a prediction horizon and have the capacity to adapt to the

incoming waves. Apart from the adaptive/predictive classification, two kinds of control strategies are identified; turbine speed control that sets the PTO at its optimum efficiency point, and the latching mechanism that aims to modify the WEC motion to force resonance conditions with incident waves to maximise resource conversion.

Each CL has been implemented at the Mutriku power plant except CL7. The tested control laws operated alternatively in intervals of 30 min, achieving so the first implementation at-sea of latching and predictive controls. Operational data have been collected and analysed to offer a comparison between each CL, focused on performance, reliability and power quality.

Finally, the best in class adaptive control was found to be CL2 which increased the production by more than 20% regarding the base case CL1. Though it operated in few sea states, the predictive version of CL6 produced over 30% more electrical power than the base case and seem to be promising for the next project phase. When focusing on PTO efficiency, CL1 showed the best turbine efficiency, but its global performance was compromised because it was configured to reduce the number of operations of the high-speed safety valve (HSSV) until generator rated power is reached. Above this threshold, CL1 relies on the HSSV for safe operation. However, this CL offered the best results regarding power quality due to the use of the rotational kinetic energy storage (flywheel effect) and peak-power limitation.

The turbine performance results obtained at the Mutriku power plant should be analysed carefully since they are biased. The turbine diameter was optimised for the Oceantec's buoy and not for Mutriku plant. As such, the pneumatic power available to the turbine at Mutriku is far from optimal.

Another round of tests is expected to happen in Oceantec's buoy located in BiMEP, where the biradial turbine will continue its sea trials. This will give the opportunity to test further the control algorithm and this time in a floating device, where the latching algorithms are expected to operate better than in the Mutriku plant.

TABLE OF CONTENTS

LIST OF FIGURES

LIST OF TABLES

ABBREVIATIONS AND ACRONYMS

B2B: Back-to-Back power converter
DB: Database
DG: Discontinuous Galerkin
EIRF: Excitation Impulse Response Function
HSSV: High-Speed Safety Valve
MPC: Model Predictive Control
MWPP: Mutriku Wave Power Plant
OWC: Oscillating Water Column
Pk2avg: Peak-to-Average power ratio
PMP: Pontryagin's Maximum Principle
PTO: Power Take Off
RL: Reinforcement Learning
SS: Sea State
VSI: Voltage Source Inverter
W2W: Wave-to-Wire
WEC: Wave Energy Converter
WP: Work Package
YK: Yokogawa power analyser

1. INTRODUCTION

In line with the objectives of work package 4 (WP4) under the framework of the H2020 OPERA project, the Mutriku Wave Power Plant has been used as a real-world laboratory for the first implementation of advanced algorithms for controlling the innovative biradial turbine developed in WP3. Mutriku Wave Power Plant (MWPP) is a facility located in the Bay of Biscay that converts wave energy by means of oscillating water column technology. Prior to this first sea trials and with the objective of de-risking innovative technologies, the controllers' performance was assessed using numerical simulation via a Wave-to-Wire (W2W) model describing one chamber of the Mutriku Oscillating Water Column (OWC) plant. Besides, after numerical simulations, 6 CLs (CL1 – CL6) were implemented in one of the two electrical dry-test infrastructures hosted by the partners' project.

In total, 6 out of 7 control algorithms have been validated, grouped in two main families: adaptive controllers and predictive controllers. The adaptive controls use operational data of the plant to decide the best instantaneous control action, whereas the predictive strategies perform an on-line optimisation along with a prediction horizon. Apart from the adaptive/predictive distinction, two kinds of control strategies are identified; the turbine speed control acts to set the Power Take Off (PTO) to its best efficiency point, and the latching control aims to modify the in-sea WEC (Wave Energy Converter) hydrodynamics in order to force resonance conditions with the incident waves.

Tests in MWPP have been carried out from July 2017 to June 2018, collecting so 12 months of operational data.

The deliverable is structured in several parts. Section 2 describes the Mutriku Wave Power Plant, starting with the available wave resource. Then, the dynamics of the air chamber where the power take-off system is described including the biradial turbine. Section 3 describes the 7 CLs, detailing the implementation requirements. Section 4 details the measurements carried out during the tests, as well as the database where they have been collected. Section 5 gives information about the methodology followed during the testing along with its chronology. Section 0 summarises the analysis of testing results, as well as a quantitative and qualitative comparison of their performance. In order to facilitate the comparison of the CLs, CL1 has been used as "base control" benchmark. An evaluation table has also been included to have a common criterion for comparison. Recommendations based on lessons learnt during the testing period at the Mutriku plant are given in Section 7.

2. MUTRIKU WAVE ENERGY PLANT

The wave energy plant at Mutriku [1]–[3] is hosted inside the breakwater that protects its harbour, in the Bay of Biscay. Its design includes a hollow structure forming a trapezium shape which contains 16 air chambers, with OWC being the technology used for the energy conversion. One of these chambers, number 9, has been used in OPERA project to test the novel turbine-generator set developed in WP3, as well as the advanced algorithms that control its operation.

2.1 WAVE RESOURCE

Mutriku Wave Power Plant is producing energy in a local wave climate. Sections 2.1.1 to 2.1.3 describe the elements that were used to measure and estimate the wave resource during the testing of the advanced CLs.

2.1.1 PRESSURE GAUGE WITH DATA LOGGER (RBR/*VIRTUOSO*)

The RBRvirtuoso [4], supplied by RBR, has been found as the best sensor for resource measurement according to the project requirements and constraints. It is small and robust and can be positioned in a relatively protected part of the seabed (e.g. between rocks) sheltered from wave action without any impact on performance. The pressure sensor was selected as the best compromise between accuracy, cost of operation, deployment and survivability capabilities to the harsh Winter season [5]. The uncertainties related to the computation of the wave elevation from the hydrostatic pressure are discussed in Annex 8.2

FIGURE 1. RBR VIRTUOSO OFF-LINE PRESSURE SENSOR

This pressure gauge was installed in November 2016 (see Figure 1), 200 m in front chamber #9, following the most frequent wave direction, in a depth of around 15 m. It was removed in May 2017 to collect the data along this 6 months deployment. However, it was discovered a

leakage in the battery happened in February leaving only three months and a half of viable data. After its repair, and due to the hard conditions of winter, it was not possible to reinstall it until late January 2018. In June 2018, it was removed again for data collection and reinstalled immediately (see Figure 1). A total of 8 months of data was registered during when 2.5 months covers the testing period.

2.1.2 PRESSURE GAUGE WITH REAL-TIME COMMUNICATION

The CNC4200-MT3 [6], supplied by ISURKI, is based on a ceramic die and measures the hydrostatic pressure through a capacitive effect. A vented tube inside the cable assures the compensation of the atmospheric pressure variations. There is a subsea cable that connects it with the Mutriku Wave Power Plant as it can be seen in Figure 2.

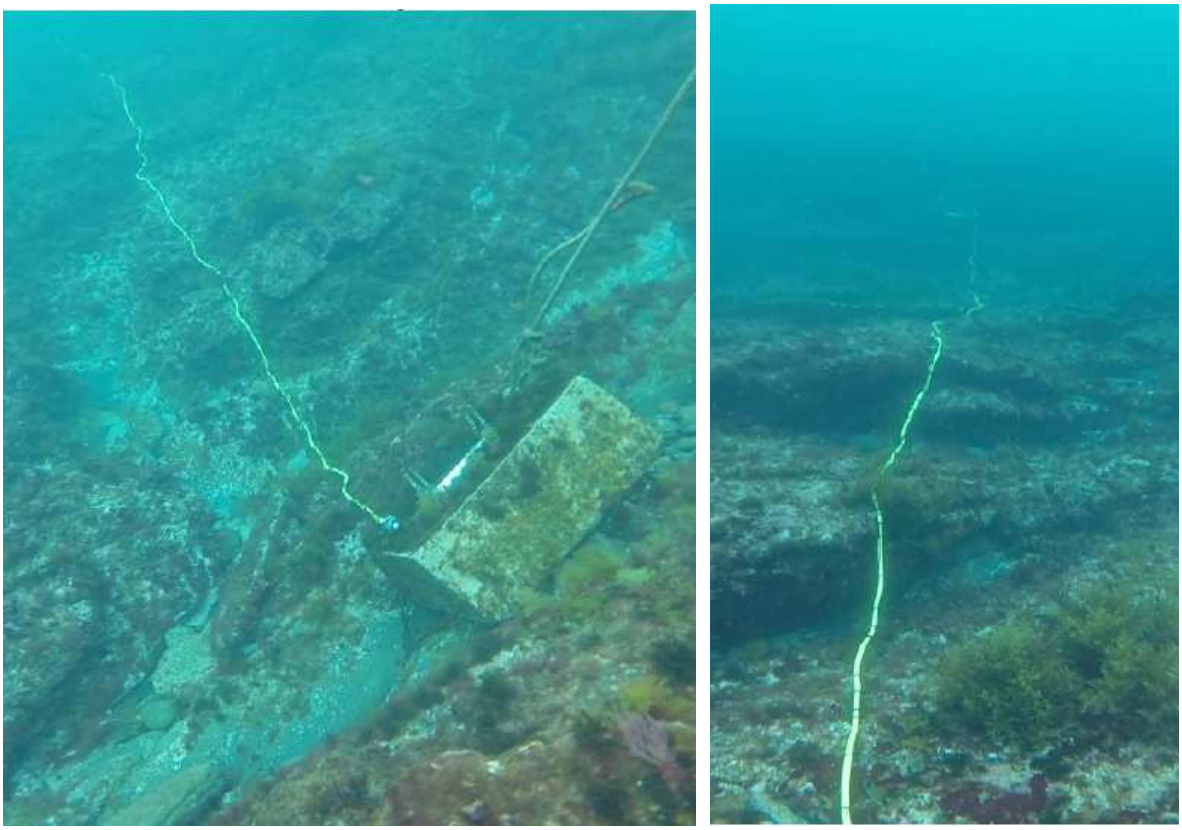

FIGURE 2. CNC4200 AND COMMUNICATION CABLE INSTALLED AT SUBSEA

The installation of this pressure gauge was delayed due to the bad weather conditions happened during winter. It was installed in May 2018, 200 m offshore in a depth of around 15 m.

2.1.3 ESTIMATION FROM SIMAR POINTS

For the control law tests in which none of the sensors was available, the wave data was obtained using a "Punto SIMAR 3171032" (the closest to Mutriku) [7], and the tidal elevation was taken from "Mareografo BILBAO 3". It is an estimate of the wave climate made by the institution *Puertos del estado* given by a propagation model.

2.2 AIR CHAMBER

The main parameters related with the air chamber N.9 where the tests have been carried out are shown in Table 1.

TABLE 1. CHARACTERISTICS OF THE MUTIKU POWER PLANT

Parameters	Symbol	Value	Unit
Physical quantities			
Water density	$\boldsymbol{\rho_w}$	1025	kg/m^3
Reference atmospheric air density	$\boldsymbol{\rho_{at}}$	1.25	kg/m^3
Gravitational constant	$\boldsymbol{g}$	9.81	m/s^2
Reference atmospheric pressure	$\boldsymbol{p_{at}}$	101.5	kPa
Specific heat ratio	$\boldsymbol{\gamma}$	1.40	-
Plant dimensions			
Chamber width	$\boldsymbol{w_{ch}}$	4.50	m
Chamber length	$\boldsymbol{l_{ch}}$	3.10	m
Chamber height at the mean tide	$\boldsymbol{h_{ch}}$	7.45	m
Minimum height (maximum astronomical tide)		5.20	m
Maximum height (minimum astronomical tide)		9.70	m

2.3 POWER TAKE-OFF SYSTEM

2.3.1 AIR TURBINE

The turbine- performance can be described by the dimensionless aerodynamic parameters of pressure head Ψ, mass flow rate Φ, power Π and efficiency η expressed as in [8] as a function of the air chamber pressure p_{ch} , the mass flow rate $\dot{m}_t$ and P_t the turbine shaft power :

$$\Psi = \frac{p_{ch}}{\rho_{at}\Omega^2 d^2} \quad (1)$$

$$\Phi = \frac{\dot{m}_t}{\rho_{at}\,\Omega\,d^3} \quad (2)$$

$$\Pi = \frac{P_t}{\rho_{at}\Omega^3 d^5} \quad (3)$$

$$\eta = \frac{P_t}{p_{ch}Q_t} = \frac{\Pi}{\Psi\Phi} \quad (4)$$

Here D is the turbine diameter and Ω is the rotational speed in $\mathrm{rad/s}$,. The torque provided by the turbine is:

$$T_t = P_t/\Omega \qquad (5)$$

The size and inertia of the biradial turbine installed in Mutriku wave power plant (see Figure 3) are shown in Table 2.

TABLE 2. TURBINE CHARACTERISTICS

Parameters	Symbol	Value	Unit
Diameter	***d***	0.50	m
Total inertia of turbo-generator set	***I***	5.00	kg m^2

FIGURE 3. TURBINE INSTALLED IN MUTRIKU WAVE POWER PLANT

The turbine characteristics $\Phi = \mathrm{f}(\Psi)$, also known as turbine damping, and $\eta = \mathrm{f}(\Psi)$ are plotted in Figure 4.

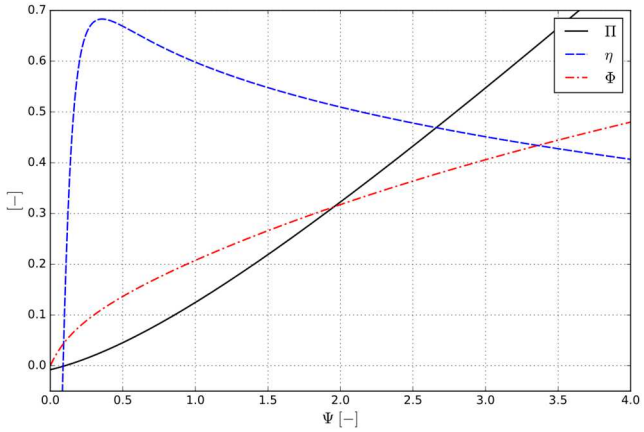

FIGURE 4. PERFORMANCE CURVES OF OPERA BIRADIAL TURBINE. DIMENSIONLESS FLOW RATE Φ, POWER COEFFICIENT Π AND EFFICIENCY η VERSUS DIMENSIONLESS PRESSURE HEAD Ψ. BASED ON DATA FROM [9].

2.3.2 ELECTRICAL GENERATOR

The electrical generator installed in the PTO is an asynchronous induction generator with a rated power of 30 kW, whose characteristics is extracted from [9] and listed in Table 3.

TABLE 3. GENERATOR SPECIFICATIONS

Parameters	Symbol	Value	Unit
Rated power	P_{nom}	30	kW
Rated torque	T_{nom}	200	Nm
Rated speed	N_{nom}	1470	rpm
Runaway speed	N_{run}	3000	rpm
Insulation class	*Class*	H (180 °C)	
Number of pair poles	N_{pp}	2	-
Weight	W_{kg}	250	kg
Nominal voltage	V_{nom}	400	V
Frequency	f_{hz}	50	Hz

2.3.3 SAFETY VALVE FOR CONTROL OF THE TURBINE

A safety valve installed in the turbine operates in high energetic sea states (SS) to protect the components. It prevents the turbine from reaching over-speed. If the threshold of the cut-off speed Ω_{co} is reached, the valve closes and blocks the air flow. A torque is applied at the generator following the present control law and reduces the rotational speed until a cut-in speed Ω_{ci} is reached When this value is reached, the valve opens and the turbine operates normally. It is assumed the valve cyclic actuation time is around 0.25 s. Table 4 below presents the values to control the safety valve:

TABLE 4. OPERATION OF THE SAFETY VALVE

Parameters	Symbol	Value	Unit
Cut-off speed	Ω_{co}	220	rad/s
Cut-in speed	Ω_{ci}	180	rad/s

2.3.4 BUTTERFLY SERIES VALVE

Every turbine in the plant has a butterfly valve located between of the turbine and the air chamber. When the valve is fully open, its angle is 90 deg from its closed position. In some specific conditions, such as highly energetic seas, the butterfly valve was partially closed to continue the production. The plant control software of the Wells turbines adapts the shutter angle as a function of the pressure inside the chambers. However, for comparison, the valve shutter angle was the same for all the CL when the biradial turbine was operating in highly energetic sea-states.

2.3.5 POWER ELECTRONICS AND CONTROL SYSTEM

The power electronics system, or Frequency Converter Unit, consist in a back-to-back converter, set up by interconnecting two Voltage Source Inverter (VSI) drives sharing a common DC bus (see Figure 5). Both systems are individually configured but share a common Real-Time Ethernet Link, thus allowing fast, reliable communication between the PLC system and the converter despite being separated by a distance above 100 m.

FIGURE 5. INTERIOR VIEW OF POWER ELECTRONICS CABINET

Both installed VSI are off-the-shelf Unidrive M700 devices supplied by Control Techniques. These devices integrate a control so they commutate the semiconductor status to obtain the required reference. In Figure 6 the back-to-back converter diagram is shown. From one side,

the generator is connected to one VSI, which is the responsible for achieving the required torque or speed reference. From the other side, the other VSI is connected to the grid through a LCL filter, and it will take or give energy to it following the required power factor reference.

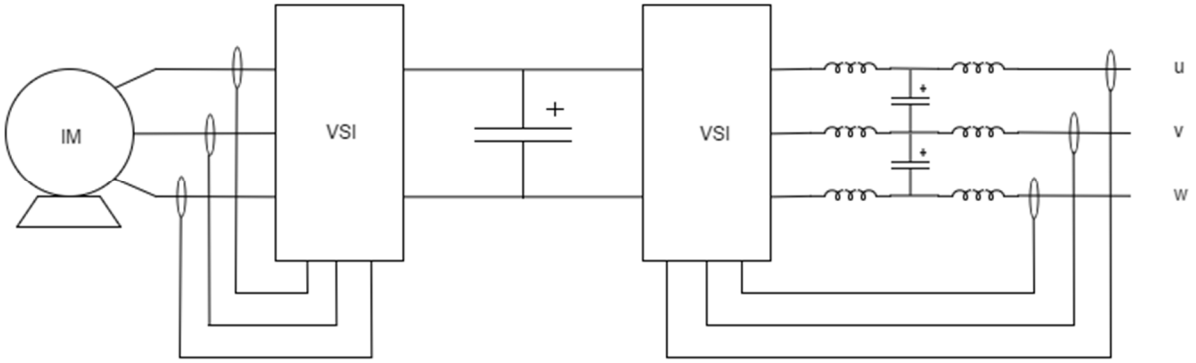

FIGURE 6. BACK-TO-BACK CONVERT UNIT DIAGRAM

Different parameters can be adjusted in the M700 devices. As an example, the user can select between two different control strategies as a scalar V/f control or an RFOC vector control. In this sense, the encoder signals of the generator are introduced into the device to determine the rotational speed and direction. The maximum values of the installed devices at 690 V are 104 A continuous current and 90 kW active power. The voltage bus is connected to a regenerative resistor for safety reasons. If the voltage level of the bus increases above a damage limit, the extra energy will be dissipated through this resistance.

The turbine control system, containing a CPU unit and several I/O modules, is mounted into a separate cabinet, containing all the necessary hardware elements to ensure system operability, as well as safety elements to ensure safe operation of the system (see Figure 7).

The detailed element list and schematics of the control cabinet have been delivered within WP1 partners for descriptive purposes.

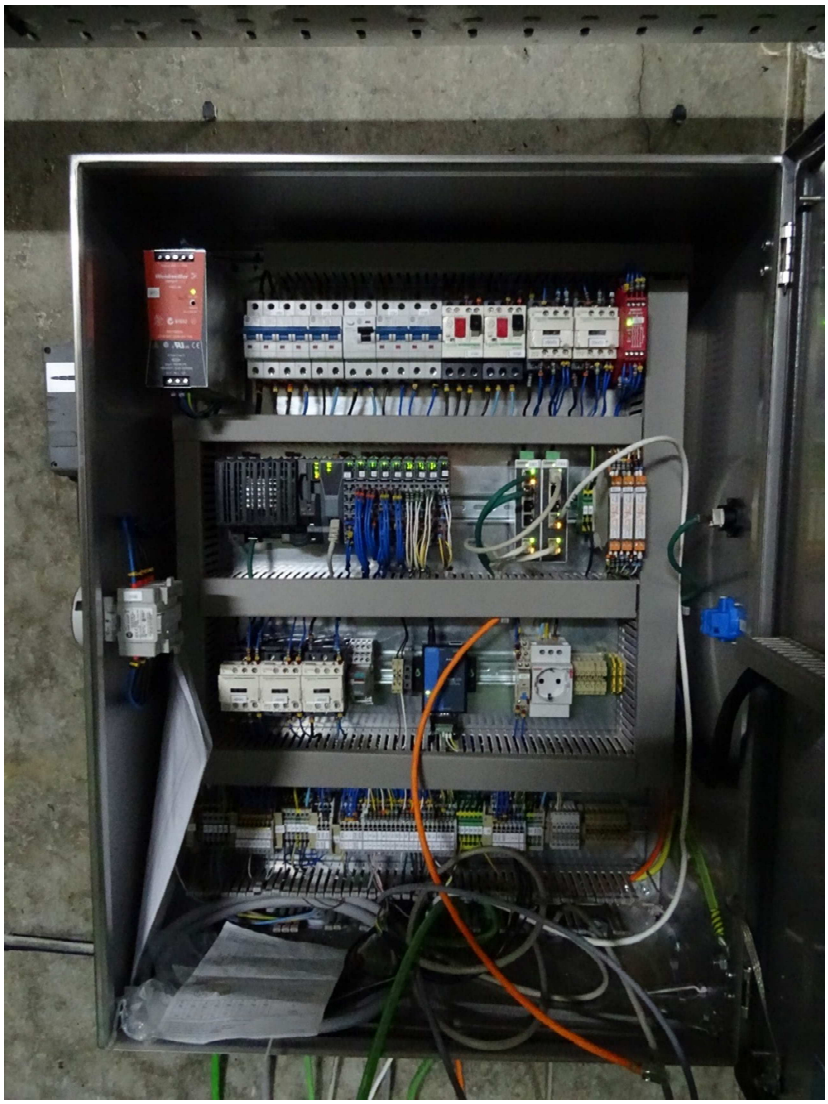

FIGURE 7. CONTROL CABINET INSTALLED IN MUTRIKU

3. CONTROL ALGORITHMS DESCRIPTION

Table 5 summarises the 7 control algorithm laws used in OPERA project and developed in [10]; 6 of them were tested at Mutriku.

TABLE 5. SUMMARY OF CONTROL LAWS

Control Law #	Partner	Adaptive/ Predictive	Controls …	Based on …
CL1	IST	Adaptive	Generator torque	Rotational speed
CL2	UCC	Adaptive	Generator torque	Chamber pressure
CL3	UCC	Adaptive	PTO damping, valve open-close timings	Hourly sea-state data
CL4	IST	Adaptive	Valve open-close timings and position	Rotational speed, chamber pressure and valve position
CL5	UNEXE	Adaptive	Generator torque	Reinforced learning: Next wave information + output power + rotational speed
CL6	TEC	Predictive	Generator torque	Water column motion in chamber (position and speed) Pressure in chamber Turbine speed Wave elevation in front of the plant
CL7	IST	Predictive	Valve open-close timings and position	12-24 sec future wave information, rotational speed and chamber pressure and valve position

The following subsections describe in more detail each control law.

3.1 CL1: ADAPTIVE GENERATOR TORQUE CONTROL BASED ON ROTATIONAL SPEED

3.1.1 DESCRIPTION

CL1 control law is based on simple evidence that the maximum power extraction is achieved with an ideal zero-inertia turbine-generator set whose instantaneous rotation speed is controlled. So, the turbine power is defined as:

$$P_{\text{turb}} = \underbrace{\varrho d^5 \Pi\left(\Psi\left(\eta_{\text{bep}}\right)\right)}_{\text{const}} \Omega^3 \tag{6}$$

where $\Pi(\Psi)$ is the turbine power coefficient as a function of the pressure head coefficient, $\Psi\left(\eta_{\text{bep}}\right)$ is the pressure head coefficient at the best efficiency point, Ω is the rotational speed and *d* is the diameter of the turbine. Based on this equation, the following control law is proposed to define the generator power:

$$P_{\text{gen}} = a\,\Omega^{\text{b}} \tag{7}$$

where a and b are two constants depending on the the turbine geometry and the inertia of the turbine and the generator rotating parts.

Three variations of the control law were implemented. The first applied directly with an upper limit to the instantaneous generator power

$$P_{\text{gen}}(\Omega) = \min\left(a\,\Omega^{\text{b}}, P_{\text{gen}}^{\text{rated}}\right). \tag{8}$$

Here a and b are user defined constants and $P_{\text{gen}}^{\text{rated}}$ is the generator rated power, see Figure 8. If the turbine rotational speed reaches Ω_{max} then the system enters in safe mode and the valve is closed until the rotational speed drops below Ω_{thr}, resuming the system to normal operation.

A second version aims to reach less often the generator rated power, $P_{\text{gen}}^{\text{rated}}$. As such, a stepping increase of the generator power was applied above the rotational speed threshold Ω_{thr1}

$$P_{\text{gen}}(\Omega) = \begin{cases} a_1\Omega^{b_1}, & 0 < \Omega < \Omega_{\text{thr1}}, \\ a_2\Omega^{b_2}, & \Omega_{\text{thr1}} < \Omega < \Omega_{\text{thr2}}, \\ P_{\text{gen}}^{\text{rated}}, & \Omega_{\text{thr2}} < \Omega, \end{cases} \tag{9}$$

where a_1 and b_1, Ω_{thr1} and Ω_{thr2} are user defined constants. The constants a_2 and b_2 are computed such that the control law function is continuous between Ω_{thr1} and Ω_{thr2}, see Figure 9. As in the case of the previous version of the CL1, if the turbine rotational speed reaches Ω_{max} then the system enters in safe mode and the valve is closed until the rotational drops below Ω_{thr1}, resuming the system to normal operation.

During the IST dry tests performed before the turbine commissioning, a novel type of control law 1 was implemented and tested. The idea was to use control law Eq. (8) in normal operation, $0 < \Omega \leq \Omega_{\text{thr2}}$, and partially close the valve when the rotational speed is above Ω_{thr2}. This control is called "Peak-shaving control", see Figure 10. As such, for $\Omega > \Omega_{\text{thr2}}$, the high-speed safety-valve follows a closing law $F(u)$ given by

$$F(u) = \begin{cases} c(u), & u < 1, \\ 0, & u \geq 1. \end{cases} \tag{10}$$

Here $c(u)$ is a non-linear PI control calibrated based on physical arguments. The function $c(u)$ controls the opening fraction of the valve within the range $0.4 \leq c(u) \leq 1.0$. The control u was defined by

$$u = \frac{\Omega - \Omega_{\text{thr2}}}{\Omega_{\text{max}} - \Omega_{\text{thr2}}} \tag{11}$$

If the control u reaches 1, then the system enters in safe mode and the valve is closed until the rotational speed drops below Ω_{thr1}, resuming the system to normal operation.

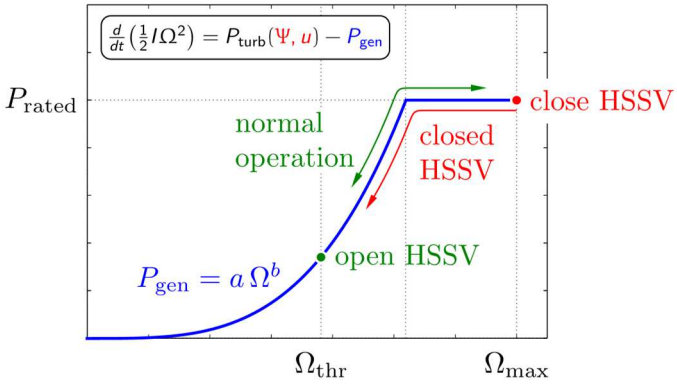

FIGURE 8. BASE VERSION OF THE CONTROL LAW CL1

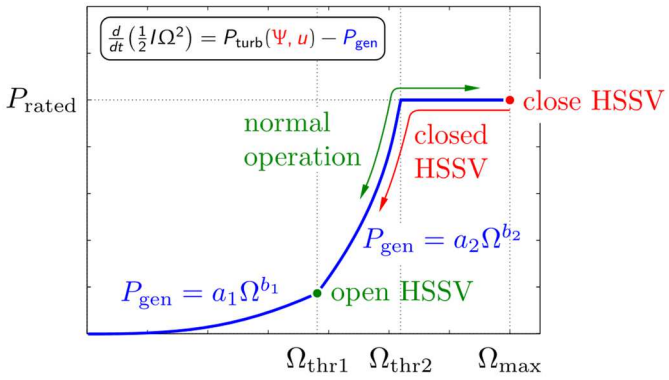

FIGURE 9. STEPPER VERSION OF THE CONTROL LAW CL1

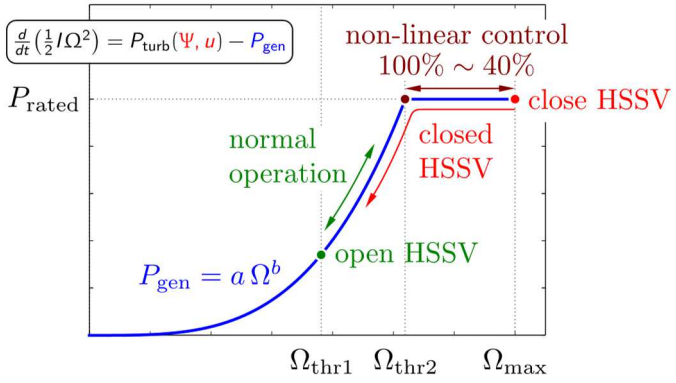

FIGURE 10. "PEAK-SHAVING CONTROL" VERSION OF THE CONTROL LAW CL1

3.1.2 REQUIREMENTS

The CL1 requires as input the measurement of the biradial turbine rotational speed, Ω at a frequency of 2 Hz. The output is the generator torque computed as

$$T_{\text{gen}} = P_{\text{gen}}\,\Omega^{-1} \tag{12}$$

and the instantaneous valve position if operating in safe mode.

3.2 CL2: ADAPTIVE GENERATOR TORQUE CONTROL BASED ON CHAMBER PRESSURE

3.2.1 DESCRIPTION

CL 2 is based on a torque reference determined by a function of the mean pressure measured within the plenum chamber of the OWC and the pneumatic-to-mechanical conversion efficiency of the turbine. This control law results in a quasi-constant torque reference that changes slowly as the mean chamber pressure changes. The mean chamber pressure is calculated based on a moving average over a predetermined time window. Any rapid fluctuations in power capture will be momentarily stored in turbine inertia.

In high energy sea state conditions, the inertia of the turbine may not be large enough to store excess energy, so a second mean pressure based control law was developed that introduces a condition based on instantaneous chamber pressure. The purpose of this added condition was to reduce turbine speed excursions compared to the original controller.

The CL in this case also included a rotational speed 'floor', where if the rotational speed of turbine was below a set value, no torque would be applied to the generator. The floor can be adjusted depending on sea state conditions as well as generator specifications to maximise energy conversion efficiency during operation.

3.2.2 REQUIREMENTS

Minimum requirements are:

- Measurement of the mean chamber pressure.
- Instantaneous chamber pressure.
- Instantaneous rotational speed.
- Ability to run the generator drive in torque control mode.

While desirable requirements are:

- Voltage on the DC-link of the back to back power converter (If measured, this can be used to determine, offline, any flexibility offered by using the DC-link to smooth speed fluctuations.).
- Accurate real-time measurement of pressure drop *across* the turbine.
- Temperature of power electronics and of generator.
- Burst of very high-resolution measurements of voltages, currents. E.g. 200 ms window of data recorded at a sample rate high enough to determine harmonics on 50 Hz, e.g. 1 kHz sampling or greater.

3.3 CL3: ADAPTIVE PTO DAMPING AND VALVE CONTROL BASED ON HOURLY SEA STATE DATA

3.3.1 DESCRIPTION

CL3 is a modified latching controller that does not require the detailed future information. Instead, the control law will use the wave statistical period. To obtain the statistical wave periods, wave forecast or the previous wave statistics can be used. Hence the requirement of future information is not necessary. This control law is proposed as a sub-optimal control for improving wave energy conversion for the OWC devices and other type of wave energy converters, aiming to remove the requirement of future wave prediction. The aim of CL3 is to improve the hydrodynamic and pneumatic energy conversion efficiency of the WEC by altering the hydrodynamic resonance response of device through latching control. As CL3 is latching based only and does not include a generator torque controller, the torque controller from CL1, a rotational speed based torque controller, is applied to the generator for the electrical power take-off.

The implementation of the control law includes the closing and opening of the control valve. Ideally, the control law requires the valve can be open and close very fast. The physical implementation of the CL3 is as following:

Step 1: This control law will close the valve of the OWC when the chamber pressure is zero or very small. It is similar to the conventional latching control, and due to the zero flow rate passing the control valve (corresponding to zero chamber pressure), closing the valve should be easy to achieve.

Step 2: Latching duration is determined based on the wave energy period, T_e, and the resonance period of the internal water surface of the OWC, T_0.

The latching durations are calculated based on the sea state and the internal water surface resonance period. In the latching control, when the chamber pressure is very small (theoretically zero), the control valve closes and remains closed until the latching duration is reached when the valve opens. In the control, the opening and closing of the valve should be as fast as possible.

3.3.2 REQUIREMENTS

Minimum requirements are:

- Summary wave statistics based on wave forecasting
- Valve that can fully open and close in a fast manner (< 0.25 s)
- Indication of the instant of zero or small chamber pressure

While desirable requirements are:

- Accurate wave period data based on recent measurements
- High speed control valve
- High precision real time chamber pressure measurement

3.4 CL4: ADAPTIVE VALVE AND POSITION CONTROL BASED ON ROTATIONAL SPEED, CHAMBER PRESSURE AND VALVE POSITION

3.4.1 DESCRIPTION

CL4 is an enhanced version of the strategy 2 described in [11,12]. It uses the rotational speed and the air chamber pressure to control the HSSV position. The main goal is to avoid over-powering the turbine and the generator in more energetic sea states.

The variable used to compute the opening instants is the pressure head coefficient defined by:

$$\Psi = \frac{p_{\mathrm{ch}}}{\rho_{at}\Omega^2 d^2}. \tag{13}$$

Being p_{ch} the pressure inside the chamber.

The latching control implemented within this control, is based on a positive threshold for the pressure head coefficient, Ψ_{thr}^{+}, and a negative threshold, Ψ_{thr}^{-}, see Figure 11.

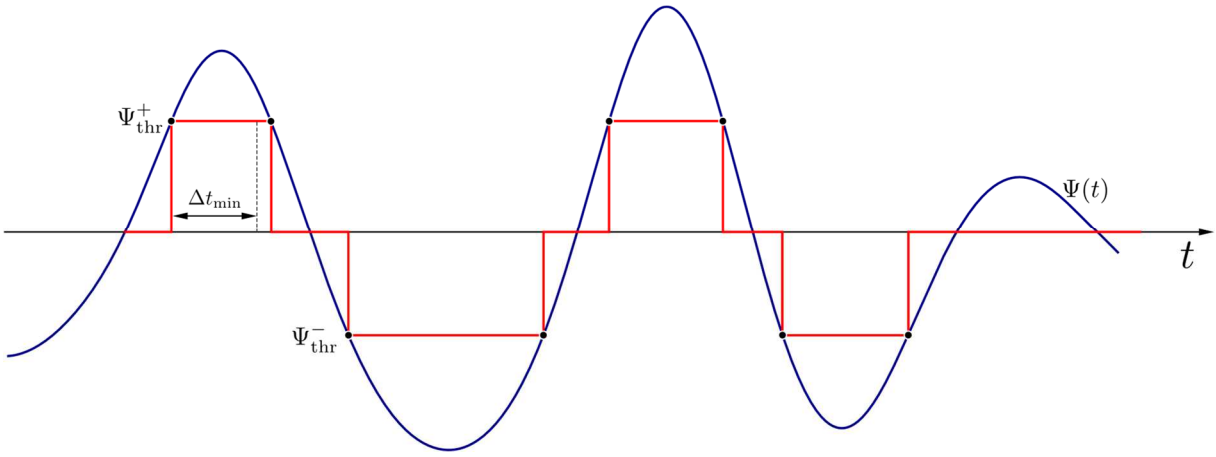

FIGURE 11. DEFINITION OF THE THRESHOLD VALUES Ψ^+_{thr} AND Ψ^-_{thr}, AND THE MINIMUM ELAPSED TIME $\Delta t_{\min}$

When Ψ is positive and is above Ψ^+_{thr} then the valve is opened. The valve is closed when $\Psi < \Psi^+_{\text{thr}}$ and the elapsed time after the opening order is greater than $\Delta t_{\min}$. Analogous strategy is applied when Ψ is negative. The threshold values Ψ^+_{thr} and Ψ^-_{thr} are to be determined experimentally. The used of a pre-defined minimum elapsed time $\Delta t_{\min}$ after the opening order aims to avoid intermittent operation for short time intervals.

The outer-loop of this control law applies the generator control law CL1 as given by Eq. (8).

To apply this law, it is required to filter the pressure signal before computing Ψ.

3.4.2 REQUIREMENTS

Real-time measurement of the following signals:

- Biradial turbine rotational speed, Ω.
- Pressure in the air chamber with the biradial turbine, p_{ch}.

Desired data acquisition at a frequency of 4 Hz.

3.5 CL5: ADAPTIVE TORQUE CONTROL BASED ON REINFORCEMENT LEARNING

3.5.1 DESCRIPTION

CL5 is concerned with the application of Reinforcement Learning (RL) for the optimal control of an OWC. This is an on-line, model-free algorithm which ensures that it can adapt to changes to the device hydrodynamics over time and is unbiased by modelling errors. The output turbine power versus speed for different wave condition has the typical characteristic shown in Figure 12. The red curve represents the maximum power that can be delivered at all wave

conditions. If this curve is known, the turbine is controlled to follow the curve by measuring output power and adjust speed accordingly. The red curve can be obtained analytically such as:

$$P_{opt} = a\,\Omega^{b}, \tag{14}$$

where the coefficients (α and b) can be found using an optimised technique based on the hydrodynamic model. In CL4, RL will be used to find the optimal curve on-line and without relying on the hydrodynamic model.

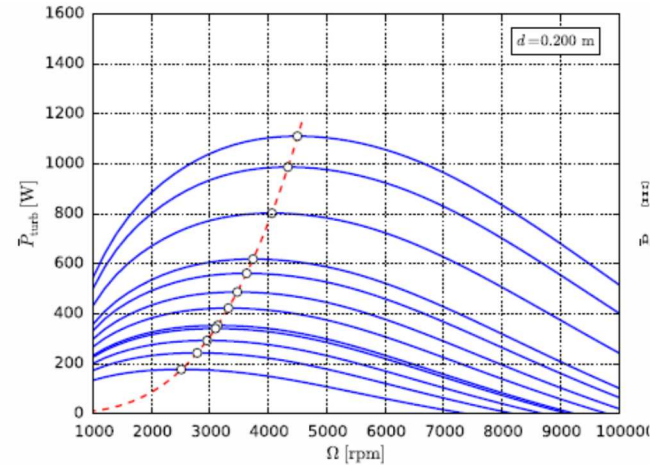

FIGURE 12. TURBINE CHARACTERISTIC [9]

The aim is to implement RL to find the optimal curve relating maximum power and turbine speed by measuring the output generator power and adjust the generator torque. Figure 13 shows how RL is integrated with the OWC model.

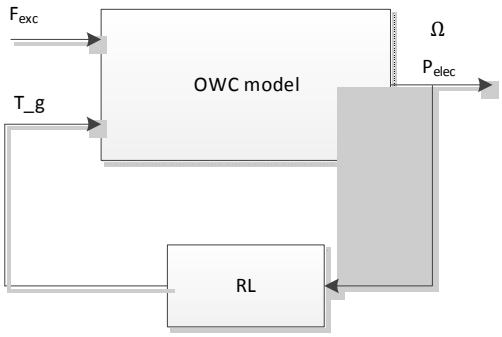

FIGURE 13. RL INTEGRATION WITH THE OWC MODEL

- **Reinforcement learning implementation**

In RL, an agent, which is in a particular state s_n, interacts with the surrounding environment by taking an action a_n, where n defines the time step of the RL algorithm. The agent then moves to a new state, s_{n+1}, and the action is followed by a reward, r_{n+1}, depending on its

outcome. The action selection process is modelled as a Markov decision process based on the value function, which expresses the estimate of the future reward. The agent is expected to learn an optimal behaviour, known as policy, over time for the maximisation of the total reward.

- **RL Implementation**

The system model supplied by Tecnalia is discretised with a sampling period of 0.1sec. Oscillating measured power is filtered by a low-pass to smooth out the oscillations. The control algorithm runs at a rate that is longer than the time response of the controlled plant in order for the change in the control parameter to be noticed by the reward function.

3.5.2 REQUIREMENTS

As was shown in Figure 13, the controller needs to measure the turbine speed and power at a sampling frequency of 10 Hz. The controller will update the generator torque every 1 minute.

The minimum requirement is to be able to measure the turbine speed and power at a sampling frequency of 10 Hz. Also, it is required that the controller is able to update the generator torque every 1 minute.

Desirable requirements are:

- Wave measurements from (multiple) wave sensor(s) ("multiple" in particular for off-shore to guarantee accurate directional power density spectrum; on-shore the assumption of one significant wave direction might suffice) to calculate wave height and period as input at chamber/buoy;
- Pressure inside the chamber, to verify correlation with wave data input.
- Wave height and period at chamber/buoy;
- Predictive pressure modelling based on some form of current wave climate and past pressure data

3.6 CL6: PREDICTIVE GENERATOR TORQUE CONTROL BASED ON FUTURE WAVE INFORMATION

Initially, CL6 was classified as a predictive algorithm depending on the presence of a real-time wave elevation measurement situated up-wave to the plant. Due to adverse weather conditions, the CNC4200 sensor was only installed at the end of the testing period allowing only a couple of weeks for implementing and testing this algorithm. Knowing the eventual delay in the installation of this sensor, another control law labelled CL6.0 has been developed to take advantage of this slot. The predictive algorithm is then defined as CL6.1 in the rest of the document.

3.6.1 CL6.0 DESCRIPTION

This variable speed control is based on a customised torque law - $T_{ctrl} = f(\Omega)$ - and its parametrisation relies on the observation of the PTO operation with different CLs. In low energetic seas, operational CL would apply a resistive torque at low speed regimes too high having the effect of preventing the turbine from accelerating. In high seas, the torque applied was in some cases too low and the turbine would reach the rotational speed threshold, meaning the activation of the HSSV. Sometimes it reached the maximum threshold having the effect of stopping the production for safety reason. The strategy behind this law is to gradually increase the torque until the generator reaches nominal speed and then follow a power law shape. In higher regimes, the nominal torque is applied to break the turbine and prevent over-speeding. There are 5 operational regions for this CL6.0 as can be seen in Figure 14:

- 1: no torque is applied for low speeds
- 2: the torque slowly increases with the speed until reaching the generator nominal rotational speed.
- 3: a power law defined by [a,b] coefficients as other CLs is applied until reaching the threshold speed signifying the shut-off of the HSSV.
- 4: here there is a plateau limited at the nominal torque while the speed still increases. In this operation region the generator is allowed to be overloaded.
- 5: No torque is applied in order not to cause damages to the component.

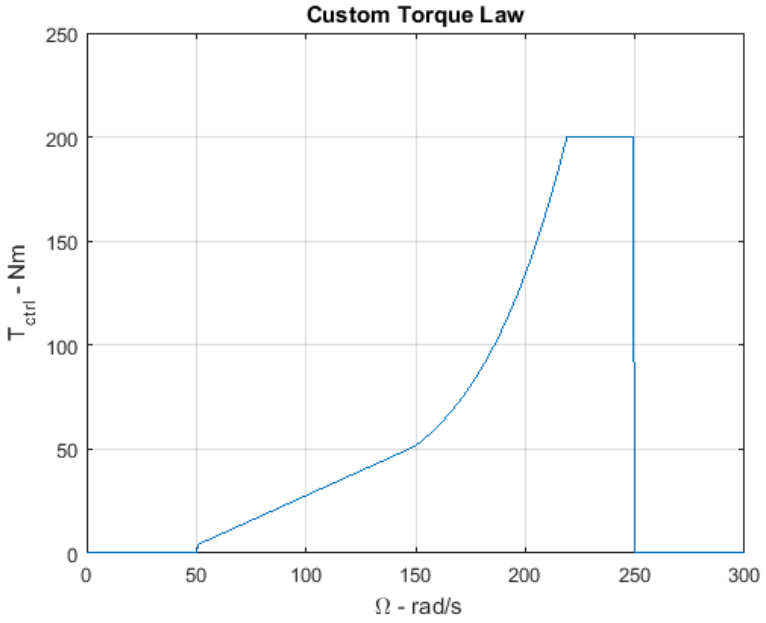

FIGURE 14. OPERATIONAL REGIONS FOR CL6.0

3.6.2 CL6.1 DESCRIPTION

- **Control strategy and predictive optimisation process**

The control law 6 is a variation of the controller presented in [13] applied to variable speed control. It uses a predictive algorithm to optimise online the control parameters that define the torque law. It is a Model Predictive Control (MPC)-like algorithm that includes model non-linearities (air compressibility, turbine and generator efficiencies). The aim is to control the turbine speed to set the PTO at its best efficiency point for the plant condition by applying a controlled torque T_{ctrl} to the generator. Considering the torque law:

$$T_{ctrl} = \ a\ \Omega^{b-1} \tag{15}$$

The predictive algorithm finds the optimal configuration of $[a, b]$ for the next incoming waves. The objective is thus to define the best torque-law for the prediction horizon of incoming waves, typically $T_{ph} = 2\ T_p$, and apply it during the re-planning time $T_{rp} \ = \ T_p$. (see Figure 15).

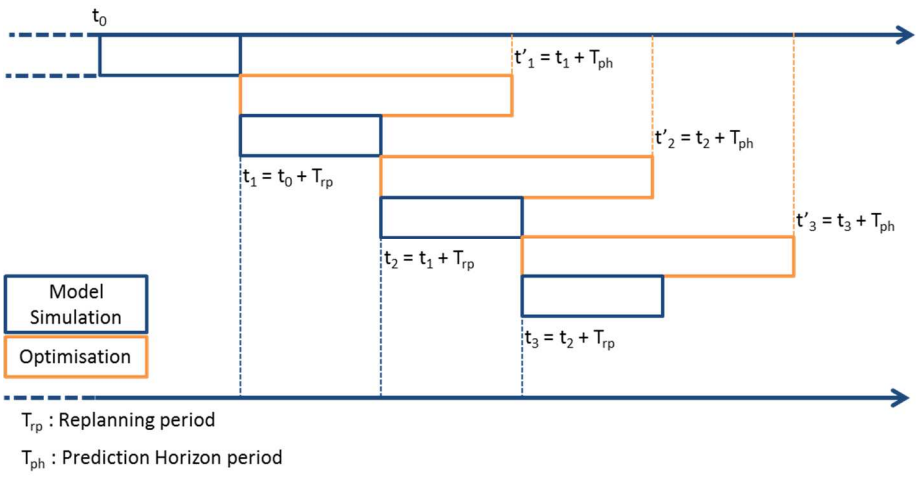

FIGURE 15. DEFINITION OF BEST TORQUE-LAW FOR THE PREDICTION HORIZON OF INCOMING WAVES

For each optimisation process, the full numerical model is run and the objective is to maximise a cost function taking into account a combination of pneumatic power, turbine power and generator power:

$$J = max \sum_1^{N_{ph}} (\alpha\ P_{pneu} + \beta\ P_{turb} + \gamma\ P_{gen}) \tag{16}$$

Where α, β and γ are weighting parameters.

- **Estimation of the wave force**

Being a predictive algorithm, the wave excitation force must be estimated. The wave elevation sensor installed around 200 m in front of the plant offers sufficient time for the prediction

process. Figure 16 includes the relation between the water depth (changes with the tides) and the wave travel time based on observation with a previous RBR measurement campaign. Unfortunately, the wave direction was not taken into account in the analysis which may be the reason for the results dispersion of time delay for a given water depth.

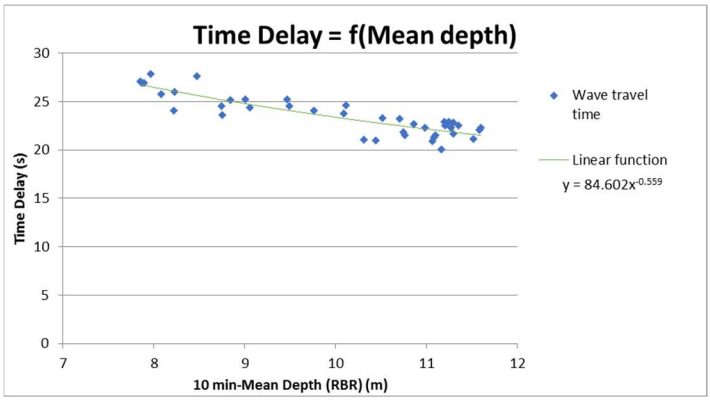

FIGURE 16. RELATION BETWEEN THE WATER DEPTH AND THE WAVE TRAVEL TIME

This data is used to parametrise the prediction time T_{ph} containing the maximum amount of wave data available. In the process, the time T_{ph} is taken from the 1st wave measured until this wave reaches the front wall of the plant. The entire vector of wave elevation is converted to a wave excitation $F_{exc,est}(t)$, estimation based on the theory presented in [14], [15]:

$$F_{exc,est}(t) = k_t(t) * \eta_w(t) = k_t(t - t_c) * \eta_w(t + t_c) = k_{t,c}(t) * \eta_{w,p}(t) \quad (17)$$

$k_{t,c}(t)$ is the causal complex excitation impulse response function (EIRF) and $\eta_{w,p}(t)$ the predicted wave with the t_c causal time. That way both amplitudes and phases are considered. The convolution is resolved in time domain by approximating the EIRF with the Prony method at 15th order and calculated by a state-space system. Figure 17 shows a comparison of a wave excitation force and its respective wave elevation computed from a wave spectrum versus the estimated one computed from the same wave elevation for a sea state $H_s = 2$ m and $T_p = 14.5$ s.

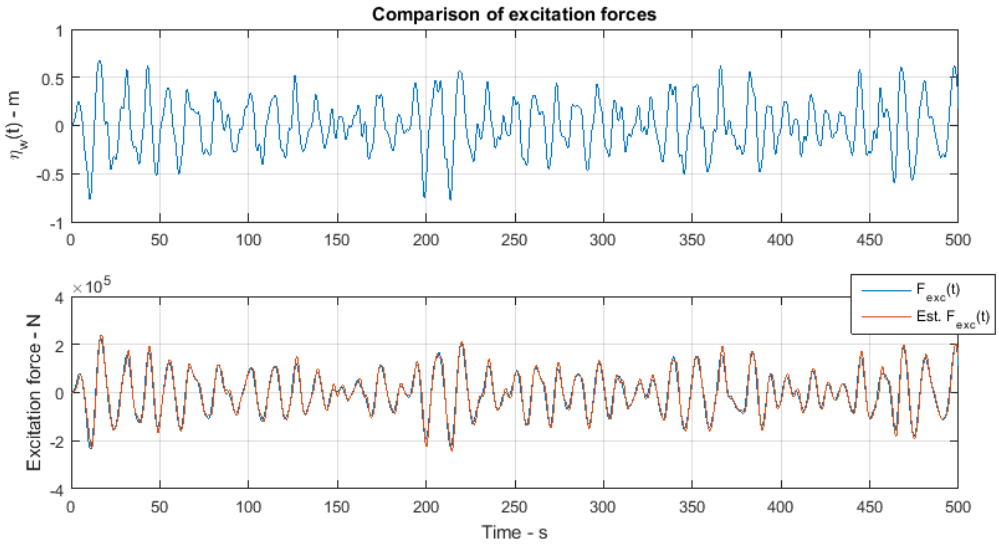

FIGURE 17. COMPARISON OF A WAVE EXCITATION FORCE AND ITS RESPECTIVE WAVE ELEVATION

At first sight, the estimation looks rather good, but a spectral representation allows to compare the magnitudes for several frequencies. In Figure 18, one can attest that for frequencies until 0.5-0.6 rad/s the estimation is fine, and above there is an overestimation meaning that the estimation will be less accurate for wave periods lower than 10 s.

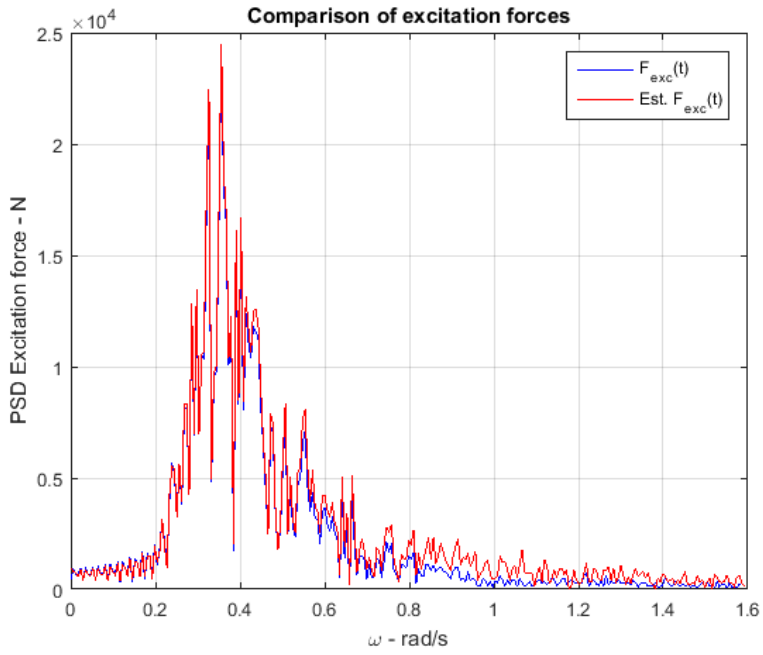

FIGURE 18. SPECTRAL REPRESENTATION OF EXCITATION FORCES

3.6.3 REQUIREMENTS

This algorithm uses both plant measurement and environmental data. The minimum requirements of CL6 are presented in Table 6:

TABLE 6. MINIMUM REQUIREMENTS OF CL6

Measurement	Specification [s]
Water column motion in the chamber (position and speed)	Real-time
Pressure in chamber	
Turbine speed	
Wave elevation in front of the plant	with minimum 1 wave period prediction

In addition to these basic needs, the algorithm needs an accurate hydrodynamic model and an exact PTO characterisation. The more accurate the model, the better the optimisation which is:

- The prediction of the excitation force: using a wave elevation sensor located in front of the plant, the wave force is estimated for the duration of the wave travel time.
- A validated numerical model: during the optimisation process

3.7 CL7: PREDICTIVE VALVE CONTROL BASED ON FUTURE WAVE INFORMATION

3.7.1 DESCRIPTION

A novel high-order method to compute optimal control problems was developed for CL7.. The method presents several advantages over the current state-of-the-artPseudo-Spectral methods. The resultant work has been published in a journal paper and presented in two conferences [11], [12], [16] [8-10].

A Discontinuous Galerkin (DG) finite element time-stepping method is used for the solution of optimal control problem of the biradial turbine within the framework of the Pontryagin's Maximum Principle (PMP). The finite element function space generally used by DG approximations consists of piecewise polynomials that are allowed to be discontinuous across element boundaries. The inter-element boundary conditions are weakly enforced. The state, co-state and control variables are approximated using Legendre polynomials. The resultant integrals are evaluated using a Gauss-Lobatto quadrature rule with points at the extremes of the integration interval.

- **Weak formulation for the state equations**

The DG finite element space is defined as

$$V_h^k \equiv \{v \in L^2(0,T): v|_{I_e} \in P^k(I_e), e = 0, \dots, N\} \quad (18)$$

where $P^k(I_e)$ is the space of the polynomials in I_e of degree at most k. Although not required, the same degree k of polynomial approximation was used for all the finite elements, I_e, that discretize the domain Ω.

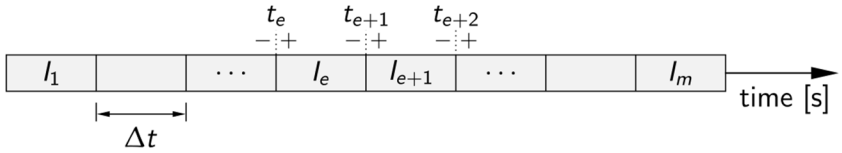

FIGURE 19. DISCRETIZATION OF THE TIME DOMAIN IN SMALL ELEMENTS

The DG method seeks an approximate solution $x_h \in V_h^k$ such that, for any $v_h \in V_h^k$, and all I_e,

$$\int_{I_e} v_h \frac{\mathrm{d}x_h}{\mathrm{d}t}\mathrm{d}t + v_h(t_e)\,[x_h(t_e^+) - x(t_e^-)] = \int_{I_e} v_h f \mathrm{d}t, \tag{19}$$

where the superscripts $+$ and $-$ denote the right and left element boundaries, see Figure 19.

The jump term defined by:

$$x_h(t_e^+) - x(t_e^-) = [\![x]\!]_e \tag{20}$$

serves the purpose of weakly enforcing the left boundary condition $x(t_e^-)$ on element I_e.

- **Legendre polynomials**

Consider a polynomial approximation of k-th order for x in the element I_e such that

$$\hat{x}_h(\tau) = \sum_{j=0}^{k} p_j(\tau)\tilde{x}_{e,j} \tag{21}$$

Choosing Legendre polynomials, p_j may be obtained using the Rodrigues' formula

$$p_j(\tau) = \frac{1}{j!\,2^j}\left(\frac{\mathrm{d}}{\mathrm{d}x}\right)^j (x^2-1)^j \tag{22}$$

It can be shown that $p_j(1) = 1$ and $p_j(-1) = (-1)^j$.

- **Domain transformation for each finite-element**

Using an affine transformation from $t \in I_e$ to $\tau \in [-1,1]$, we obtain

$$\int_{-1}^{1} \hat{v}_h \frac{\mathrm{d}\hat{x}_h}{\mathrm{d}\tau}\mathrm{d}\tau + \hat{v}_h(-1)\hat{x}_h(-1^+) - \hat{v}_h(-1)\hat{x}(-1^-) = \frac{\Delta t}{2}\int_{-1}^{1} \hat{v}_h\,\hat{f}\,\mathrm{d}\tau \tag{23}$$

where the hat denotes a function mapped onto a local computational domain, τ, using

$$\tau = \frac{2}{\Delta t_e}(t - t_e) - 1 \tag{24}$$

- **System of equations**

Equation (23) is applied to all elements I_e of the computational domain Ω. After same algebraic manipulation, we get a system of algebraic equations

$$\left(A_{ij} + P_{ij}^{-}\right)\tilde{x}_{e,j} = p_i(-1)\, x_{e,j}^{\mathrm{BC}} + b_i, \tag{25}$$

where

$$A_{ij} = \int_{-1}^{1} p_i \dot{p}_j \mathrm{d}\tau \tag{26}$$

and

$$b_i = \frac{\Delta t}{2}\int_{-1}^{1} p_i \hat{f}\, \mathrm{d}\tau \tag{27}$$

The matrix associated with the inter-element boundary condition is given by

$$P_{ij}^{-} = p_i(-1)\, p_j(-1) \tag{28}$$

The boundary conditions $x_{e,j}^{\mathrm{BC}}$ for each element I_e are given by

$$x_{e,j}^{\mathrm{BC}} = \begin{cases} x_{0,j}, & e = 0, \\ \sum_{j=0}^{k} p_j(+1)\, \tilde{x}_{e-1,j}, & 0 < e \leq N \end{cases} \tag{29}$$

The integrals appearing in the formulation are computed using a standard Gauss-Lobatto integration rule with q points, being two of them in the extremes of the integration interval.

The initial value problem is solved starting from the element I_0, integrating sequentially and element-by-element forward in time. Each component of the state vector $\mathbf{x}$ of is computed sequentially.

- **The weak form of the adjoint equations**

The adjoint equations are integrated backwards. The weak formulation for the adjoint equations is similar to (23):

$$\int_{-1}^{1} \hat{v}_h \frac{\mathrm{d}\hat{\lambda}_h}{\mathrm{d}\tau}\mathrm{d}\tau + \hat{v}_h(1)\left[\lambda(1^+) - \hat{\lambda}_h(1^-)\right] = \frac{\Delta t}{2}\int_{-1}^{1} \hat{v}_h \hat{g}\, \mathrm{d}\tau \tag{30}$$

where the jump term is defined at the right-hand side of the element I_e and defined by

$$\lambda(t_{e+1}^{+}) - \lambda_h(t_{e+1}^{-}) = [\![\lambda]\!]_{e+1} \tag{31}$$

Considering a polynomial approximation of k-th order for λ we get

$$\hat{\lambda}_h(\tau) = \sum_{j=0}^{k} p_j(\tau)\, \tilde{\lambda}_{e,j} \tag{32}$$

The resulting system of equations is given by

$$\left(A_{ij} - P_{ij}^{+}\right)\tilde{\lambda}_{e,j} = -p_i(+1)\, \lambda_{e,j}^{\mathrm{BC}} + c_i \tag{33}$$

where

$$c_i = \frac{\Delta t}{2} \int_{-1}^{1} p_i \, \hat{g} \, \mathrm{d}\tau \tag{34}$$

The boundary conditions $\lambda_{e,j}^{\mathrm{BC}}$ for each element I_e are given by

$$\lambda_{e,j}^{\mathrm{BC}} = \begin{cases} \lambda_{T,j}, & e = N \\ \sum_{j=0}^{k} p_j(-1) \, \tilde{\lambda}_{e+1,j}, & 0 \leq e < N \end{cases} \tag{35}$$

- **Maximisation of the Hamiltonian function**

Following the typical approach of the finite element methods, we approximate each component of the vector of control variables u with a Legendre polynomial such that

$$\hat{u}_h(\tau) = \sum_{j=0}^{k} p_j(\tau) \, \tilde{u}_{e,j} \tag{36}$$

The optimal solution $u(t)$ is computed by maximising the integral of the Hamiltonian, $\mathcal{H}$, in each time interval, I_e. For the present bang-bang optimal control problem, we assume a constant value of $\hat{u}_h$ in each element, I_e. In our finite element context, a constant value of $\hat{u}_h$ in each element, I_e, is equivalent to a zero-degree polynomial approximation

$$\hat{u}_h(\tau) = p_0(\tau)\tilde{u}_{e,0} \tag{37}$$

- **Solution algorithm**

The overall solution method for the present OCP is described in Figure 20. The method starts by doing the initialisation. Afterwards, the co-state, the states and control variables are solved iteratively using a segregated solution method until convergence.

Algorithm 1 Iterative method to solve the state-adjoint-control set of equations

for $e \in \{0, \ldots, N\}$ **do**
  compute $\mathbf{x}_e^0$ as the solution of $\dot{\mathbf{x}}_e = \mathbf{f}\left(t, \mathbf{x}_e, u_e^0 = 1\right)$
end for
$n \leftarrow 0$
repeat ▷ outer loop
  $n \leftarrow n + 1$
  for $e \in \{N, \ldots, 0\}$ **do** ▷ backward solution of the adjoint equation
    compute $\boldsymbol{\lambda}_e^n$ as the solution of $\dot{\boldsymbol{\lambda}}_e = \mathbf{g}\left(t, \mathbf{x}_e^{n-1}, \boldsymbol{\lambda}_e, u_e^{n-1}\right)$
  end for
  HysterisysMode $\leftarrow$ False
  for $e \in \{0, \ldots, N\}$ **do** ▷ forward solution of the control coupled with the state equations
    compute $\mathbf{x}_e^n$ as the solution of $\dot{\mathbf{x}}_e = \mathbf{f}(t, \mathbf{x}_e, u_e^n)$
    if $\Omega > \Omega_{\max}$ **then**
      HysterisysMode $\leftarrow$ True
    end if
    if HysterisysMode = True and $\Omega < \Omega_{\mathrm{thr}}$ **then**
      HysterisysMode $\leftarrow$ False
    end if
    if HysterisysMode = True **then**
      $u \leftarrow 0$
    else
      compute the optimal $u_e^n(t)$
    end if
  end for
until $\left\| \mathbf{x}_e^n - \mathbf{x}_e^{n-1} \right\|_\infty < \epsilon_x$

FIGURE 20. CL7 SOLUTION ALGORITHM

3.7.2 REQUIREMENTS

CL7 requires an accurate estimation of the incoming waves to compute the excitation force that acts on the OWC.

4. MEASUREMENT SYSTEM & DATABASE

4.1 DATA COLLECTION METHODOLOGY

In order to monitor and record the maximum quantity of data corresponding to the control law testing, local signals from sensors or any control signal which can be generated, are collected by means of a real-time data logging system designed for that purpose.

The complete list of signals registered in the database is shown in Table 7. Each parameter is associated to a signal code that is not represented here but detailed in a technical note from WP1 [17].

TABLE 7. LIST OF PARAMETERS RECORDED IN THE DATABASE

COMMENT	Field name	SQL Type	Comments
id	id	BIGINT	DB row identifier.
TimeStamp	TimeStamp	TIMESTAMP	Timestamp of the data row, including millisecond information.
msec	msec	SMALLINT	Timestamp millisecond attribute. This is made redundant for compatibility issues, as some drives strip off the millisecond term in the TimeStamp column.
Quality	Quality	SMALLINT	Data quality identifier, Possible values are: 192: Good Data Quality 255: No quality data available Any Other value: Bad Data Quality
	Col001	FLOAT	Not used
Control Law Number	Col002	FLOAT	Control law number as defined in WP4.
Test Run Number	Col003	FLOAT	Test Number Identifier. Helps to identify test bins
STA Current State	Col004	FLOAT	Current State of PLC State Machine: 1: Booting 2: Standby 3: Spin-up 4: Operating 5: Spin-down 6: Safe Standby
Vrel Sigma 60	Col005	FLOAT	Standard deviation of the distance to internal water level computed with a 60 s time window, according to exponential averaging (See Annex)
Vrel Sigma 300	Col006	FLOAT	Standard deviation of the distance to internal water level computed with a 300 s time window, according to exponential averaging (See Annex)
Pressure Sigma 60	Col007	FLOAT	Standard deviation of chamber pressure computed with a 60 s time window, according to exponential averaging (See Annex)
Pressure Sigma 300	Col008	FLOAT	Standard deviation of chamber pressure computed with a 300 s time window, according to exponential averaging (See Annex)
Motor Torque	Col009	FLOAT	Motor torque reference, as passed by the PLC to the VFD.
Chamber pressure	Col010	FLOAT	Chamber pressure

Water Level	Col011	FLOAT	**Distance** to internal water surface, as measured by the Radar Level Sensor.
Generator Temp 1	Col012	FLOAT	Temperature measurement in generation winding nº1.
Generator Temp 2	Col013	FLOAT	Temperature measurement in generation winding nº2
Generator Temp 3	Col014	FLOAT	Temperature measurement in generation winding nº3
Pressure RMS	Col015	FLOAT	Running RMS value calculation from chamber pressure
	Col016	FLOAT	Not used
STA Current State	Col017	FLOAT	See Col004. Duplicated here as floating-point number.
Run Time	Col018	FLOAT	Run-time accumulated in current state
	Col019	FLOAT	
Damper Position	Col020	FLOAT	Position of the series butterfly valve. Valid range goes from [0º - Closed to 90º -Open]
Galeria Relative Humidity	Col021	FLOAT	RH in the turbine galleria
Sigma Water velocity	Col022	FLOAT	Standard deviation of the water level velocity computed with a 600 s time window, according to moving average method.
Avg Water Level	Col023	FLOAT	Average value of the distance to internal water level computed with a 600 s time window, according to moving average method.
Sigma Water level	Col024	FLOAT	Standard deviation of the distance to internal water level computed with a 600s time window, according to moving average method.
Sigma Water velocity	Col025	FLOAT	Standard deviation of the water level velocity computed with a 600 s time window, according to moving average method.
Water velocity	Col026	FLOAT	Computation of water velocity by finite differences using 1st level SG with span = 9.
HSSV Position	Col027	FLOAT	HSSV valve linear position. Valid range is [0-63 mm]
HSSV Open	Col028	FLOAT	Status of HSSV valve.
Vibration Sensor	Col029	FLOAT	Horizontal axis vibration sensor reading.
Flow	Col030	FLOAT	Air Flow calculated as chamber area multiplied by water velocity (Col026)
	Col031	FLOAT	Not used
Alarm Status	Col032	FLOAT	Not used
Pressure Sensor 1	Col033	FLOAT	See turbine diagram in Annex 8.1
Pressure Sensor 2	Col034	FLOAT	See turbine diagram in Annex 8.1
Pressure Sensor 3	Col035	FLOAT	See turbine diagram in Annex 8.1
Pressure Sensor 4	Col036	FLOAT	See turbine diagram in Annex 8.1
Pressure Sensor 5	Col037	FLOAT	See turbine diagram in Annex 8.1
Pressure Sensor 6	Col038	FLOAT	See turbine diagram in Annex 8.1
Pressure Sensor 7	Col039	FLOAT	See turbine diagram in Annex 8.1
Pressure Sensor 8	Col040	FLOAT	See turbine diagram in Annex 8.1
Pressure Sensor 9	Col041	FLOAT	See turbine diagram in Annex 8.1
Pressure Sensor 10	Col042	FLOAT	See turbine diagram in Annex 8.1
Accelerometer 1	Col043	FLOAT	Horizontal Accelerometer Reading. Not used.

Accelerometer 2	Col044	FLOAT	Vertical Accelerometer Reading. Not used.
Temperature Sensor K1	Col045	FLOAT	Temperature measurement in generator bearing
Temperature Sensor K2	Col046	FLOAT	Temperature measurement in generator bearing
Antifog	Col047	FLOAT	Not used
PressureMean_300	Col048	FLOAT	RMS value of the chamber pressure computed with a 300 s time window.
Wave Elevation	Col049	FLOAT	Wave Elevation sensor
Wave Elevation No Tide	Col050	FLOAT	Wave elevation sensor reading with tide level correction.
Drive 1 Speed Ref	Col051	FLOAT	Speed reference passed by the PLC to the VFD. Not used int Torque Control Mode.
Drive 1 Speed Feedback	Col052	FLOAT	Motor Speed measurement through the generator encoder.
Drive 1 Total Current	Col053	FLOAT	Measured total current flowing to/from the generator.
Drive 1 Active Current	Col054	FLOAT	Measured active current flowing to/from the generator.
Drive 1 Torque Ref	Col055	FLOAT	Torque reference as % of nominal passed by the PLC to the VFD. Not used in Torque Control Mode
Drive 1 Out Hz	Col056	FLOAT	Measured output frequency in the Drive terminals.
Drive 1 Out V	Col057	FLOAT	Measured output voltage in the Drive terminals.
Drive 1 Out Power	Col058	FLOAT	Estimated Drive power as measured in the Drive terminals.
Drive 1 Out Power	Col059	FLOAT	Same as above.
Drive 1 Out Power	Col060	FLOAT	Same as above.
Regen Var Power	Col061	FLOAT	Estimated apparent power delivered to grid by regenerative Drive
Regen Total Current	Col062	FLOAT	Measured total current delivered to the grid.
Regen Active Current	Col063	FLOAT	Measured active current delivered to the grid.
Regen OutV	Col064	FLOAT	Measured output voltage in the regenerative drive terminals.
Regen OutPower	Col065	FLOAT	Power delivered to the grid by the Regenerative Drive.
Regen BusDC	Col066	FLOAT	DC Bus Voltage as measured by the Regenerative Drive
Regen In Power1	Col067	FLOAT	Not used. Provides a reference to the power to be extracted by the regenerative Drive.

4.2 MEASUREMENT CALIBRATION METHODOLOGY

A campaign of on-field measurement focusing on electrical matters was performed with a portable power analyser because there were doubts on the obtained electrical power levels. In the electrical components installed after the biradial turbine are the induction generator, the sine-wave filter and the power electronics. In the actual setup, the back-to-back power converter (B2B) processes an estimate of electrical quantities at its input and outputs. They are the data uploaded to the OPERA database (DB). However, this estimation is not ideal and it is possible to improve the quality of data by comparing them with measurements. The expected output is to isolate the possible losses, assess the efficiencies independently for each of the components and obtain the correction factors from the measurements to estimated data.

Figure 21 shows a schematic view of the electrical setup of the PTO installed for the OPERA project, including the 3 measurement points where the power analyser is to be situated during the measurement campaign. The equipment used is a Yokogawa WT1600 digital power meter [18].

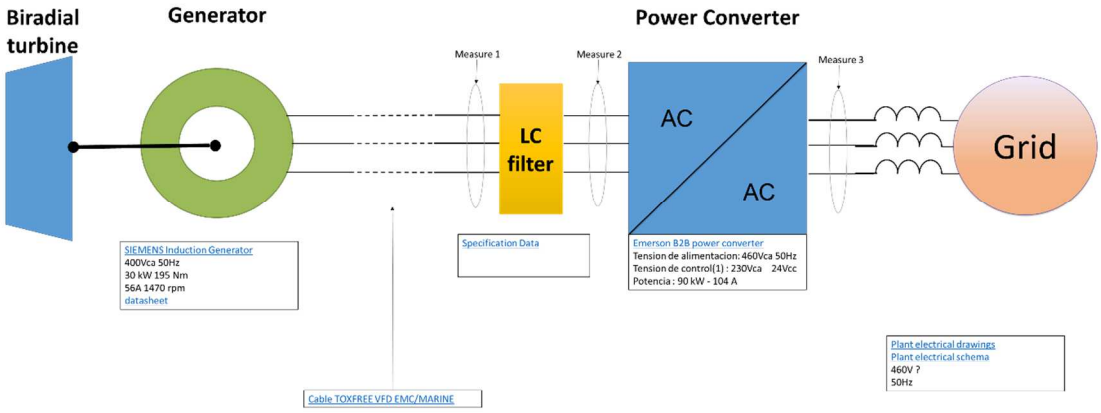

FIGURE 21. ELECTRICAL SETUP OF THE PTO INCLUDING THE 3 MEASUREMENT POINTS

So, with the objective of determining the total losses along the electrical chain, 3 measurement points are considered:

TABLE 8. MEASURE POINTS

Measurement	Electrical component
1	Filter input
2	Filter output/ B2B input
3	B2B output

At each measured point, values of the voltage levels, current magnitudes and power profiles have been recorded. At the same time, the power converter estimates electrical quantities at its input and output. The data of interest are labelled in the DB as it is shown in Table 9:

TABLE 9. LOCATION OF DATA IN DATABASE

Location	Label of electrical quantity
B2B Input	Drive 1 Total Current
	Drive 1 Out V
	Drive 1 Out Power
B2B Output	Regen Total Current
	Regen 1 Out V
	Regen 1 Out Power

The experiment was carried on for 5 days, the data represented here are collected from the two data sources:

- the estimated electrical values present in the database (DB)
- the measurement from the power analyser Yokogawa (YK)

A synchronisation process is required to improve the quality of data for comparison. It is done by cross-correlating the two data sources. So, with the objective of calibrating estimated values of the power electronics stored in the DB with the values measured by the YK, the three main electrical quantities of voltage, current and power are studied both at the input (drive) and output (regen) of the power electronics. A scatter plot is then obtained for each electrical quantity. An example of a one-hour sample is shown in Figure 22 comparing estimated versus measured values, while the ones in the regenerative side are presented in Figure 23.

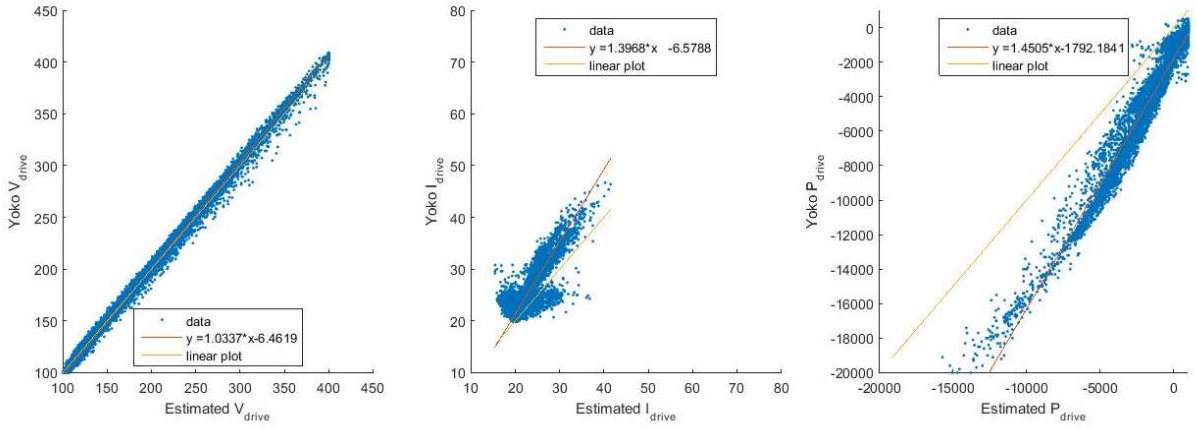

FIGURE 22. VOLTAGE, CURRENT AND POWER ESTIMATED VS MEASURED IN THE POWER ELECTRONIC (DRIVE SIDE)

Focusing on the voltage levels, the two set of data match and fit a linear relation. However, the values of the current present a strong dispersion, especially in low quantities, are not

correlated, and an underestimation can be witnessed. The way the current is estimated by the power electronic is questionable. As a result, and in this specific one-hour case, the power electronics underestimate by 25% the electrical power in comparison with the measurement. Note that the power is negative because by default, and as seen by the power electronics, the power flows from the grid to the electrical machine, in this case, negative power indicates the generator is producing and injecting current.

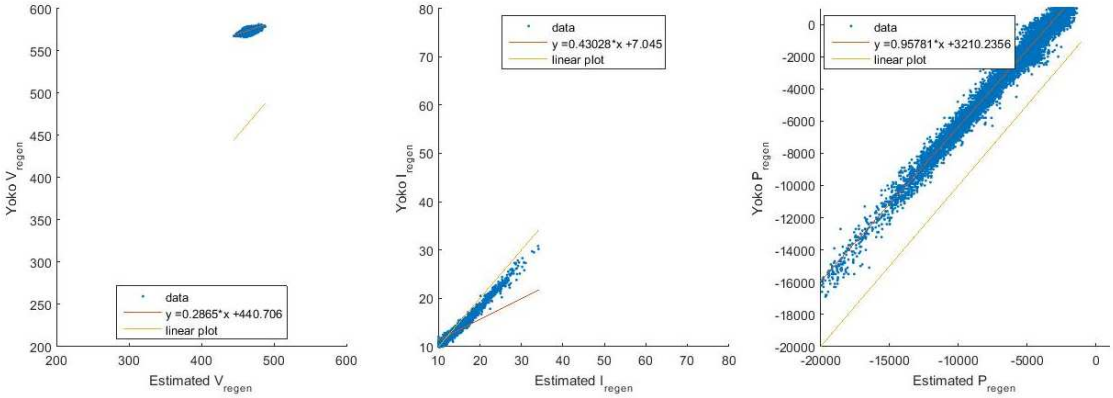

FIGURE 23. VOLTAGE, CURRENT AND POWER ESTIMATED IN THE POWER ELECTRONIC (REGEN SIDE)

On the contrary on the grid side, the power is overestimated and follow an offset, in this case, because the voltage level is not well represented.

When analysing the whole period of tests, there is statistical relevance to define a calibration relation to correct the estimated values. Figure 24 presents two power profiles from the two sources of data and a third one showing the corrected power applying a correlation calibration factor. The two scatter plots show on the left-hand side the estimated versus measured powers and on the right-hand side the corrected values of electrical power versus the measured one.

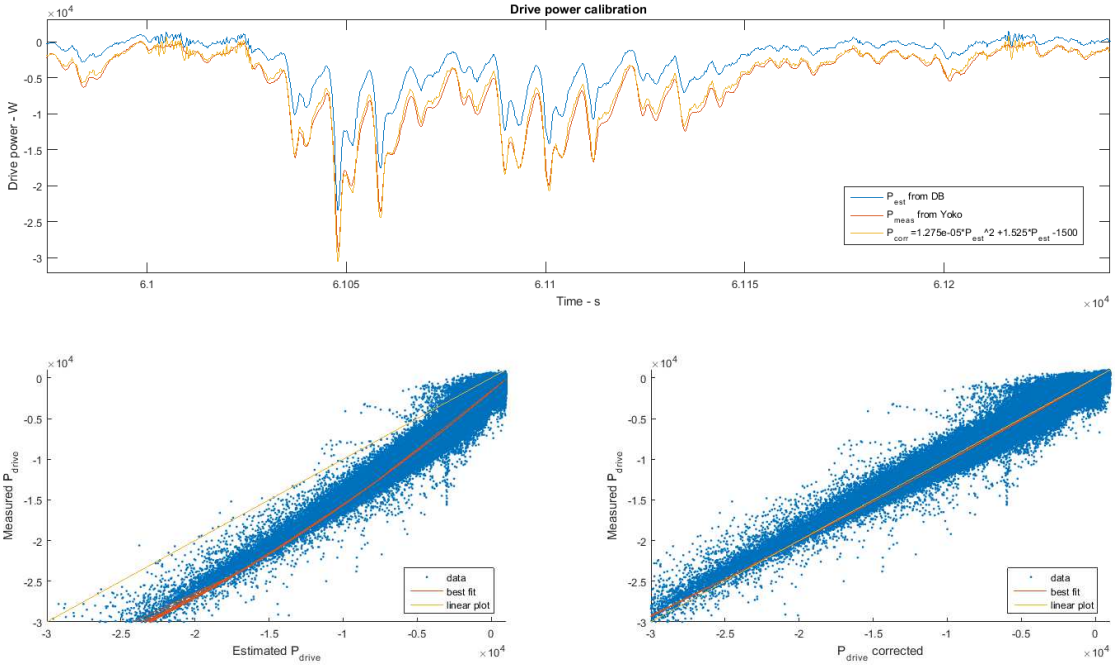

FIGURE 24. CALIBRATION OF ESTIMATED POWER – GENERATOR SIDE

Taking it in account, the following correction expression follows a polynomial defined by:

$$P_{drive,corr} = \mathrm{K}_1 P_{drive,est}^2 + \mathrm{K}_2 P_{drive,est} + \mathrm{K}_3 \quad (38)$$

Where $P_{drive,corr}$ is the corrected power and $P_{drive,est}$ the estimated one.

Correction constants are: $k_1 = 1.27e^{-5}\, W^{-1}$, $k_2 = 1.525$, $k3 = -1500\, W$

Making the same exercise for the grid side, the results can be observed in Figure 25.

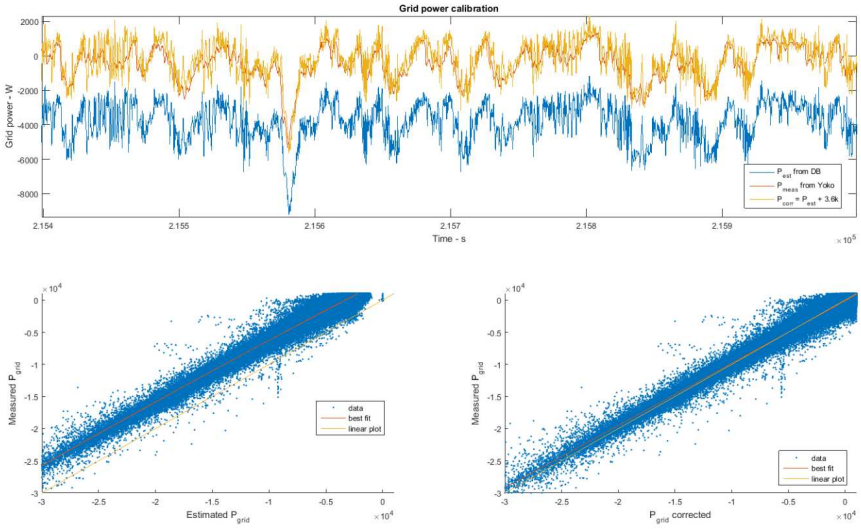

FIGURE 25. CALIBRATION OF ESTIMATED POWER – GRID SIDE

In this case, the correction expression is:

$$P_{regen,corr} = P_{regen,est} + \mathrm{K}_4 \quad (39)$$

With the constant $k_4 = 3600$ W.

This analysis brought in the issue of having reliable measurement equipment. In the next sections, data considering electrical values are corrected. Surely it is not the best approach when dealing with production data, and one shall bear in mind that still discrepancies can arise in the following analysis of results.

4.3 LOSSES ALONG THE ELECTRICAL CHAIN

Another activity achieved during the tests carried out with the power analyser is the characterisation of losses along the electrical chain from the generator to the power electronics output. From the 3 measurement points, the YK data allows to detail the filter losses (1) and the power electronics ones (2). The third value represents the total losses (3). Figure 26 shows the power levels at the 3 measurement points, being the lower figure a detailed view of the upper one.

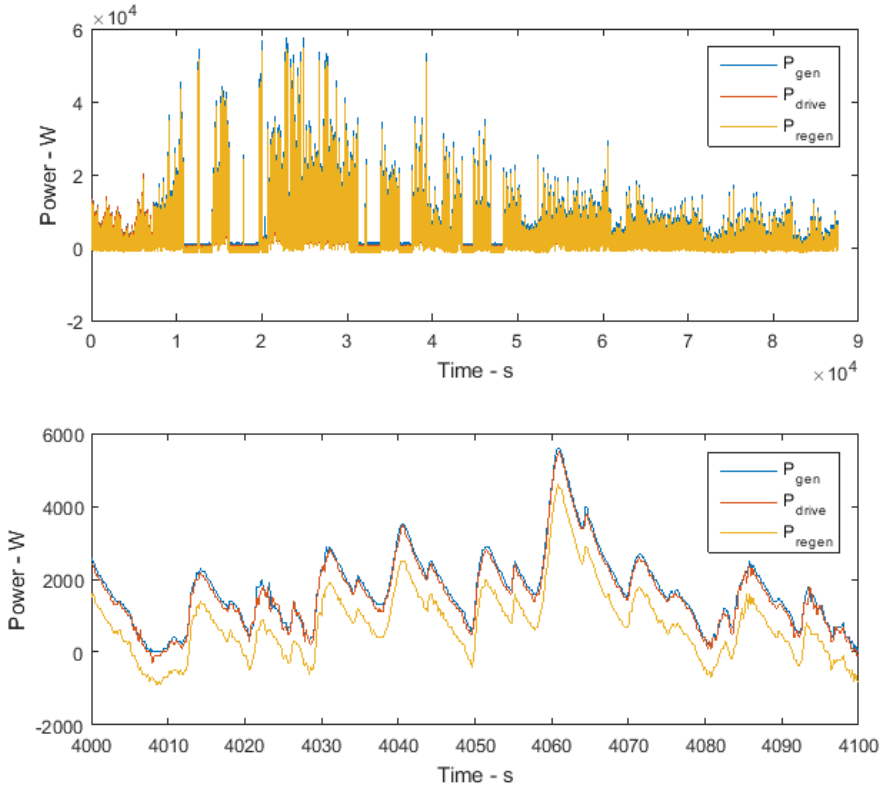

FIGURE 26. POWER IN THE 3 MEASURE POINTS (ZOOM AT LOWER GRAPHIC)

Figure 27 presents the efficiencies of the filter, the power electronics and the total efficiency. They are respectively calculated point by point:

$$\eta_{Fil} = P_{drive}/P_{gen} \qquad \eta_{PE} = P_{drive}/P_{regen} \qquad \eta_{tot} = \eta_{Fil}\,\eta_{PE}$$

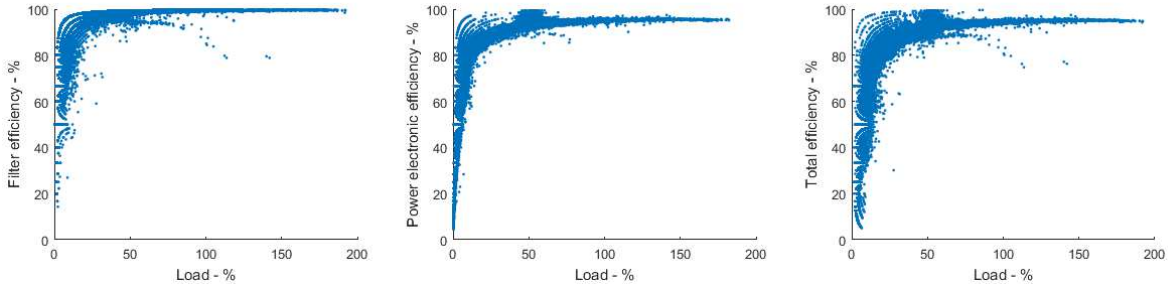

FIGURE 27. EFFICIENCY OF THE ELECTRICAL COMPONENTS

The profile of the efficiencies plotted in Figure 27 is typical of electrical equipment with low efficiency at low load and then a fast rise. At 25% of the load regime, the total efficiency is already over 80%. Note that the filter is more efficient than the power electronics and does not add too much electrical losses at rated capacity.

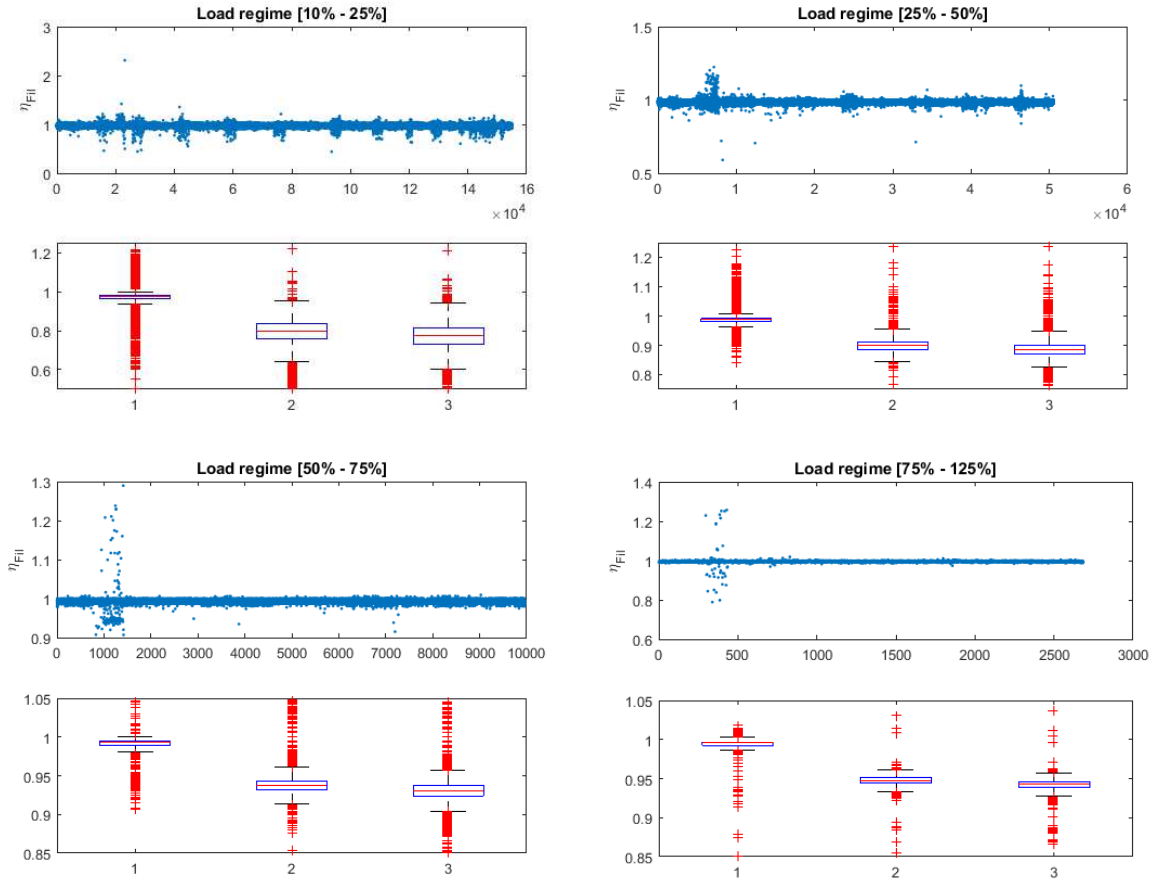

FIGURE 28. BOXPLOT OF THE FILTER (1), POWER ELECTRONICS (2) AND TOTAL EFFICIENCY (3) FOR DIFFERENT LOAD REGIMES

These figures focus on different load regimes, and for each, the efficiency point by point is plotted followed by a boxplot showing 1- the filter efficiency, 2- the PE and 3- the product of both. This representation is convenient because it shows the statistical representation of the dataset. It does not consider outliers (red crosses) that have no statistical relevance shows the max and min, the 2nd and 3rd quartiles representing ½ of the data are in the blue square, and finally the median is the red line.

Table 10 is based on the previous graphics and summarises the efficiencies:

TABLE 10. EFFICIENCIES AT DIFFERENTS LOAD RATIOS

Load Regimen	Filter efficiency	Power electronic efficiency	Total Efficiency
< 10%	0.9697	0.7727	0.7561
10-25%	0.9730	0.7955	0.7750
25-50%	0.9880	0.8981	0.8857
50-75%	0.9938	0.9375	0.9309
75-125%	0.9958	0.9474	0.9426
>125%	0.9959	0.9549	0.9510

After repairing the generator, the filter had to be added. Fortunately, the present results show a good performance of this component. Also, it is worth noting the power electronics adds a 10% of losses below half the rated capacity.

5. TESTING CALENDAR AND METHODOLOGY

The start of the sea trials of the advanced control algorithms in Mutriku Wave Power Plant was conditioned by previous activities. Figure 29 shows the complete calendar of works carried out. In November 2016, an offline pressure sensor measuring the wave elevation was installed in front of the plant. Although it does not provide real-time information, it permits to have resource data for the post-processing activities. This device was removed in May 2017, when it was discovered that, due to the leakage of a battery, it stopped recording at the beginning of February. It was repaired and, reinstalled in late January 2018 until it retrieval in June when it was found the sensor stopped recording in mid-April.

Starting in June 2017, the activities of installation and commissioning of the biradial turbine developed in WP3 were carried out. Everything was ready for starting the assessment of control strategies in the middle of July.

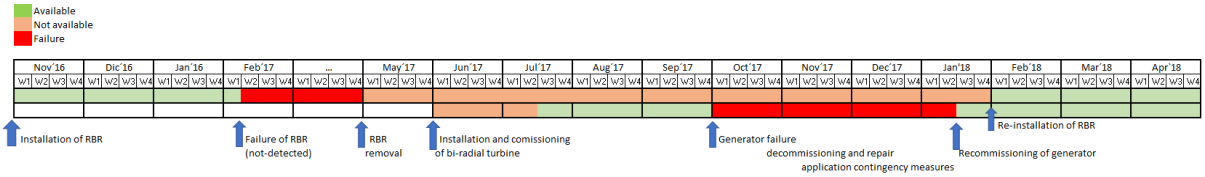

FIGURE 29. CALENDAR OF ACTIVITIES IN MUTRIKU

After two and a half months of continuous operation, a failure in the generator happened so the testing of CLs was interrupted. The works were resumed in January 2018, after the analysis of the failure, repairing works and recommissioning.

So, as a summary, the testing of CLs can be classified in two campaigns, during when the main activities are detailed in the next subsections:

- First campaign:
  - Started after the commissioning of the turbine and the correction of the issues related to the HSSV control.
  - Implementation, operation and tuning of algorithms CL1,2,5.
- Second campaign:
  - Started after the repair and re-commissioning of the electric generator plus installation of the filter
  - Coincide with the RBR installation until mid-April
  - Installation of the real-time wave measurement sensor at the beginning of June
  - Implementation of CL3, CL4, CL6.0 and CL6.1

The algorithms were tested sequentially and autonomously for 1/2h periods to allow comparison.

6. IMPLEMENTATION, TEST RESULTS AND ANALYSIS

During the 1-year period when the PTO was installed at Mutriku, the CLs were continuously tested over a wide variety of environmental conditions. They totalise 1841 hours of operation, equivalent to 77 consecutive days, and are distributed by each algorithm as it is shown in Table 11:

TABLE 11. OPERATION DATE AND DURATION OF CLS

CL#	Started operation	Hours
1	19/07/2017	500
2	19/07/2017	317
3	11/08/2017	216
4	23/04/2018	77
5	02/08/2017	247
6.0	19/01/2018	297
6.1	11/06/2018	188
Total hours of operation		1841

There were downtime periods because of plant issues and environmental conditions; the system was idle during storms and low energy sea states. Further to this, the PTO was unavailable from the end of September until mid-January due to a failure in the generator. In the presentation of results related to the PTO efficiency, two periods correspond are analysed: Phase I is before the generator failure and Phase II after the recommissioning.

6.1 CONTROL ARCHITECTURE FOR IMPLEMENTATION

When thinking of the implementation of the control algorithms to the control environment of the MWPP, not only the requirements regarding measurements are considered but also the algorithm complexity must be understood. Two groups can be divided: the CLs that are fully implemented into the logic controller and those requiring an external CPU. In the first case, the implementation is straightforward because only a few lines of code are implemented, this is the case for the CL1, CL2, CL3 and CL6.0. On the other case, the algorithms 4,5,6.1 were implemented in another computer present in the same network as the PLC. They used Matlab/Simulink models, quite similar to those used for the dry tests, where the I/O with the PLC was assured by an OPC server. This enables reliable real-time communication between the control computer running the CLs and the PLC. In Figure 30, the architecture of such a configuration is presented. The PLC sends the necessary measurements and variables to the Simulink model, where the control variable is processed and sent back to the PLC.

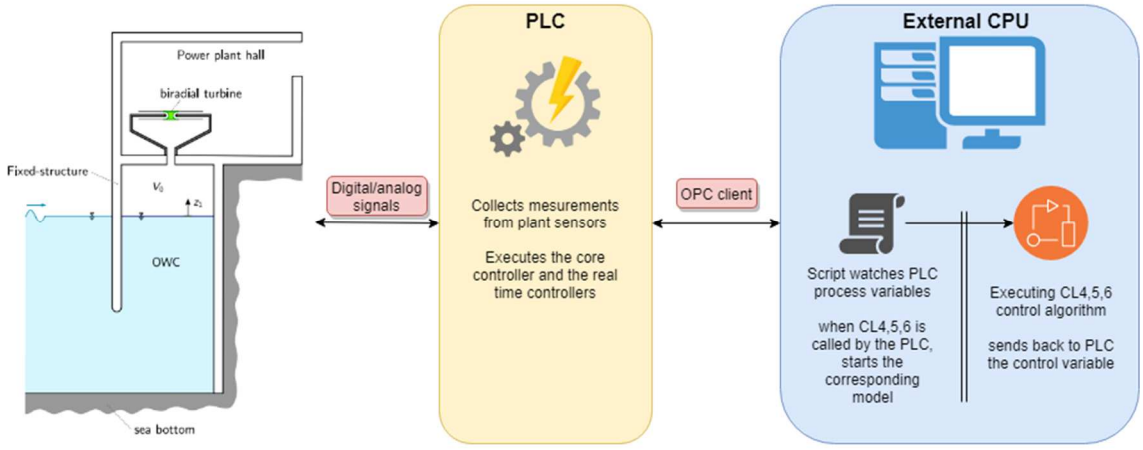

FIGURE 30. CONTROL ARCHITECTURE

One of the objectives of this WP is to offer a comparison of the performance of these algorithms. For that purpose, the control environment was programmed to run autonomously and automatically switched between the CL every 30 min and it is hoped that the environmental conditions do not change too much during a set of tests.

6.2 INTRODUCTION TO DATA ANALYSIS

6.2.1 RESOURCE AT THE MUTRIKU PLANT

Following the IEC standard TS62600-102 on power performance evaluation of ocean energy devices, it was decided to use a local measurement point. The equipment used and their location is detailed in section 2.1. There exist uncertainties linked to the measurement of the wave elevation using hydrostatic pressure sensors as described in Section 8.2. Still, the pressure sensor was the best compromise between accuracy, ease of deployment/maintenance and survivability to the harsh Winter season. Therefore, the results are conditioned by these uncertainties. This is not in the scope of WP4 to perform the most complete and accurate resource assessment. Figure 31 reveals the complexity of wave elevation measurements. The data from the SIMAR point are sea states estimated hourly by joining two numerical models (WAM and WaveWatch) and coupling it with a numerical weather model called HIRLAM [19]. This estimation is made on an area of 5 km, and the accuracy of such estimation is as good as the models used.

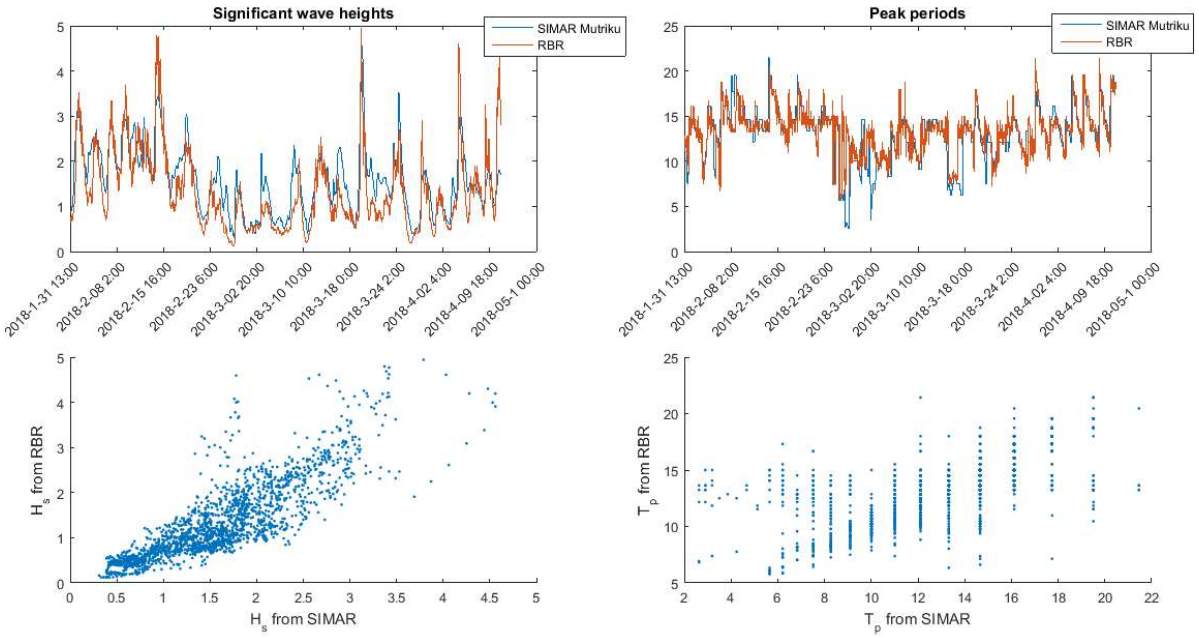

FIGURE 31. ATTEMPT TO CORRELATE THE TWO RESOURCES - SIMAR AND RBR

As stated in Section 5, the RBR/Virtuoso failed during its deployment. Due to the unavailability RBR wave elevation sensor during the overall testing period, the assessment and comparison of the control strategies are divided into 3 periods. It follows the availability of the wave resource from 3 different sources. The SIMAR point presents the benefit of covering the entire testing period but the wave climate is an estimation. This division of tests is supported by the fact that the local measured wave resource is to be the most reliable one. Another clarification, the data collection is limited to the second campaign, defined in the previous section. Table 12 presents the 3 periods along with the CL analysed and the source of the resource.

TABLE 12. PERIOD COVERED DURING CL TESTS

#	Period covered	CL assessed	Wave measurement
1	31-01-2018 to 18-04-2018	1 - 2 - 3 - 5 - 6.0	Offline RBR/Virtuoso pressure sensor
2	23-04-2018 to 31-05-2018	1 - 4	SIMAR Point # 3171032 – Puertos del estado
3	11-06-2018 to 24-06-2018	1 - 6.1	Online ISURKI pressure sensor

One objective of the WP is to compare the algorithms and, for that purpose, CL1 was selected to be the baseline. That is why in each of the 3 testing periods the aim is to present the electrical production of CL1 regarding sea states and the results comparing the other CLs with this base case.

One must keep in mind that the PTO was designed to be tested in the Oceantec buoy. In that sense, the objective of the Mutriku testing is the de-risking of the turbine and generator.

Design parameters for both the turbine and the generator are optimized for the buoy. For example, the generator was selected to fit the offshore resource and the production of the Marmok A5. Its nominal capacity is 30 kW while those coupled to the Wells turbines already installed are 18.5 kW of rated power. When analysing electrical production, the reader is asked to remember that fact. In respect to WP4, the Mutriku testing phase allows validating the feasibility of implementing these algorithms and operate the PTO safely. Also, this stage allows to have a hint about the most promising control strategies to be soon integrated into the Marmok A5.

6.3 ASSESSMENT OF CL COVERING THE DEPLOYMENT OF THE RBR WAVE SENSOR

According to the IEC TS62600-102, the performance is to be evaluated using power matrices where the performance is shown as a function of the resource. The axes are the wave heights and periods, and a bin shows performance values (efficiencies, electrical power). The methodology employed to obtain the wave statistic was to:

- obtain the timestamp of beginning and end of a test
- select the raw data of water elevation for this period
- correct the tide level with the mean to get the wave elevation
- perform spectral analysis and obtain the significant wave height H_s and the energy period T_e. The full process is soon to be reported in a deliverable in the scope of WP1.

Each sea state is then defined by bins of ½ m of H_s and 1 s period T_e. During the 2.5 months period of winter when the RBR was installed, the sea state occurrence is shown in Figure 32.

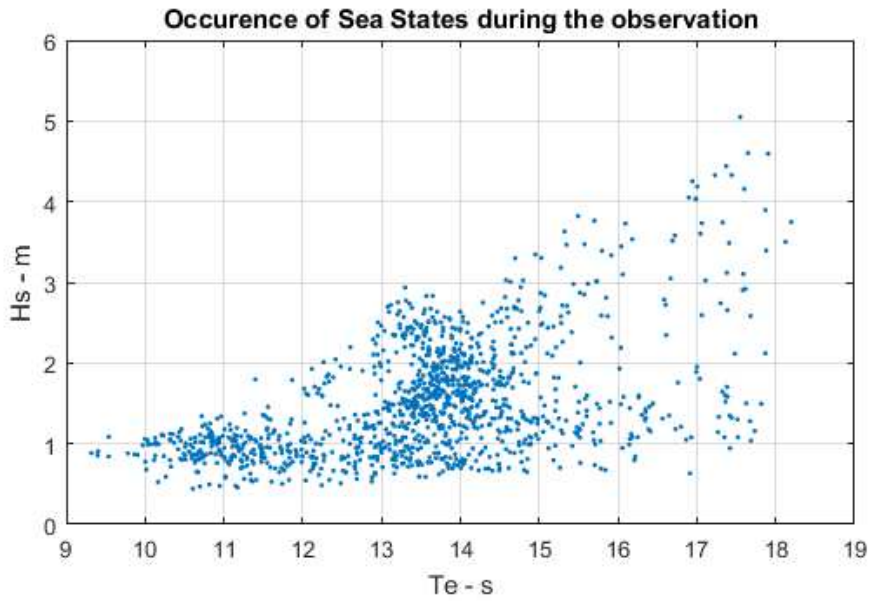

FIGURE 32. SEA STATE OCCURRENCE DURING THE RBR INSTALLATION

If applying the IEC standard, there are 49 different sea states during which 5 control laws were operative. When focusing on each sea states, and due to the wide variety of sea states, some have very few results and thus do not show statistical relevance. Instead, a clustering method was used to group the sea states. The K-means approach was used based on a squared Euclidian distance algorithm, the number of clusters (20 sea states) was selected, so each CL was sufficiently represented for each sea state.

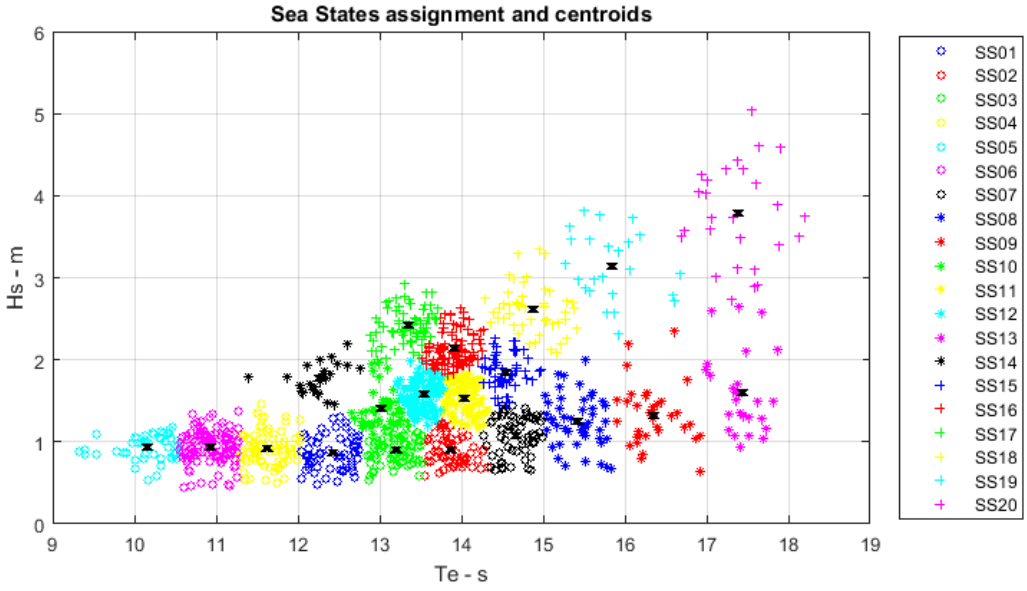

FIGURE 33. GROUP OF SEA STATES

Table 13 represents the wave climate during the period 31/01 to 18/04 2018 at Mutriku.

TABLE 13. SEA STATE REPRESENTATION

SS	Hs (m)	Te (s)	N. of element	Occurrence (%)
1	0.87	12.42	45	3.72
2	0.90	13.87	110	9.09
3	0.90	13.20	80	6.61
4	0.92	11.63	61	5.04
5	0.93	10.15	24	1.98
6	0.94	10.93	72	5.95
7	1.08	14.66	46	3.80
8	1.25	15.42	70	5.79
9	1.33	16.35	63	5.21
10	1.40	13.01	116	9.59
11	1.54	14.03	96	7.93
12	1.58	13.53	101	8.35
13	1.61	17.43	54	4.46
14	1.78	12.25	62	5.12
15	1.85	14.54	47	3.88

16	2.14	13.90	49	4.05
17	2.43	13.34	25	2.07
18	2.62	14.86	35	2.89
19	3.14	15.83	28	2.31
20	3.79	17.37	26	2.15
TOTAL NUMBER OF TESTS			**1210**	**100.00**

Among these 1210 1/2h-tests, the repartition of tests between the CL is the following:

TABLE 14. NUMBER OF TESTS PER CL

CL	N. of element
1	255
2	278
3	252
5	250
6.0	280

6.3.1 CONTROL LAW CL1

6.3.1.1 IMPLEMENTATION

This section presents the behaviour of CL1 by showing the time series of the main operational data. The control law parameters used in the tests presented were defined not to optimised the turbine and generator powers but to reduce the number of operation of the high-speed safety valve. The data are collected from the DB and present plant condition quantities and PTO operational values. The graphs are taken during a sea state $H_s = 3$ m and $T_e = 15$ s which is a quite energetic sea state and, though it is not a typical test, it allows to understand the behaviour of the control algorithm in terms of torque and power levels, amplitude of rotational speed and HSSV actuation. In these conditions, the damper valve was opened at 30°, – a third of its total course - to dissipate part of the energy and continue operating. Still the HSSV operates when the rotational speed reaches 220 rad/s. In Figure 34, it is noticeable there is a reliance on the safety valve as the upper threshold speed is often reached and force the HSSV to often close. The torque is kept low so the electrical power does not overshoot its nominal capacity, which is the objective of the peak-power control. Regarding implementation into the control environment, this is the simplest to program and it only relies on the turbine speed.

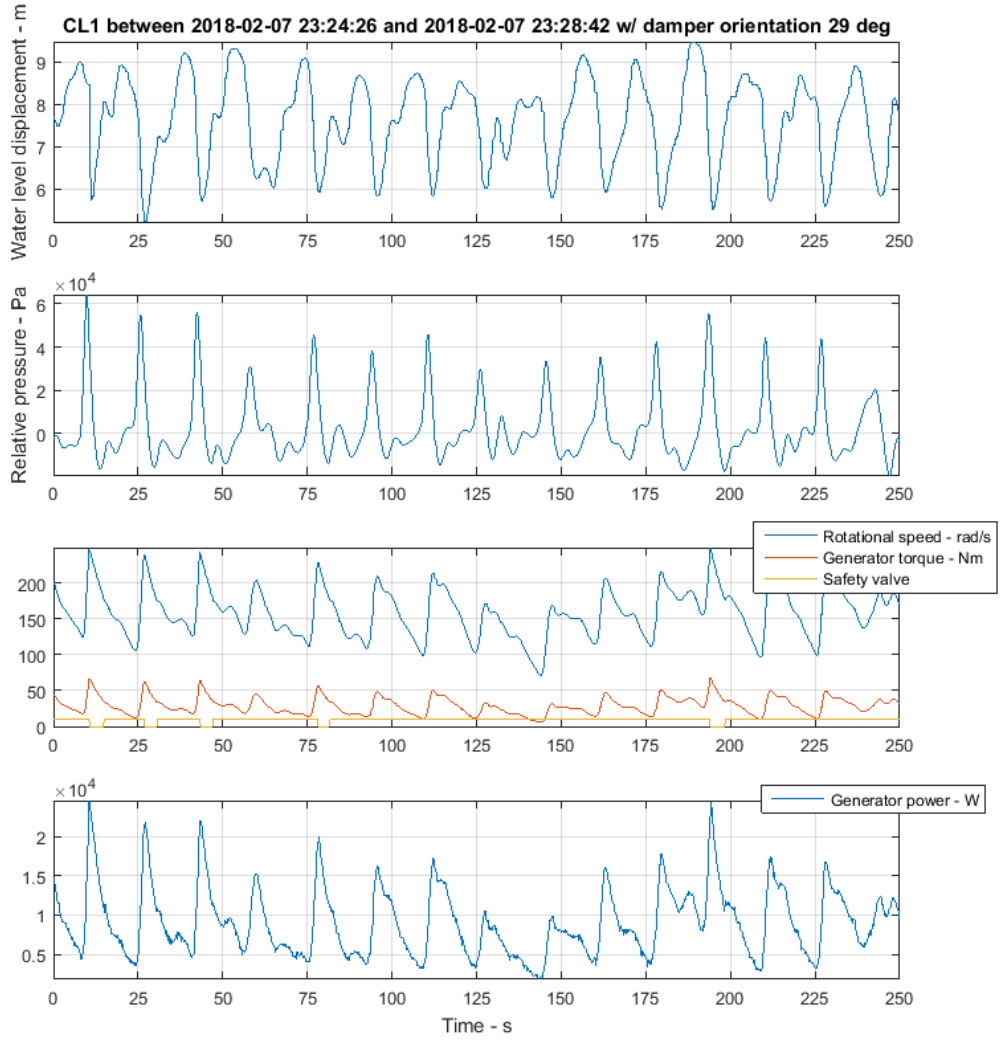

FIGURE 34. CL1 OPERATION DURING A SEA STATE $H_s = 3\ m$ AND $T_e = 14.80s$

6.3.1.2 OPERATION RESULTS

6.3.1.2.1 PERFORMANCE

Figure 35 shows the average electrical powers produced when using CL1. Each sea state covers between 2 and 22 1/2h tests for a total of 255. The boxplot representation is a good way to understand the operational results of the algorithms. The average of all the average powers are represented by the marker - * - the blue squares gather half of the results, the minimum and maximum values are shown with the black horizontal lines, and finally, the outliers are the red crosses.

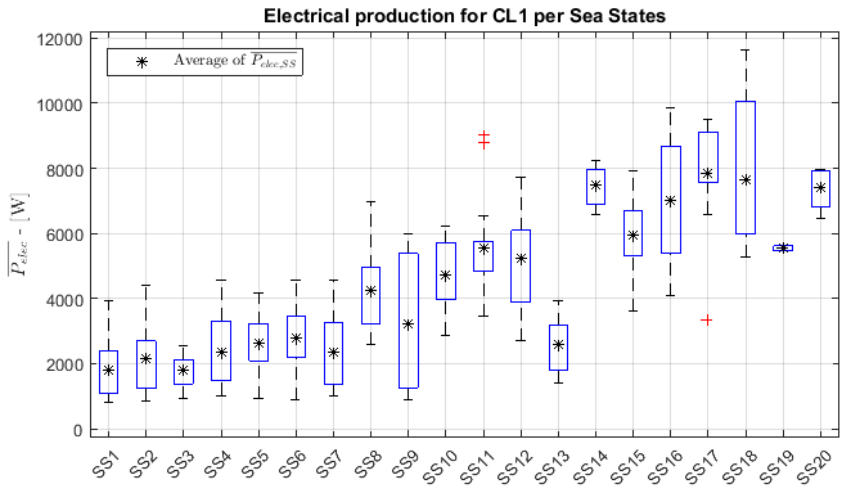

FIGURE 35. ELECTRICAL PRODUCTION FOR CL1 PER SEA STATE

One can observe a high standard deviation of average powers for the same sea state. Although in some cases there is not much dispersion as in SS3, 5, 11, 14; some sea states like the #9 vary from the simple to 6 times more. There can be many explanations for this dispersion of results:

- The clustering of results. Adding more sea states will reduce the uncertainty and by the same the number of tests to be statistically compared. When looking at the clustering of SS9, the wave heights are in the interval [0.5:2.5]m and because incident wave energy is proportional to the square of H_s the dispersion in power outputs is large. It is also the case for SS8, 9, 13, 17, 18, 19 and 20. On the contrary the, other SS are quite close to the IEC standard.
- The variation of environmental conditions like the tide level, changing the air chamber volume; or the wave direction.
- The spectral shape of the sea states. Looking at the wave spectrum of similar sea states, they can have strong differences (multi-peaks, peakedness, narrow-bandness

6.3.1.2.2 RELIABILITY

The analysis has been performed along 527 tests of 30 min each one, resulting in a total of 15,810 min in operation. Among these tests, the following extremal operation has been reached:

- Overspeed (Ω > 230 rad/s):
  - Total duration: t = 208 s
  - % of total operating time in overspeed: 0.022 %
  - Number of times reached: 69
  - Duration < 10 s: 65 times
  - Duration 10.1 < t < 30 s: 4 times
  - Duration > 30.1 s: 0 times
  - Maximum speed reached: 263.99 rad/s

- Overload in Power (P > 30 kW)
  - Total duration: t = 29.50 s
  - % of total operating time in power overload: 0.003 %
  - Number of times reached: 24
  - Duration < 10 s: 24 times
  - Duration 10.1 < t < 30 s: 0 times
  - Duration > 30.1 s: 0 times
  - Maximum power reached: 33.83 kW

- Overload in Torque (T > 200 Nm)
  - Number of times reached: 0
  - Maximum torque reached: 152.20 Nm

- Overtemperature (T > 70 ^{o}C)
  - Number of times reached: 0
  - Maximum temperature reached: 62.50 ^{o}C

6.3.1.2.3 POWER QUALITY

In the actual setup and with the frequency the data are collected, power quality as usually referenced to cannot be defined in terms of voltage and current variations to measure fluctuations, flicker of harmonic distortion. Instead, the quality of power produced is evaluated regarding standard deviations and peak-to-average (Pk2avg) power ratios. First, the standard deviation to know the variations of power levels, and the Pk2avg to tell what is the maximum power with respect to the average production. Both parameters are represented in function of the average electrical power and for both the generator and the grid power. Low values for these parameters imply a better power quality, especially for significant average power.

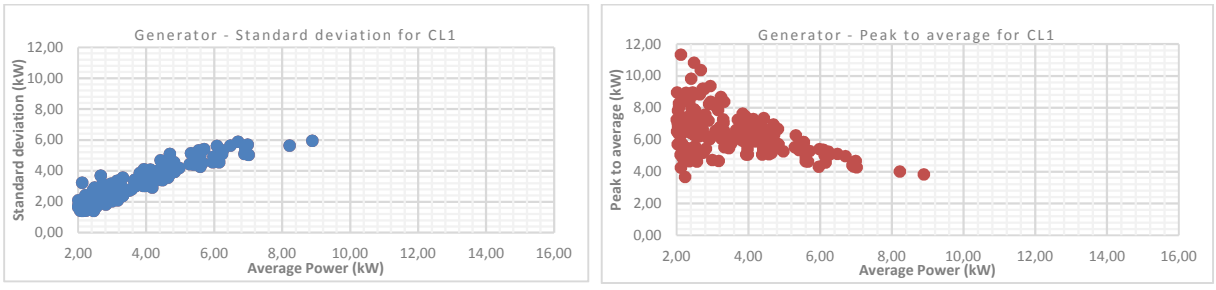

FIGURE 36. STANDARD DEVIATION AND PEAK TO AVERAGE OF GENERATOR POWER IN FUNCTION OF AVERAGE POWER FOR CL1

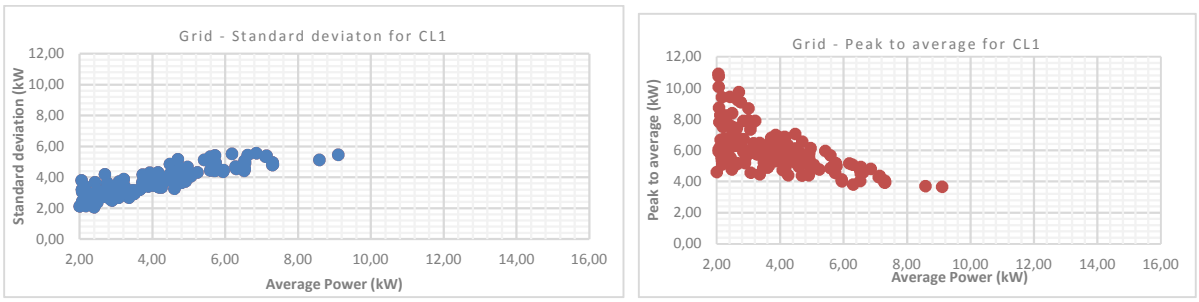

FIGURE 37. STANDARD DEVIATION AND PEAK TO AVERAGE OF GRID POWER IN FUNCTION OF AVERAGE POWER FOR CL1

6.3.2 CONTROL LAW CL2

6.3.2.1 IMPLEMENTATION

As for CL1, the time series of operational data is presented in the next Figure 38. Unlike the other turbine control laws which depend on turbine speed, CL2 is based on air chamber pressure to compute the applied electrical torque. In this specific test, the damping valve is half closed, and the sea state is equivalent to #19 in Table 13. Because this law uses values of instantaneous pressure along with average pressure, it is the fastest to respond to any change in the chamber and applies a braking torque before the energy is converted from pneumatic to mechanical and thus accelerates the turbine. In contrast, controllers based on rotational speed is more acting in reaction to the energy coming into the system after it is transformed into mechanical power.

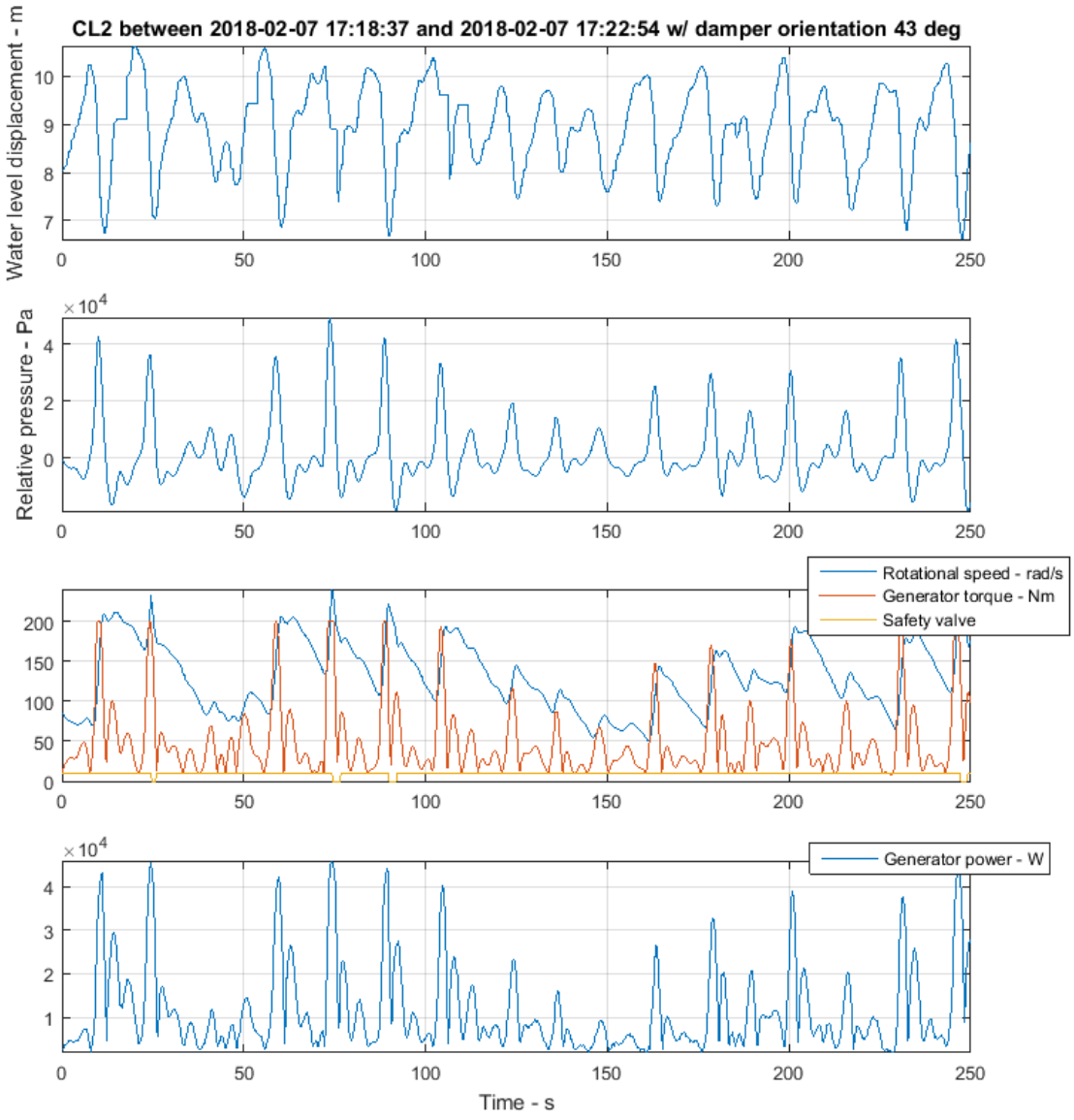

FIGURE 38. CL2 OPERATION DURING A SEA STATE $H_s = 2.80\ m$ AND $T_e = 14.90\ s$

In this figure it is also important to highlight the safe PTO operation. Some safety thresholds are reached and attest to the correct operation of the plant safety control (common to all CL). When focusing on the rotational speed, we observe peaks around 250 rad/s at 25s, 75s, 90s when the HSSV valve closes and opens back after the speed goes below 180 rad/s. This eventually prevents the turbine from overspeeding and reaching the generator runaway speed. In various cases, the nominal torque is also reached – 200 Nm – but never overshot. Finally, the generator presents short-time peaks of power above its rated power due to the operation at rotational speeds higher than the nominal. The generator can withstand these levels of power as long as the winding temperature does not reach its limit (insulation class H 180° C), which was never the case during the entire testing period.

6.3.2.2 OPERATION RESULTS

6.3.2.2.1 PERFORMANCE

Figure 39 is a summary of the operation of CL2 where all mean powers are normalised against the mean values of average electrical powers from CL1.

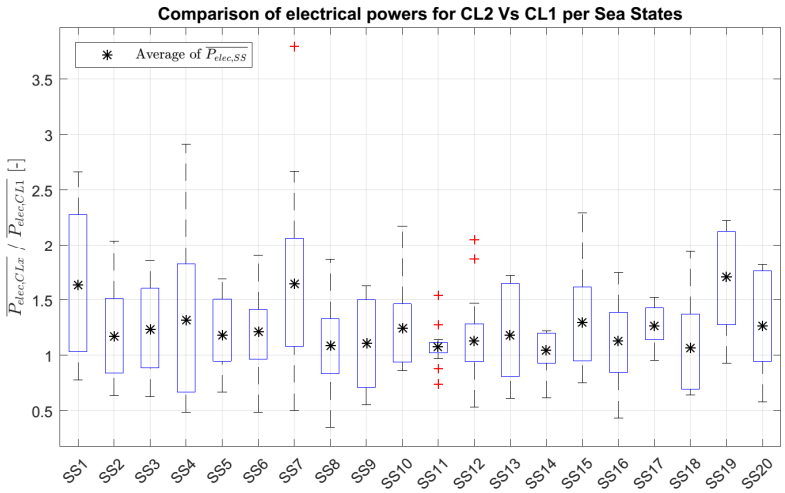

FIGURE 39. ELECTRICAL PRODUCTION OF CL2 COMPARED TO CL1

When focusing only on the mean of the average electrical powers, the most relevant observation here is that are for all sea states the average electrical power output is higher than the average of CL1 varying from 4% to 70% with a mean of 22%. Still, there is the same dispersion of results, but even when looking at the lower quartile, none is lower than 0.75% the average of CL1. It is particularly more efficient on low and high sea states with an overwhelming performance on SS1, SS7 and SS19.

6.3.2.2.2 RELIABILITY

The analysis has been performed along 466 tests of 30 min each one, resulting in a total of 13,980 min in operation. Among these tests, the following extremal operation has been reached:

- Overspeed (Ω > 230 rad/s):
  - Total duration: t = 330.75 s
  - % of total operating time in overspeed: 0.057 %
  - Number of times reached: 87
  - Duration < 10 s: 78 times
  - Duration 10.1 < t < 30 s: 9 times
  - Duration > 30.1 s: 0 times
  - Maximum speed reached: 262.74 rad/s

- Overload in Power (P > 30 kW)
  - Total duration: t = 4690 s
  - % of total operating time in power overload: 0.56 %
  - Number of times reached: 152
  - Duration < 10 s: 69 times
  - Duration 10.1 < t < 30 s: 33 times
  - Duration > 30.1 s: 50 times
  - Maximum power reached: 46.95 kW

- Overload in Torque (T > 200 Nm)
  - Number of times reached: 0
  - Maximum torque reached: 200 Nm (imposed limit)

- Overtemperature (T > 70 ^{o}C)
  - Number of times reached: 0
  - Maximum temperature reached: 68.10 ^{o}C

6.3.2.2.3 POWER QUALITY

Figure 40 and Figure 41 present indicators of power quality when using CL2, in terms of standard deviation and peak to average power for both output electric power in the generator and electric power sent to the grid.

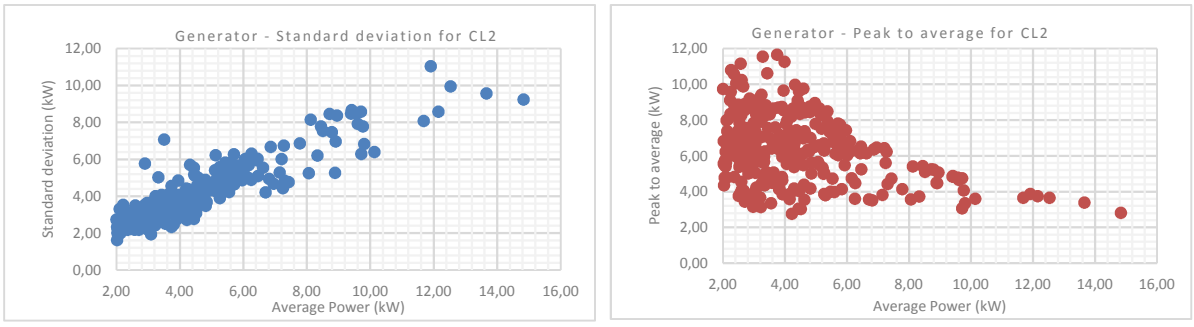

FIGURE 40. STANDARD DEVIATION AND PEAK TO AVERAGE OF GENERATOR POWER IN FUNCTION OF AVERAGE POWER FOR CL2

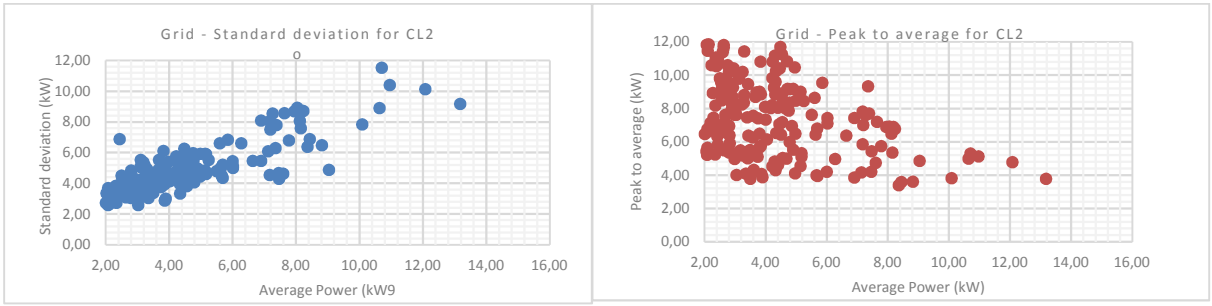

FIGURE 41. STANDARD DEVIATION AND PEAK TO AVERAGE OF GRID POWER IN FUNCTION OF AVERAGE POWER FOR CL2

6.3.3 CONTROL LAW CL3

6.3.3.1 IMPLEMENTATION

In terms of implementation, this control law is directly programmed in the PLC. It relies on values of relative pressure to determine the open and closed position of the HSSV. Then a speed control similar to CL1 is employed for the turbine control. The CL3 is a latching control where the valve operation is defined by values of pressure and based on a latching time, function of the energy period. In the actual setup, the period had to be manually entered, which was inconvenient, while it was supposed to be provided by the real-time wave sensor. One of the weaknesses of this control is that the valve can stay close because of a wrongly selected latching time. In Figure 42, although there is a highly energetic sea state, in repeated cases, the valve is shut-off while the pressure half cycle (bringing energy) is already gone. Worse, the generator has to be motored (negative generator power) to keep the rotational speed above 50 rad/s. Later on, the algorithm was modified only to activate itself in the most relevant cases, when the instantaneous pressure is higher than a threshold of average pressure.

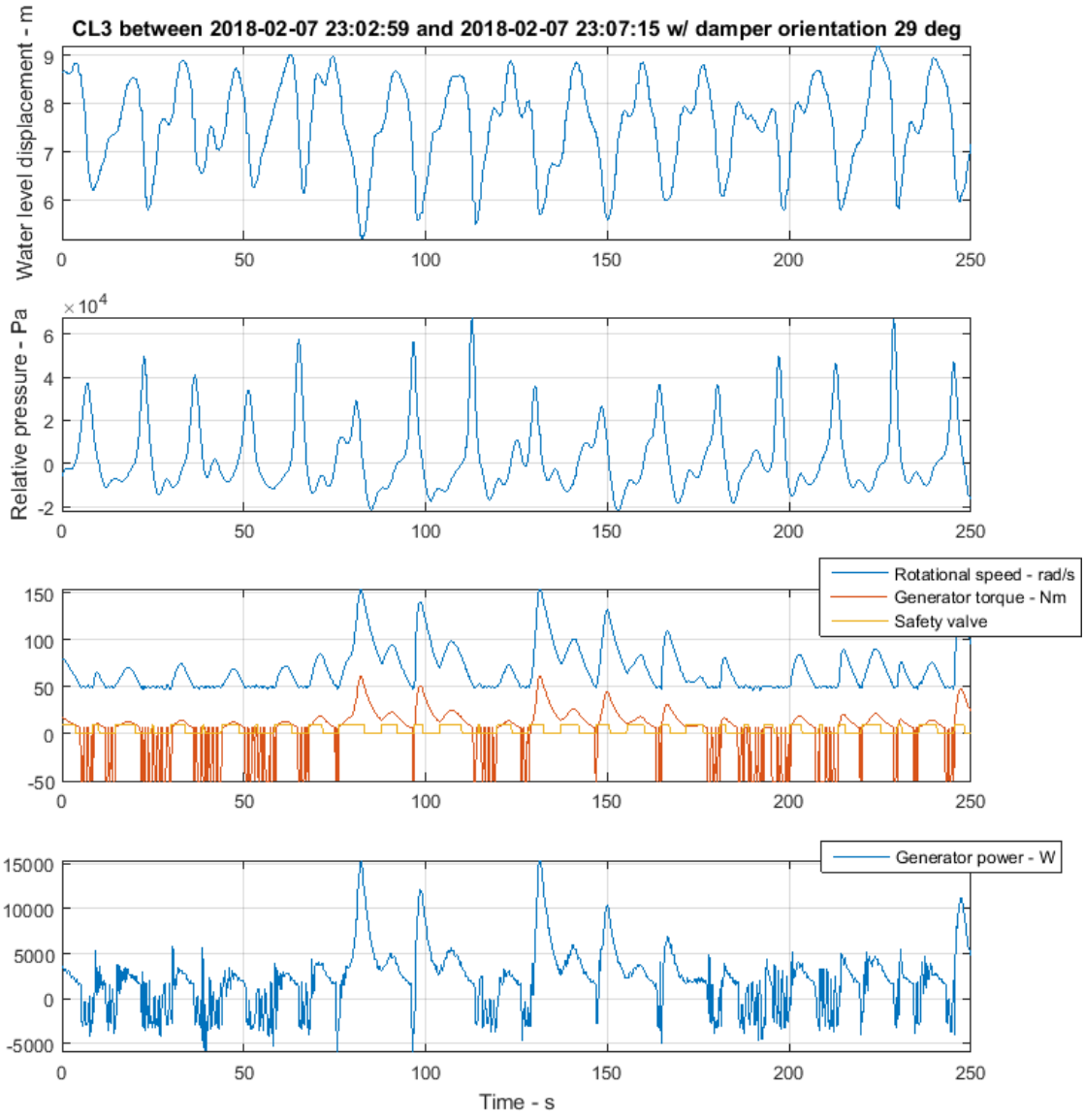

FIGURE 42. CL3 OPERATION DURING A SEA STATE $H_s = 3\ m$ AND $T_e = 15s$

6.3.3.2 OPERATION RESULTS

6.3.3.2.1 PERFORMANCE

Figure 43 presents the results of the CL3 adaptive latching strategy.

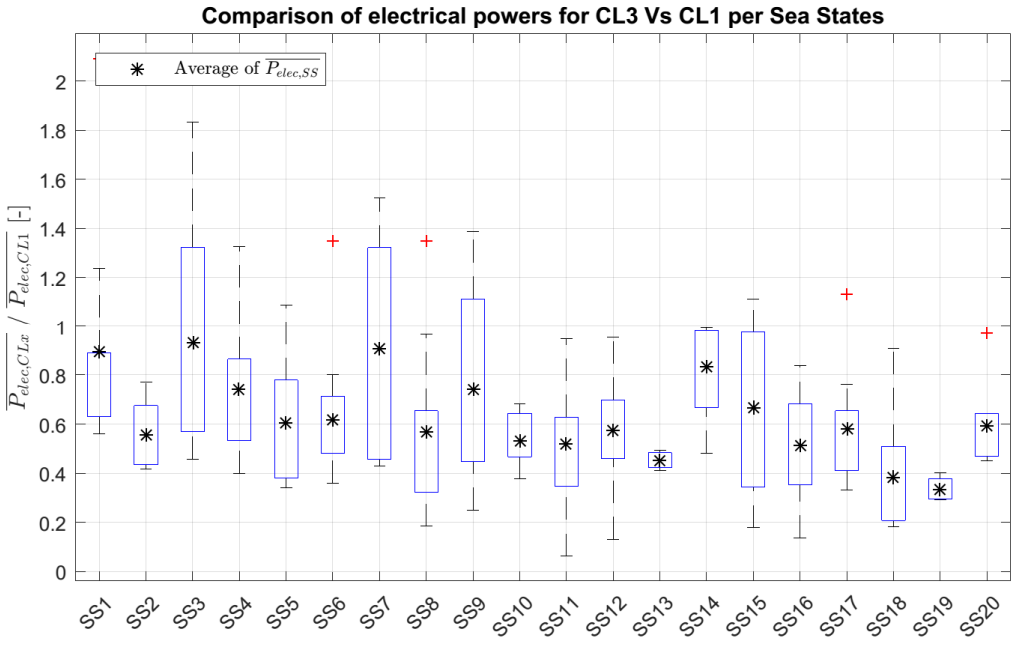

FIGURE 43. ELECTRICAL PRODUCTION OF CL3 COMPARED TO CL1

As expected after the Task 4.1 and 4.2, the resulting power convertion was poor and none of the sea states even equals the base case on average. When computing the average (weighted with the SS occurrence), this law produces 37% less than CL1. In the best case the production hardly meets the one of CL1 and in the worst case in SS19 this CL produces a third than the base case. At the origin this latching control was developed for a rigid PTO. A latching control strategy based on latching times fixed by sea states is not adapted for an OWC. This behaviour was already foreseen during the previous activities of WP4 and conclusions presented on the deliverable D4.1 [10] attest the irrelevance of latching control for the MWPP because of the proper geometry of the air chambers. When looking at the RAOs of motion, the plant already amplifies the waves during the main wave periods. Thus, the resonance effect aimed by the controller does not occur. It is fair to say that CL3 in its present configuration should be given low priority for the tests in the Marmok A5.

6.3.3.2.2 RELIABILITY

The analysis has been performed along 423 tests of 30 min each one, resulting in a total of 12,690 min in operation. Among these tests, the following extremal operation has been reached:

- Overspeed (Ω > 230 rad/s):
  - Total duration: t = 430.25 s
  - % of total operating time in overspeed: 0.056 %
  - Number of times reached: 90
  - Duration < 10 s: 78 times
  - Duration 10.1 < t < 30 s: 12 times
  - Duration > 30.1 s: 0 times
  - Maximum speed reached: 264.20 rad/s

- Overload in Power (P > 30 kW)
  - Total duration: t = 125 s
  - % of total operating time in power overload: 0.016 %
  - Number of times reached: 65
  - Duration < 10 s: 63 times
  - Duration 10.1 < t < 30 s: 2 times
  - Duration > 30.1 s: 0 times
  - Maximum power reached: 46.37 kW

- Overload in Torque (T > 200 Nm)
  - Number of times reached: 0
  - Maximum torque reached: 200 Nm

- Overtemperature (T > 70 ºC)
  - Number of times reached: 0
  - Maximum temperature reached: 66.4 ºC

6.3.3.2.3 POWER QUALITY

Figure 44 and Figure 45 present indicators of power quality when using CL3, in terms of standard deviation and peak to average power for both output electric power in the generator and electric power sent to the grid.

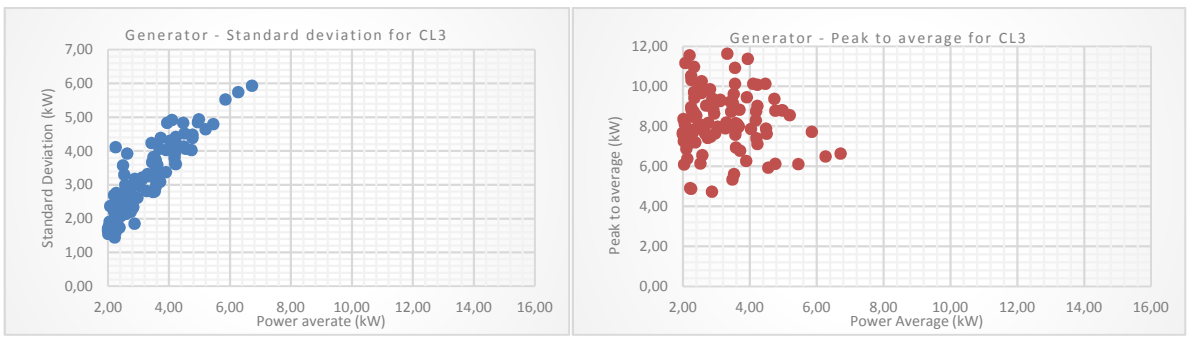

FIGURE 44. STANDARD DEVIATION AND PEAK TO AVERAGE OF GENERATOR POWER IN FUNCTION OF AVERAGE POWER FOR CL3

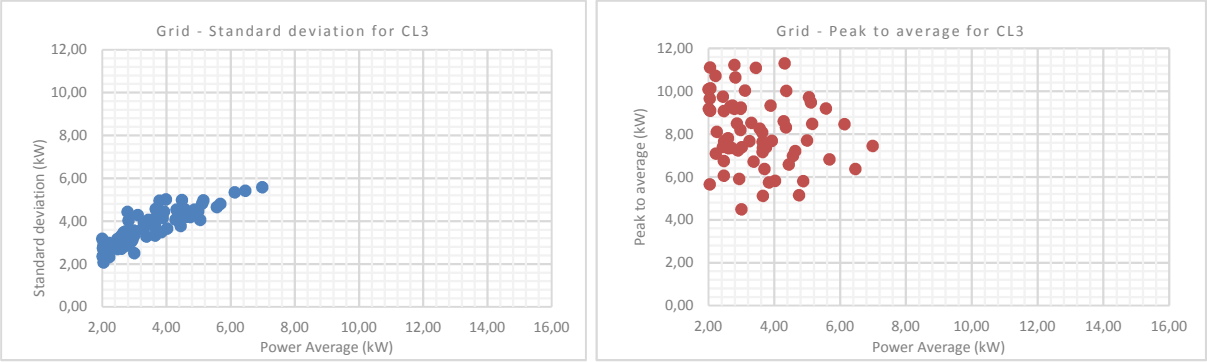

FIGURE 45. STANDARD DEVIATION AND PEAK TO AVERAGE OF GRID POWER IN FUNCTION OF AVERAGE POWER FOR CL3

6.3.4 CONTROL LAW CL5

6.3.4.1 IMPLEMENTATION

The control law 5 is based on a reinforcement learning algorithm. This control law relies on a level of complexity requiring the use of an additional PC to perform the computation of the control parameters. When operating, this algorithm tests a number of control parameters and observe the response regarding generated power. The parameters are scored and ranked while the algorithm is learning. The learning process, embedded in the training matrices, is saved, as well as the last control parameters, after each 1/2h test. That way when the CL is called again, it can continue its learning. Figure 46 shows the main operational data as the previous CL. This shows a typical turbine speed control based on a torque law, similar to CL1.

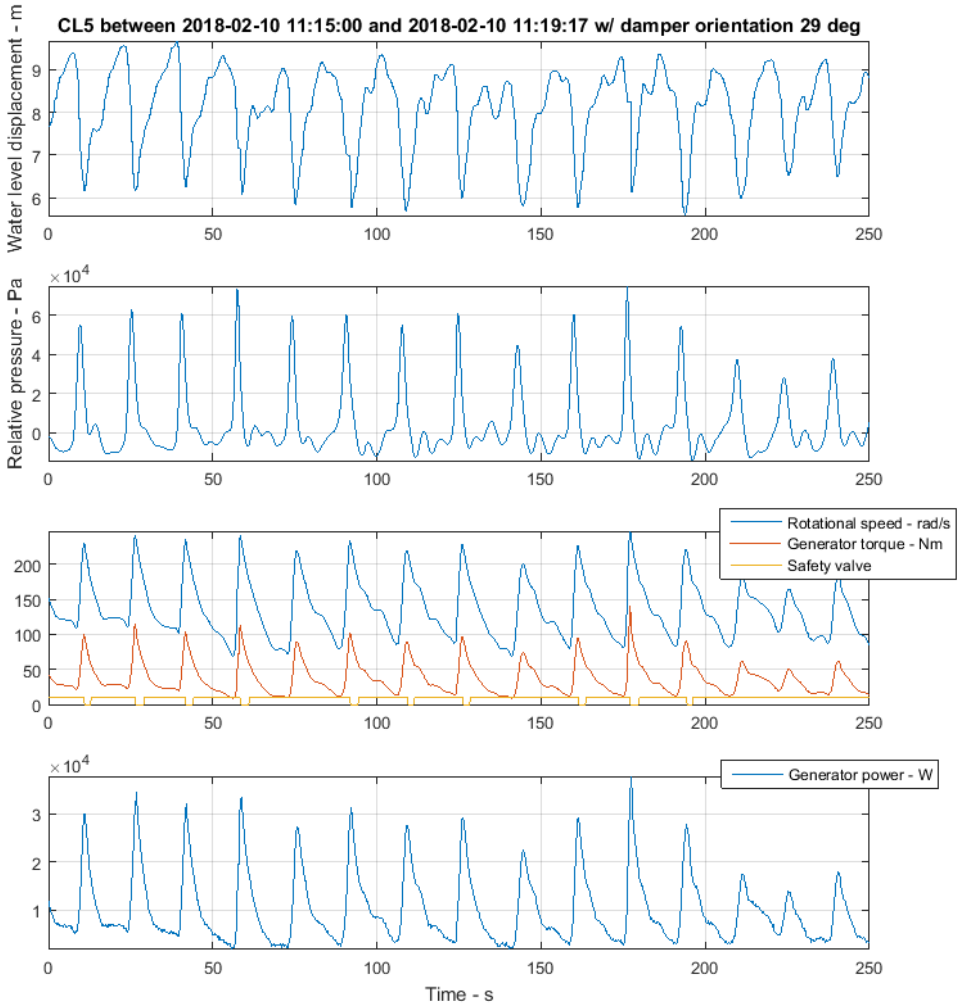

FIGURE 46. CL5 OPERATION DURING A SEA STATE $H_s = 3.5\ m$ AND $T_e = 15.7s$

Figure 47 shows an evolution of the slope parameter in the torque law after it had been reset, but not the training matrices. The parameter tests few parameters after converging to its best historical values proving the algorithm is already trained.

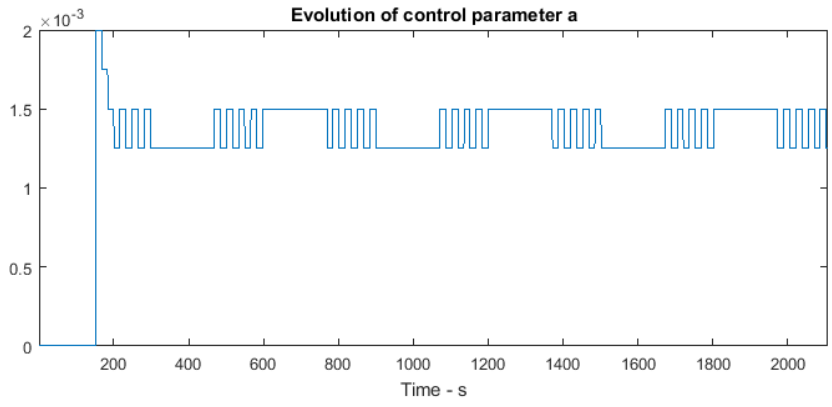

FIGURE 47. EVOLUTION OF CONTROL PARAMETER A

The main advantage is that this CL learns without using any numerical model so it's not subject to possible inaccuracy. On the other hand, one drawback is that the algorithm needs time to be trained and converge to an optimal; optimal for its training period and so sensitive to changes of sea states.

6.3.4.2 OPERATION RESULTS

6.3.4.2.1 PERFORMANCE

The results presented in Figure 48 Figure 47show the comparison of CL5 against CL1. There is an improvement in the average generated power in most of the sea states, except for SS8 10 and 18. The best performance is reached for SS7 and SS19. When averaging the increase of mean power production of all sea states and weight it with their occurrence, we can state CL5 performs better than CL1 by 10%.

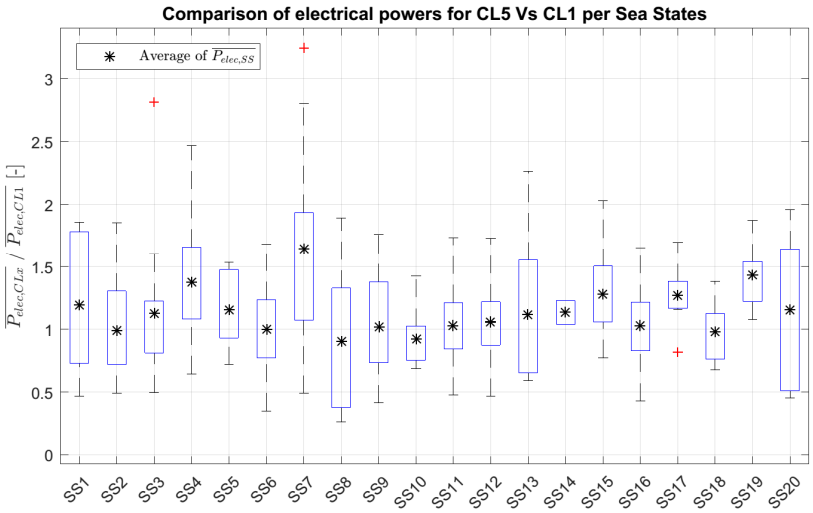

FIGURE 48. ELECTRICAL PRODUCTION OF CL5 COMPARED TO CL1

6.3.4.2.2 RELIABILITY

The analysis has been performed along 428 tests of 30 min each one, resulting in a total of 12,840 min in operation. Among these tests, the following extremal operation has been reached:

- Overspeed (Ω > 230 rad/s):
  - Total duration: t = 901 s
  - % of total operating time in overspeed: 0.117 %
  - Number of times reached: 120
  - Duration < 10 s: 91 times
  - Duration 10.1 < t < 30 s: 24 times
  - Duration > 30.1 s: 5 times
  - Maximum speed reached: 262.98 rad/s

- Overload in Power (P > 30 kW)
  - Total duration: t = 3409.75 s
  - % of total operating time in power overload: 0.44 %
  - Number of times reached: 101
  - Duration < 10 s: 63 times
  - Duration 10.1 < t < 30 s: 12 times
  - Duration > 30.1 s: 26 times
  - Maximum power reached: 46.83 kW

- Overload in Torque (T > 200 Nm)
  - Number of times reached: 0
  - Maximum torque reached: 200 Nm

- Overtemperature (T > 70 ^{o}C)
  - Number of times reached: 1, during 314 s
  - Maximum temperature reached: 73.10 ^{o}C

6.3.4.2.3 POWER QUALITY

Figure 49 and Figure 50 present indicators of power quality when using CL5, in terms of standard deviation and peak to average power for both output electric power in the generator and electric power sent to the grid.

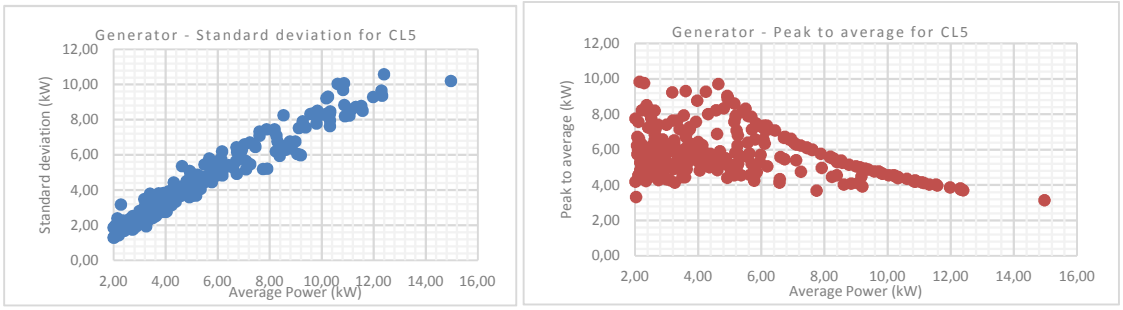

FIGURE 49. STANDARD DEVIATION AND PEAK TO AVERAGE OF GENERATOR POWER IN FUNCTION OF AVERAGE POWER FOR CL5

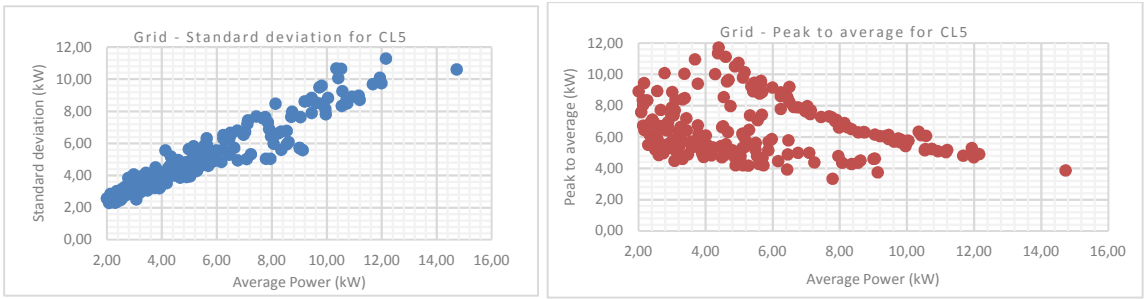

FIGURE 50. STANDARD DEVIATION AND PEAK TO AVERAGE OF GRID POWER IN FUNCTION OF AVERAGE POWER FOR CL5

6.3.5 CONTROL LAW CL6.0

6.3.5.1 IMPLEMENTATION

The implementation of this control law is quite straightforward as the code is directly implemented on the PLC and almost as simple as CL1. Figure 51 shows the behaviour of CL6.0 with the main operational quantities. It is quite similar to CL5, a rotational speed control based on a torque law and allowing short-term peaks of power higher than the generator rated capacity.

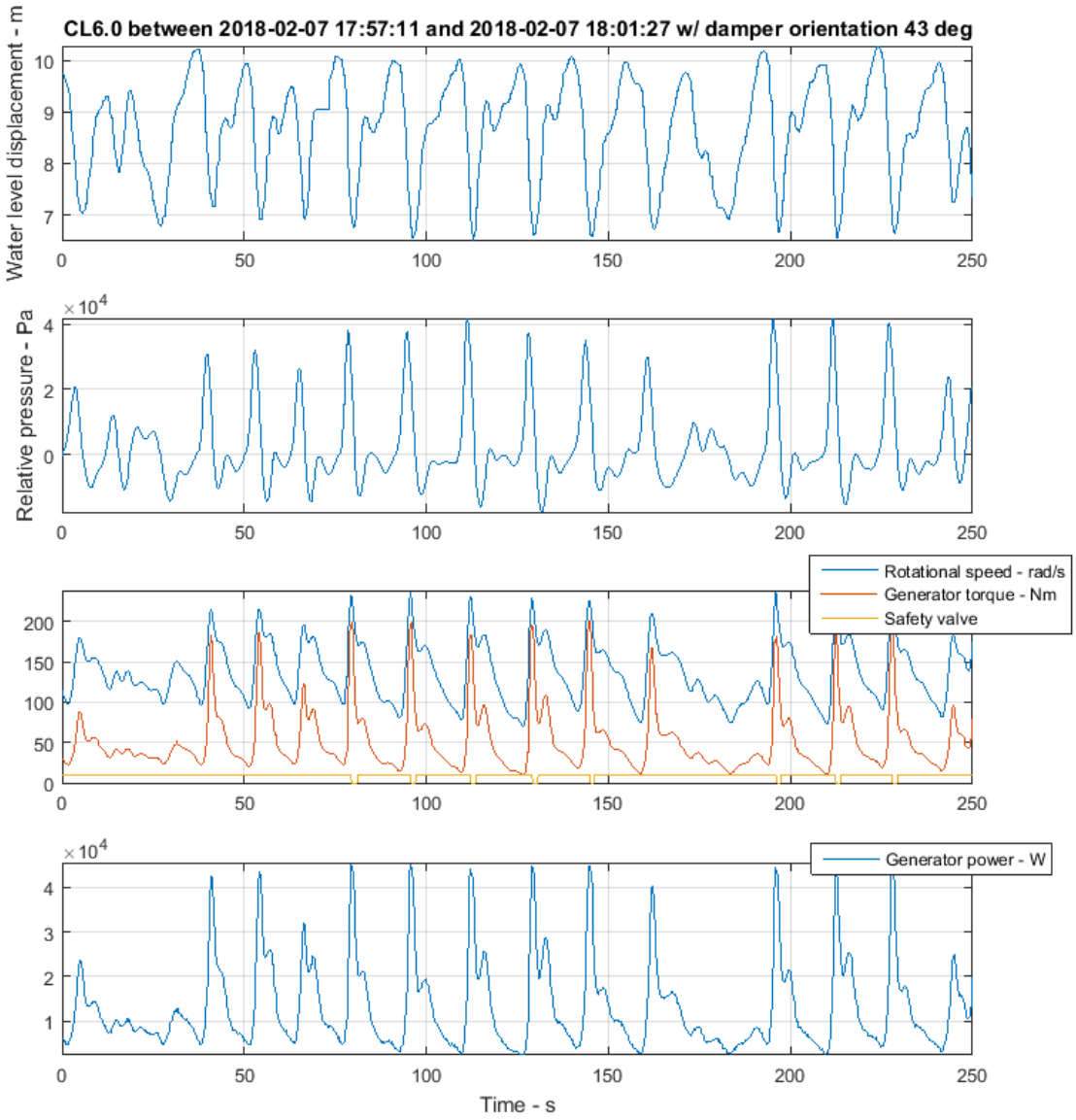

FIGURE 51. CL6.0 OPERATION DURING A SEA STATE $H_s = 2.90\ m$ AND $T_e = 14.30s$

6.3.5.2 OPERATION RESULTS

6.3.5.2.1 PERFORMANCE

Figure 52 shows globally the performance of CL6 rounds the one of CL1. The total weighted average production is slightly improved by 5%. Good score is obtained with low energy periods sea states or for waves higher than 3m. In the most frequent sea states, SS2 10 11 12, CL6 performs quite alike CL1. It is only during SS19 that this control law overtakes CL1. Also, it seems there is less dispersion inside a sea state which strengthened the confidence on its performance. In the majority of the sea states, the higher quartile stays around 1.5.

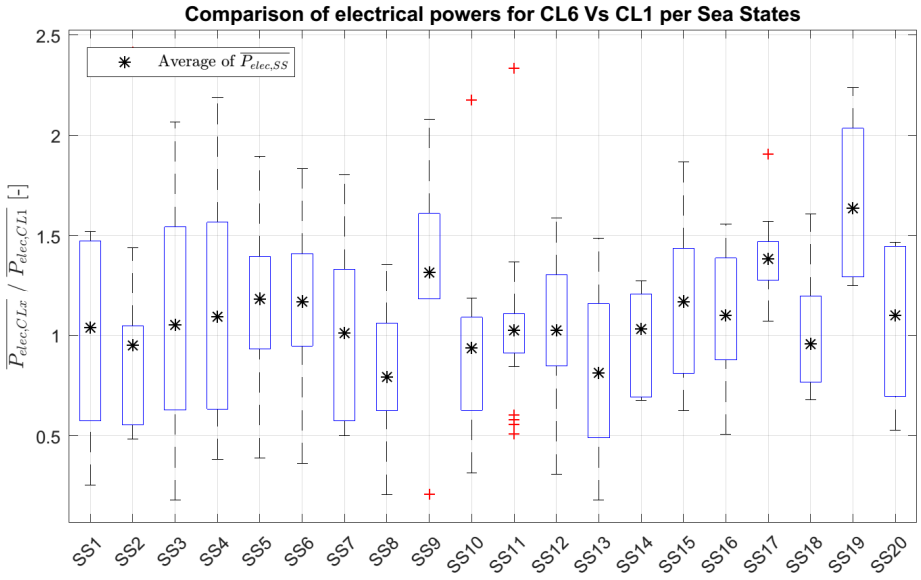

FIGURE 52. ELECTRICAL PRODUCTION OF CL6.0 COMPARED TO CL1

6.3.5.2.2 RELIABILITY

The analysis has been performed along 507 tests of 30 min each one, resulting in a total of 15,210 min in operation. Among these tests, the following extremal operation has been reached:

- Overspeed (Ω > 230 rad/s):
  - Total duration: t = 468.25 s
  - % of total operating time in overspeed: 0.051 %
  - Number of times reached: 76
  - Duration < 10 s: 57 times
  - Duration 10.1 < t < 30 s: 17 times
  - Duration > 30.1 s: 2 times
  - Maximum speed reached: 264.93 rad/s

- Overload in Power (P > 30 kW)
  - Total duration: t = 6338.50 s
  - % of total operating time in power overload: 0.69 %
  - Number of times reached: 199
  - Duration < 10 s: 84 times
  - Duration 10.1 < t < 30 s: 51 times
  - Duration > 30.1 s: 64 times
  - Maximum power reached: 47.1 kW
- Overload in Torque (T > 200 Nm)
  - Number of times reached: 0
  - Maximum torque reached: 200 Nm

- Overtemperature (T > 70 ^{o}C)
  - Number of times reached: 0
  - Maximum temperature reached: 68.10 ^{o}C

6.3.5.2.3 POWER QUALITY

Figure 53 and Figure 54 present indicators of power quality when using CL6.0, in terms of standard deviation and peak to average power for both output electric power in the generator and electric power sent to the grid.

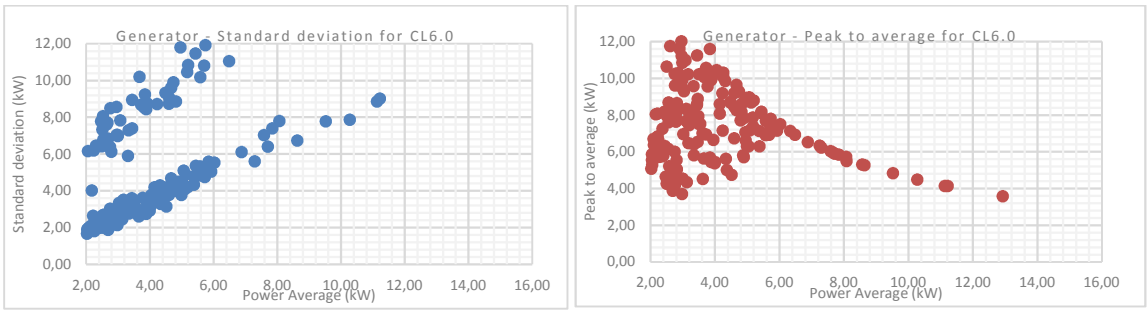

FIGURE 53. STANDARD DEVIATION AND PEAK TO AVERAGE OF GENERATOR POWER IN FUNCTION OF AVERAGE POWER FOR CL6.0

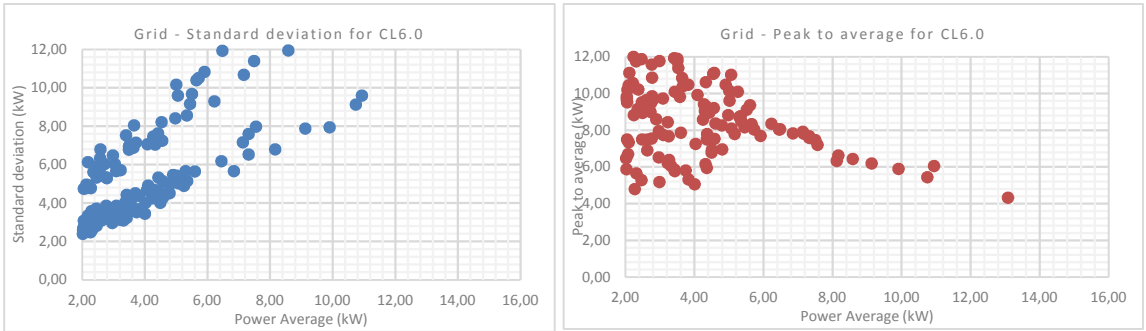

FIGURE 54. STANDARD DEVIATION AND PEAK TO AVERAGE OF GRID POWER IN FUNCTION OF AVERAGE POWER FOR CL6.0

6.4 ASSESSMENT OF CL4 IN RESPECT TO THE SIMAR POINT

During the testing period of CL4, none of the local wave measurement sensors was available. In this specific case, the SIMAR point in front of Mutriku is used to detail the wave climate. An attempt to try to correlate SS from this source and with the RBR data. If the two sources match CL4 can be integrated into the analysis with the other CL. Figure 55 shows the H_s or T_p from these two sources and it seems obvious that no correlation can be made. The SIMAR point is then the reference for the comparison of CL4 with CL1. Note that in this case, the wave period employed is the peak period T_p whereas in the other cases it is the energy period T_e. Also in this case due to the relatively low number of sea states, the IEC standard for sea state partition is used.

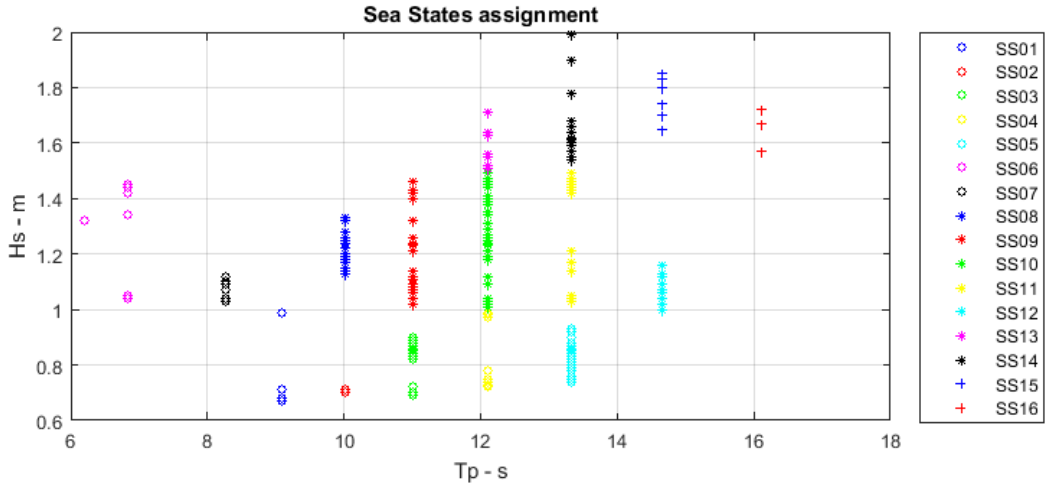

FIGURE 55. SEA STATE DIVISION OF CL4

And here goes the table of sea states experienced during the tests of CL4. There is a good variety of wave conditions but some sea states are not well represented: 4 sea states gather less than 10 tests including both CL1 and CL4.

TABLE 15. SEA STATES DURING THE TEST OF CL4

SS	Hs (m)	Te (s)	N. of element	Occurrence (%)
1	0.5	9	4	1.48
2	0.5	10	12	4.44
3	0.5	11	25	9.26
4	0.5	12	16	5.93
5	0.5	13	22	8.15
6	1	6	13	4.81
7	1	8	6	2.22
8	1	10	18	6.67
9	1	11	26	9.63
10	1	12	47	17.41
11	1	13	28	10.37

12	1	14	10	3.70
13	1.5	12	11	4.07
14	1.5	13	21	7.78
15	1.5	14	7	2.59
16	1.5	16	4	1.48
TOTAL NUMBER OF TESTS			**270**	**100.00**

6.4.1 IMPLEMENTATION

Figure 56 presents a time series of the same quantities as before to understand the behaviour of the control algorithm. This is after CL3 the second time a latching control strategy is used in this wave power plant. The latching valve operation is plotted in the 3rd graphic.

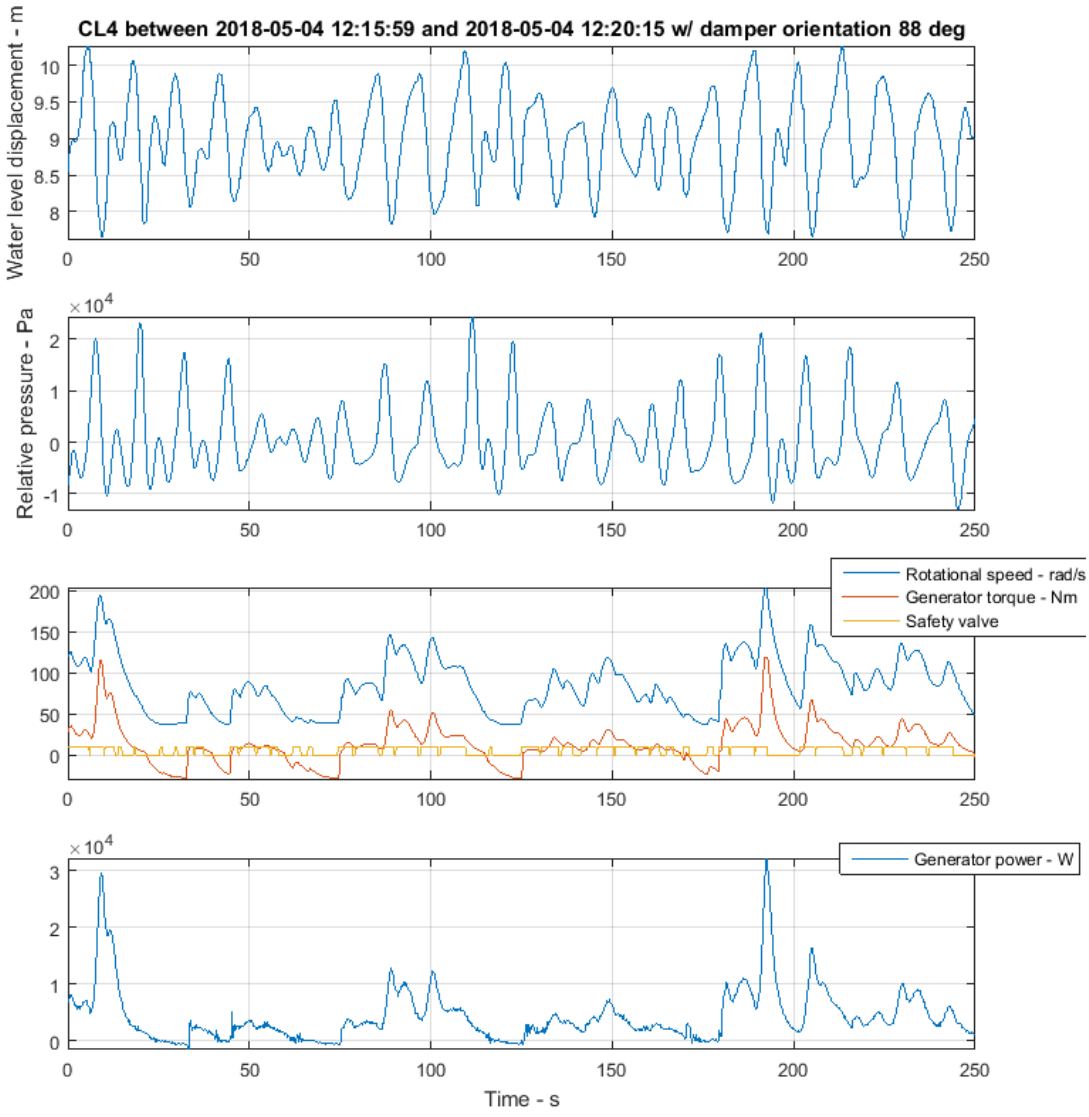

FIGURE 56. CL4 OPERATION DURING A SEA STATE $H_s = 1.20m$ AND $T_e = 13s$

It is more convenient to observe the latching valve operation in Figure 57 following the red line. The valve operates each time the dimensionless pressure, in blue, reaches the defined thresholds (straight lines).

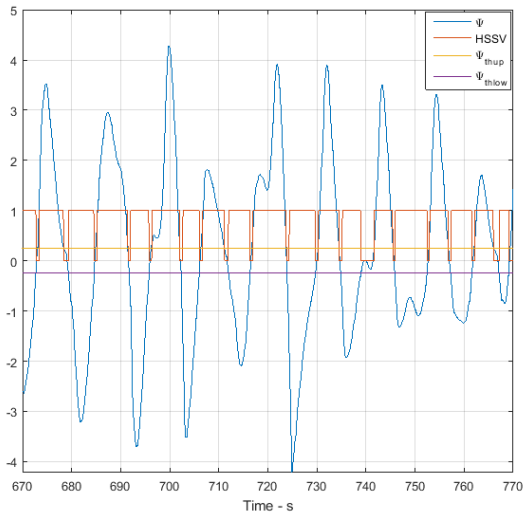

FIGURE 57. LATCHING VALVE OPERATION DURING CL4

This control strategy was implemented in an external computer following the configuration described in Section 6.1. During the tests, several pressure thresholds were tested, but their effect is not analysed here.

6.4.2 OPERATION RESULTS

6.4.2.1 PERFORMANCE

Following the same methodology as in previous section, the electrical production of CL1 is first analysed and is used as the base case scenario for comparison.

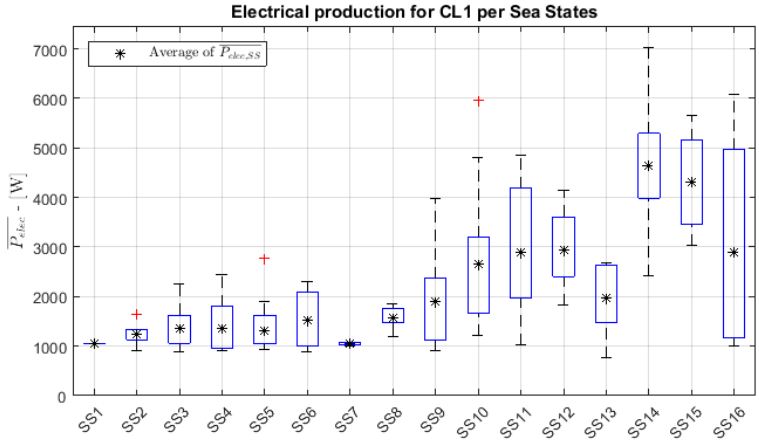

FIGURE 58. ELECTRICAL PRODUCTION FOR CL1 PER SEA STATE

In the following figure, the performance of CL4 is presented normalised with the production of CL1. It must be highlighted that SS5 and SS16 are away from the analysis as there is only one CL4 test during each of these SS. In the analysis of this latching control based on pressure threshold produces globally 15% less than CL1. Including SS5 and 16, there is an improvement of 2% in respect to CL1. Due to the lack of tests for this CL, there is too much uncertainty and the study can be biased. Also, as it has been said in the D4.1 [10] and when analyzing CL3 results, a latching control on the MWPP was expected to provide poor performance whereas it can be promising to operate it in a floating OWC [20], [21], [11], [13], [12], [16]. This CL should be included in the test campaign at BiMEP.

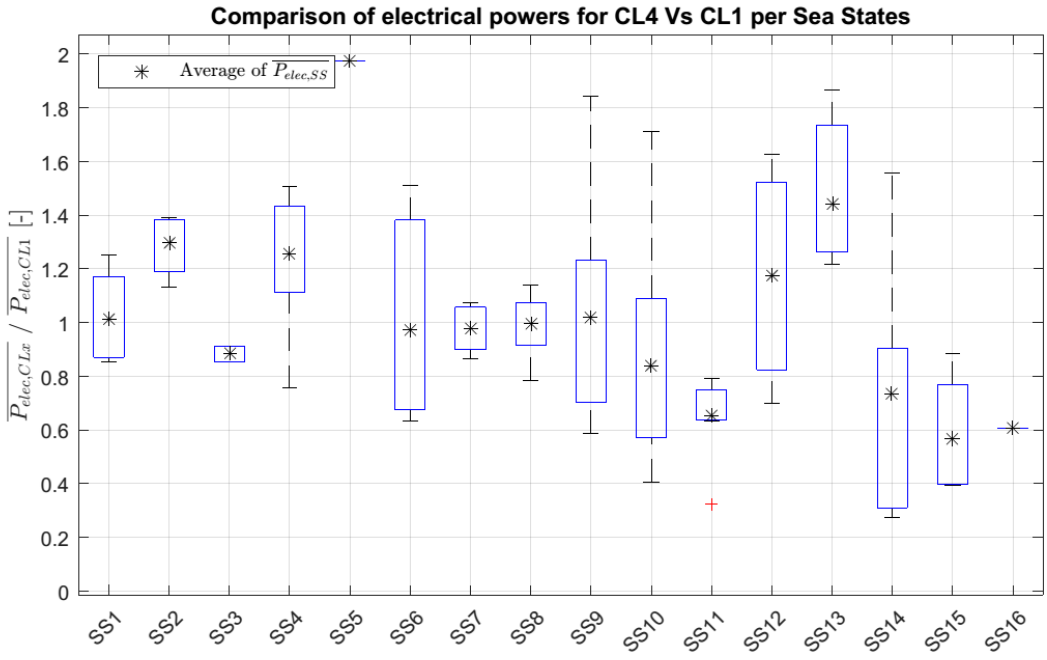

FIGURE 59. ELECTRICAL PRODUCTION OF CL4 COMPARED TO CL1

6.4.2.2 RELIABILITY

The analysis has been performed along 155 tests of 30 min each one, resulting in a total of 4650 min in operation. Among these tests, the following extremal operation has been reached:

- Overspeed (w > 230 rad/s):
  - Total duration: t = 17,5 s
  - % of total operating time in overspeed: 0.006%
  - Number of times reached: 5
  - Duration < 10 s: 4 times
  - Duration 10,1 < t < 30 s: 1 times
  - Duration > 30.1 s: 0 times
  - Maximum speed reached: 249.02 rad/s

- Overload in Power (P > 30 kW)
  - Total duration: t = 25.25 s
  - % of total operating time in power overload: 0.009%
  - Number of times reached: 18
  - Duration < 10 s: 18 times
  - Duration 10.1 < t < 30 s: 0 times
  - Duration > 30.1 s: 0 times
  - Maximum power reached: 41.5 kW

- Overload in Torque (T > 200 Nm)
  - Number of times reached: 0
  - Maximum torque reached: 179.28 Nm

- Overtemperature (T > 70 ^{o}C)
  - Number of times reached: 0
  - Maximum temperature reached: 57.50 ^{o}C

6.4.2.3 POWER QUALITY

Figure 60 and Figure 61 present indicators of power quality when using CL4, in terms of standard deviation and peak to average power for both output electric power in the generator and electric power sent to the grid.

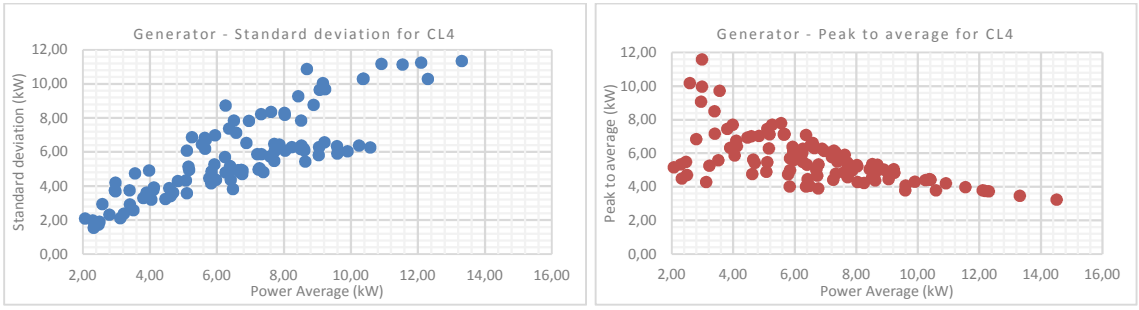

FIGURE 60. STANDARD DEVIATION AND PEAK TO AVERAGE OF GENERATOR POWER IN FUNCTION OF AVERAGE POWER FOR CL4

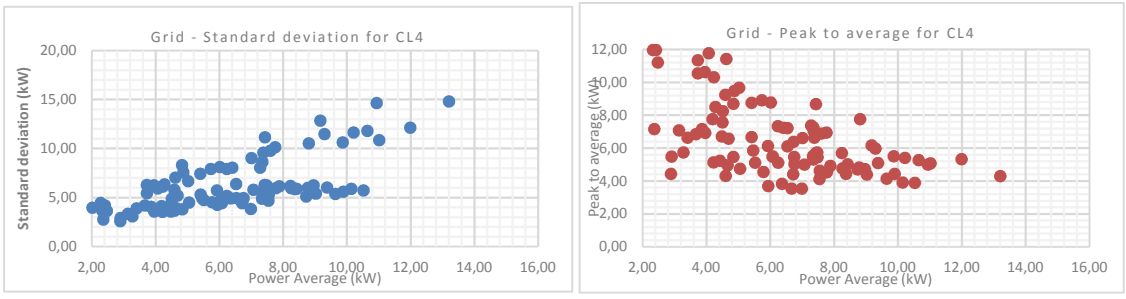

FIGURE 61. STANDARD DEVIATION AND PEAK TO AVERAGE OF GRID POWER IN FUNCTION OF AVERAGE POWER FOR CL4

6.5 ASSESSMENT OF CL6.1 COVERING THE DEPLOYMENT OF THE ISURKI

First of all, the wave climate measured by the ISURKI pressure sensor experienced during the operation of CL6.1 is grouped in 8 sea states. This time, the number of sea states is reasonable enough to use the IEC standard sea state division. During the 2-week test of CL6.1, only CL1 was also operational to serve as the base for comparison. Unfortunately, during June, the resource was quite stable and no sea state above 1m was observed. Still there were 67 1/2h tests of CL1 and 157 for CL6.1.

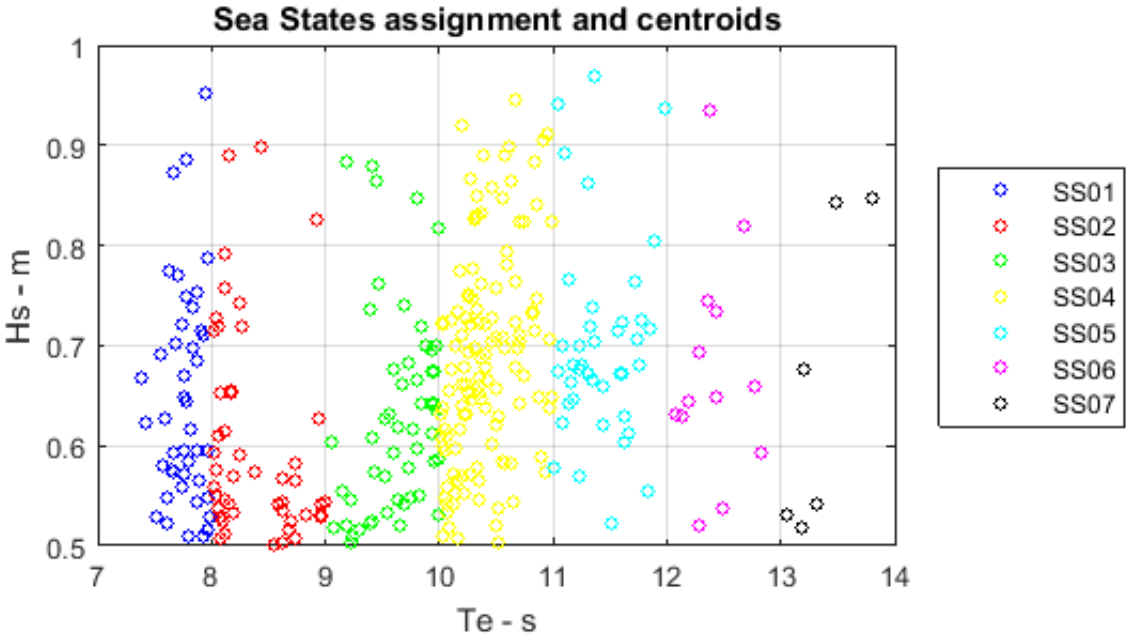

FIGURE 62. SEA STATE DIVISION OF CL6.1

Table 16 details the sea state observed during the test of this control law:

TABLE 16. SEA STATES DURING THE TEST OF CL6.1

SS	Hs (m)	Te (s)	N. of element	Occurrence (%)
1	0.5	7	44	13.54
2	0.5	8	48	14.77
3	0.5	9	52	16.00
4	0.5	10	122	37.54
5	0.5	11	40	12.31
6	0.5	12	13	4.00
7	0.5	13	6	1.00
TOTAL NUMBER OF TESTS			**325**	**100.00**

6.5.1 IMPLEMENTATION

This predictive control strategy is one of the few known ones implemented in a real environment. The prediction feature is made possible by the presence of the real-time wave measurement sensor ISURKI. The optimisation of the control parameters is made running the numerical plant model with the measured wave elevation along the travel time of the wave from the time it passes in front of the sensor until it reaches the plant wall. This gives a satisfactory prediction time to compute average values of production powers. This control algorithm is not very sensitive to synchronisation between the wave measured up-wave and the one hitting the plant because the cost function is based on average values. Figure 63 presents some operational values collected during a test of CL6.1. The behaviour is quite similar to the other turbine speed control laws like CL1, CL5 or CL6.0.

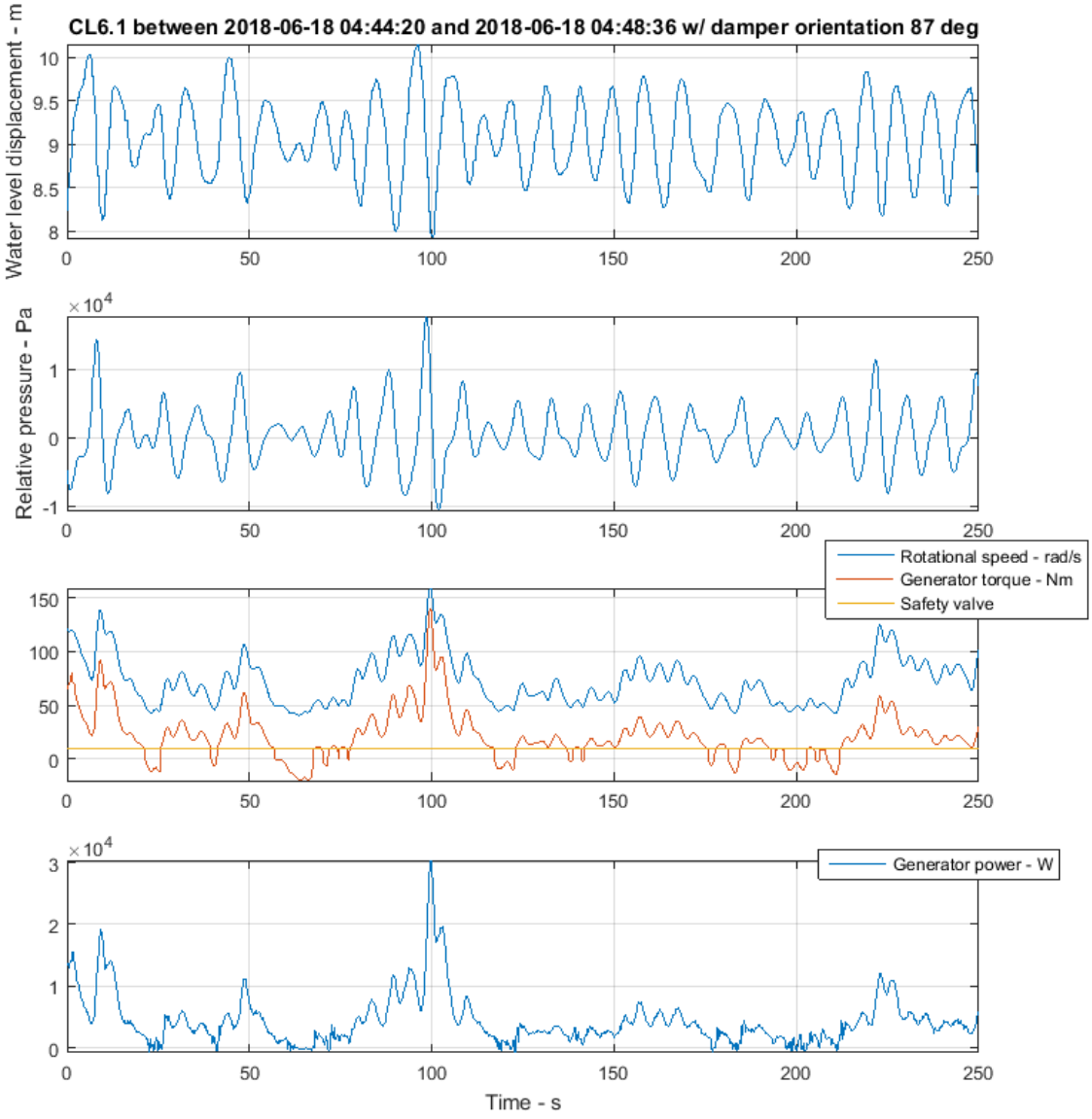

FIGURE 63. CL6.1 OPERATION DURING A SEA STATE $H_s = 0.73\ m$ AND $T_e = 11.43s$

The originality of this control law against the others is presented in the figures below. Figure 64 shows the evolution of the control parameters $[a, b]$ from the beginning of a test and the convergence towards final optimised values. The strength of this CL is that it can adapt the torque law to control the turbine speed in real-time and in function of the incoming waves unless CL1. Plus, it adapts even if the sea states change because there is no learning or weighting of best parameters as in CL5.

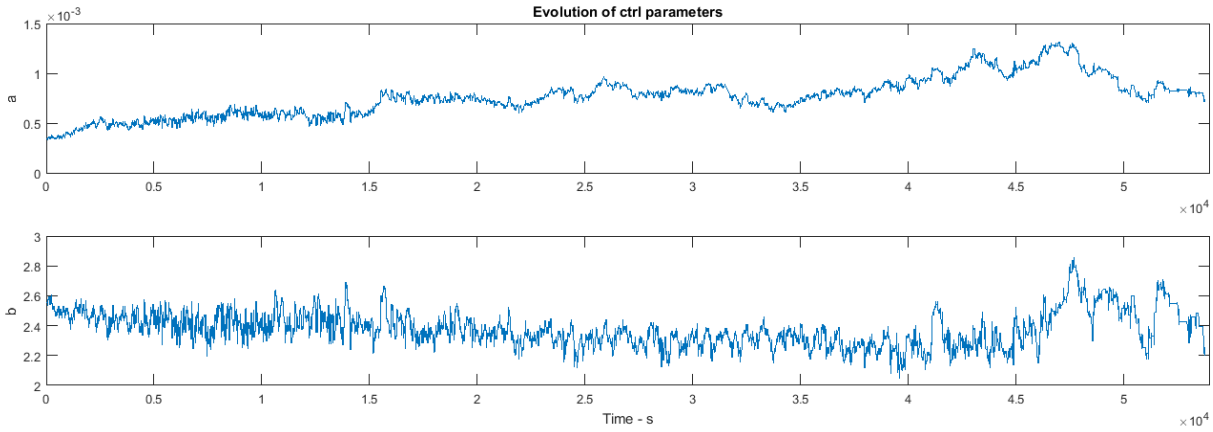

FIGURE 64. CL6.1 OPERATION DURING A SEA STATE $H_s = 0.73\ m$ AND $T_e = 11.43s$

However, the principal drawback of this algorithm is that optimal parameters can only be optimal if the model represents the real plant with high fidelity. Next graph shows a fast Fourier transform of the main quantities in the model state vector that is: the heave velocity and position, and the relative pressure. The spectral shape permits to look at the magnitudes in function of the frequencies without being disturbed by data synchronisation. In all quantities, the frequencies are kept for both the model and the measurement, but the numerical model shows magnitudes lower than expected. The hydrodynamic model was adapted from the one used in Task 4.2. But still, this one needs to be fully validated. This means there is still room for improvement for this predictive algorithm.

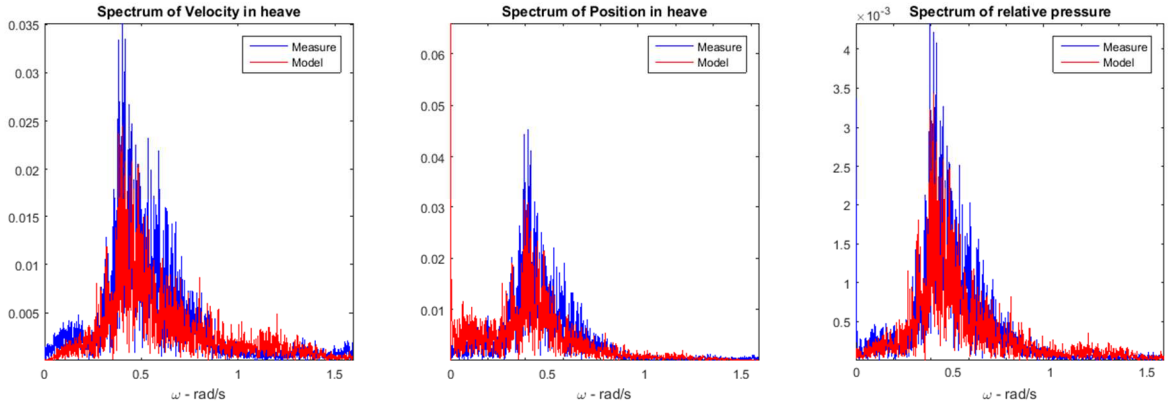

FIGURE 65. CL6.1 OPERATION DURING A SEA STATE $H_s = 0.73\ m$ AND $T_e = 11.43s$

6.5.2 OPERATION RESULTS

6.5.2.1 PERFORMANCE

Following the same methodology for the testing period of the predictive control CL6.1, a graphic of the production from CL1 is presented. Note that the average of the mean electrical powers represented by the marker - * - are taken for all the tests of a sea state. This is why in some cases, the average can be misaligned in the box of the lower and higher quartiles, like SS4, or even outside as in SS8. In brief, the box does not consider the outliers (red cross) whereas does the average.

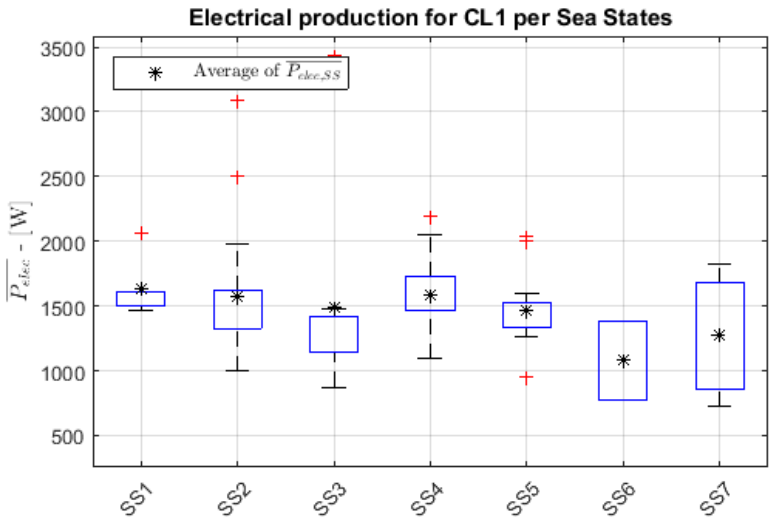

FIGURE 66. ELECTRICAL PRODUCTION FOR CL1 PER SEA STATE

When comparing the CL6.1 with CL1, one shall keep in mind that, due to the late installation of the Isurki sensor, this controller could only be tested in a short period of time and with a limited number of sea states. Still, there is a relevant number of data to perform a statistical analysis. Globally, in all the sea states, the power production by CL6.1 is improved by 15% to 45% in relevant sea states (from SS1 to SS5). The weighted average along all the SS states an increase of 31%. In most of the cases, the lower quartile equals the average production of CL1. This means that the power production of CL6.1 is at least the same as CL1 in the worst cases.

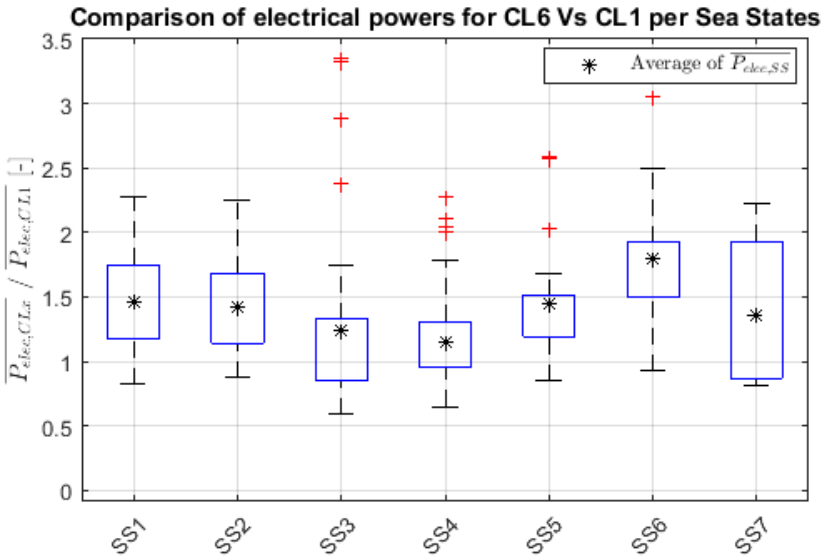

FIGURE 67. ELECTRICAL PRODUCTION OF CL6.1 COMPARED TO CL1

Although there is a limited number of test available, this predictive controller seems promising and should be tested in the Marmok A5 for a longer period.

6.5.2.2 RELIABILITY

The analysis has been performed along 380 tests of 30 min each one, resulting in a total of 11,400 min in operation. Among these tests, the following extremal operation has been reached:

- Overspeed (w > 230 rad/s):
  - Total duration: t = 0.75 s
  - % of total operating time in overspeed: 0.0 %
  - Number of times reached: 2
  - Duration < 10 s: 2 times
  - Duration 10.1 < t < 30 s: 0 times
  - Duration > 30.1 s: 0 times
  - Maximum speed reached: 232.35 rad/s

- Overload in Power (P > 30 kW)
  - Total duration: t = 30.25 s
  - % of total operating time in power overload: 0.004 %
  - Number of times reached: 9
  - Duration < 10 s: 9 times
  - Duration 10.1 < t < 30 s: 0 times
  - Duration > 30.1 s: 0 times
  - Maximum power reached: 37.11 kW

- Overload in Torque (T > 200 Nm)
  - Number of times reached: 0
  - Maximum torque reached: 200 Nm

- Overtemperature (T > 70 ºC)
  - Number of times reached: 0
  - Maximum temperature reached: 58.09 ºC

6.5.2.3 POWER QUALITY

Figure 68 and Figure 69 present indicators of power quality when using CL6.1, in terms of standard deviation and peak to average power for both output electric power in the generator and electric power sent to the grid.

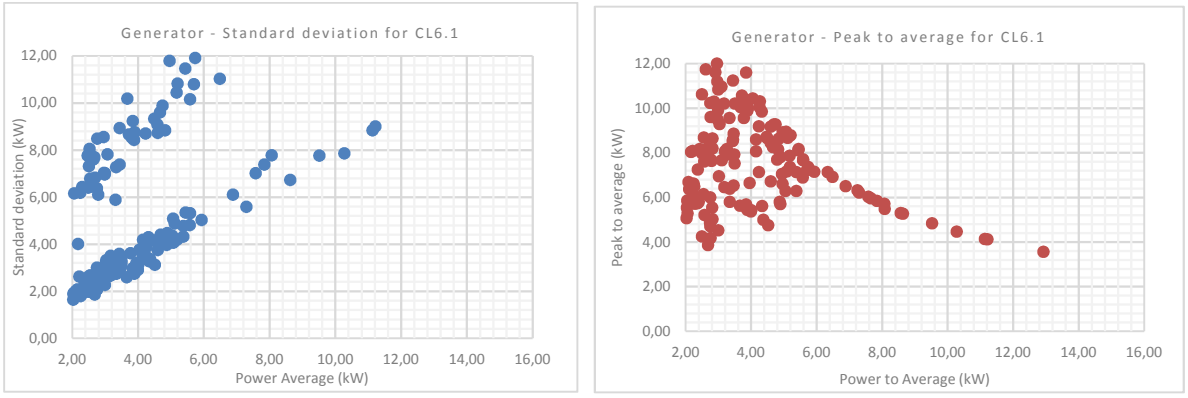

FIGURE 68. STANDARD DEVIATION AND PEAK TO AVERAGE OF GENERATOR POWER IN FUNCTION OF AVERAGE POWER FOR CL6.1

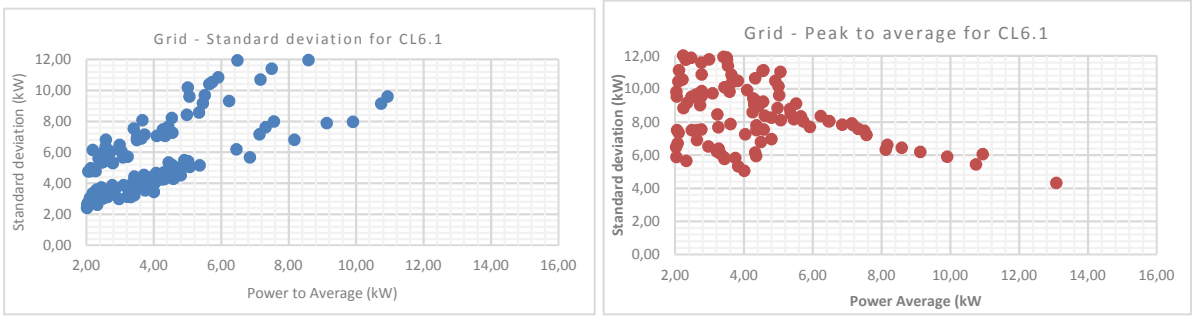

FIGURE 69. STANDARD DEVIATION AND PEAK TO AVERAGE OF GRID POWER IN FUNCTION OF AVERAGE POWER FOR CL6.1

6.6 ASSESSMENT OF CL7

6.6.1 IMPLEMENTATION

The optimal latching control based on the DG finite element method requires an accurate estimation of the incoming waves to compute the excitation force that acts on the OWC. As proved in Annex I, the pressure sensor installed at sea-bottom is not able to predict the amplitude of each wave component, and the direction of the wave crest. Without this information, it is not possible to estimate the excitation force. As such, the control CL7 could not be implemented and tested at the Mutriku power plant.

6.7 COMPARISON BETWEEN CLS

This section focuses on the comparison of the control laws regarding the criteria discussed previously. It summarises the results presented earlier, proposes a performance assessment focusing on the PTO efficiency and concludes on a global evaluation for each CL upon several criteria.

6.7.1 PERFORMANCE

6.7.1.1 POWER PRODUCTION

The following section summarises all the Performance subsection of each CL. This offers a performance comparison for all the CL in respect to CL1, for all the sea conditions and during the three periods analysed. The weighted total average symbolises the average difference of a CL electrical power production taking into account the occurrence of each sea state.

TABLE 17. POWER PRODUCTION COMPARISON OF THE CLS WITH CL1 DURING TEST PERIOD #1

SS	CL2	CL3	CL5	CL6.0
1	1.63	0.89	1.19	1.04
2	1.16	0.56	0.99	0.95
3	1.23	0.93	1.13	1.05
4	1.32	0.74	1.38	1.09
5	1.18	0.61	1.15	1.18
6	1.22	0.62	1.00	1.17
7	1.65	0.91	1.65	1.01
8	1.09	0.57	0.90	0.79
9	1.11	0.74	1.02	1.32
10	1.24	0.53	0.92	0.94
11	1.07	0.52	1.03	1.03
12	1.13	0.57	1.06	1.02
13	1.18	0.45	1.11	0.81
14	1.04	0.83	1.13	1.03
15	1.30	0.67	1.28	1.17
16	1.31	0.51	1.03	1.10
17	1.26	0.58	1.27	1.38

18	1.06	0.38	0.98	0.96
19	1.71	0.33	1.43	1.64
20	1.27	0.59	1.15	1.95
Weighted total avg	**1.22**	**0.63**	**1.10**	**1.05**

TABLE 18. POWER PRODUCTION COMPARISON OF CL4 WITH CL1 DURING TEST PERIOD #2

SS	CL4
1	1.01
2	1.30
3	0.88
4	1.25
5	1.98
6	0.97
7	0.98
8	1.00
9	1.02
10	0.84
11	0.65
12	1.18
13	1.44
14	0.73
15	0.56
16	0.61
Weighted total avg	**0.85**

TABLE 19. POWER PRODUCTION COMPARISON OF CL6.1 WITH CL1 DURING TEST PERIOD #3

SS	CL6.1
1	1.46
2	1.42
3	1.25
4	1.15
5	1.45
6	1.79
7	1.36
Weighted total avg	**1.31**

Analysing the performance of the controllers focusing on the power production, CL6.1, though operational in fewer sea states, obtains the highest improvement producing 31% more than the base case. Then CL2 follows with 22%, CL5 completes the podium with 10% of global increase. As expected, the two latching strategies are not performing well but CL4 appears to be more convincing than CL3 for future tests.

6.7.1.2 PTO EFFICIENCY

This section is divided into two subsections corresponding to the first and second phase of the test campaign, that are before and after the generator recommissioning. The motivation to

present the results that way is because the analysis requires the same testing conditions in the plant. Here are the main differences between the two phases:

- The electrical setup is different in Phase II: installation of the electrical filter, change in the low-level current control in the power electronics.
- Few control laws were operational in Phase I: CL1, CL2 and CL5 were in test during Phase I and CL2 was not implemented correctly while CL5 was being tuned.
- Not all data for a complete efficiency analysis were available: the generator electrical quantities were calibrated during Phase II after apprehending the inaccuracy of the power electronics estimation. It is likely that in Phase I uncertainties exists due to this issue. Thus, the electrical part is excluded from the analysis of the PTO efficiency for Phase I.
-

The turbine efficiency is computed as the ratio of the turbine power $\bar{P}_{turb}$ average of one ½ h test and the average pneumatic power $\bar{P}_{pneu}$ available to the turbine during the same period:

$$\eta_{turb} = \frac{\bar{P}_{turb}}{\bar{P}_{pneu}} \quad (40)$$

The pneumatic and turbine powers are computed with eq.1 to 5 the same way as explained in [9]. They are based on two real measurements (relative pressure inside the chamber and turbine rotational speed) which were filtered with a zero-phase low pass filter. The pressure used is the '*Pressure Sensor 2'* as mentioned in Table 7, a drift on the sensor was detected and corrected with the assumptions that the average of the internal pressure measured by the other sensors must be null when the valve is closed (c.f. Deliverable D3.3 [9]). The turbine characteristic curves obtained from the dry tests Figure 4 were used to determine the dimensionless coefficients $\Psi, \Phi \text{ and } \Pi$ to finally compute the instantaneous $P_{pneu} \text{ and } P_{turb}$. The same way the generator efficiency is the following:

$$\eta_{gen} = \frac{\bar{P}_{gen}}{\bar{P}_{turb}} \quad (41)$$

where $\bar{P}_{gen}$ is the 1/2h-average power estimated by the power electronics and corrected with the methodology detailed in Section 4.2. In this formulation, the generator efficiency includes the filter efficiency.
Finally, the total efficiency includes the turbine, generator and filter losses and is:

$$\eta_{tot} = \eta_{turb}\,\eta_{gen} \quad (42)$$

6.7.1.2.1 PTO EFFICIENCY IN PHASE I

Only the turbine efficiency is available in Phase I. The generator is not considered because high uncertainties reside in the estimation of the electrical power by the power electronics. Figure 70 shows the turbine efficiency of CL1 and CL5. Although operative during this phase, CL2 was not implemented correctly and is not considered in the analysis.

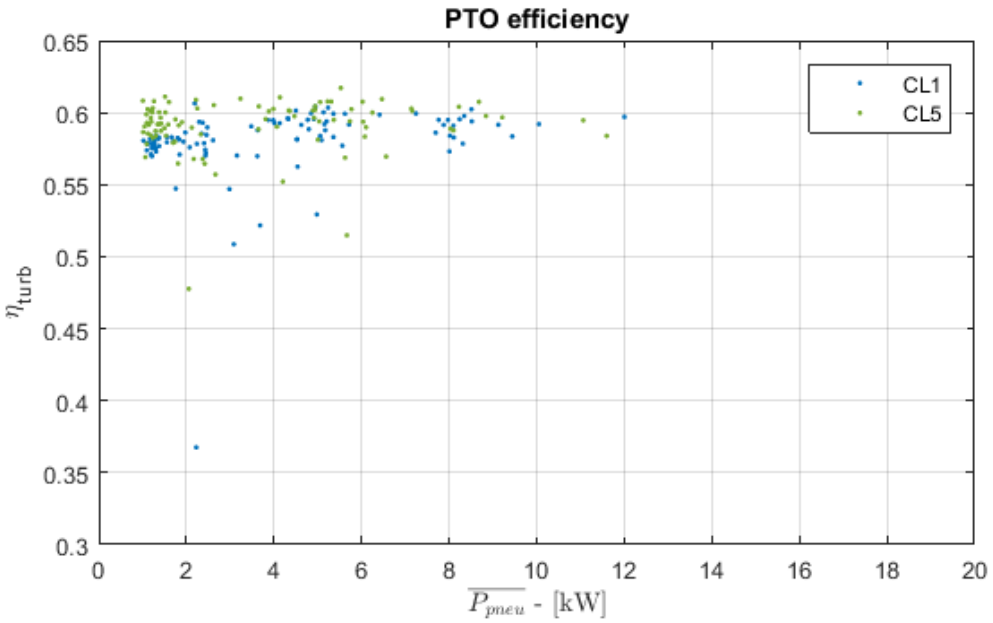

FIGURE 70. TURBINE EFFICIENCY DURING PHASE I

Efficiencies between 55-62% were obtained using these controllers where CL5 appears more efficient than CL1. These are the highest values of turbine efficiency obtained during all the PTO deployment. Figure 71 presents results of CL1 operating during the two phases. With the same power available at the turbine inlet, an efficient drop of 10% is observed.

Figure 72 and Figure 73 show histograms of the probability of occurrence of pressure coefficients, $p_o(\Psi)$, for representative CL1 and CL5 test-cases measured during the first and the second campaigns. Also represented in the same figures are the Biradial turbine instantaneous efficiency, η_{turb}, versus the pressure head coefficient, Ψ, and the pressure coefficient for the best efficiency point, Ψ_{bep}. The testing conditions are also presented in the figures. Note that a higher probability at Ψ_{bep} corresponds to higher turbine mean efficiency. Consequently, a less dispersive probability density function around Ψbep corresponds to higher mean efficiencies.

Comparing the results shown in the figures for similar available pneumatic power, it is evident that results obtained in the first campaign, either for CL1 or CL5, show a much less dispersive probability density function around Ψ_{bep} corresponding to higher mean efficiencies, in comparison with the results measured in the second campaign. This clearly shows that the turbine aerodynamic performance is the same in both campaigns and that the drop in the turbine time-averageg efficiency measured during the second campaign is due to poor selection of the CL1 and CL5 control parameters for the tests performed during the second campaign.

To corroborate the above analysis, histograms of the probability of occurrence of pressure coefficients, $p_o(\Psi)$ are shown in Figure 74 to Figure 76, for representative test-cases measured during the second campaign, with different control laws. Results in Figure 74 to Figure 76 confirm that the control laws producing higher turbine average efficiencies show less dispersive probability density functions around Ψ_{bep}.

Consequently, the reader is asked to carefully read the following results knowing that higher efficiencies are to be expected with this PTO and that the objective of this work package is the comparison and assessment of the control laws.

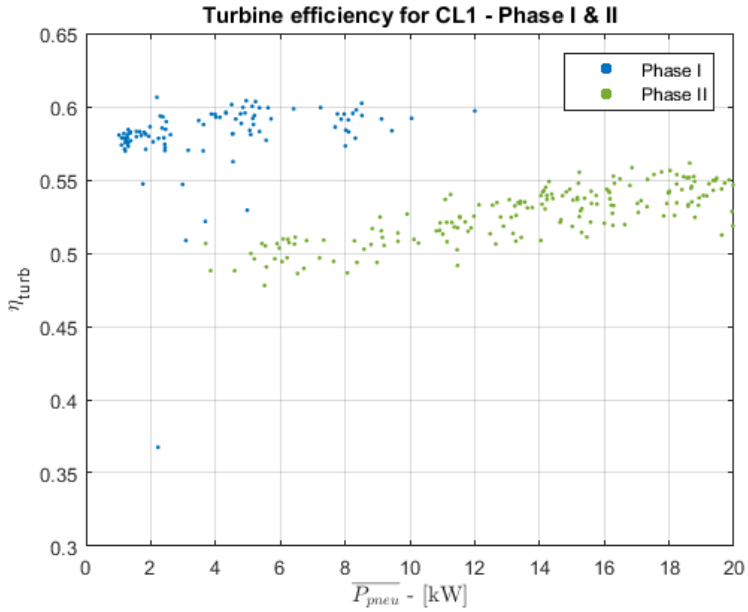

FIGURE 71. COMPARISON OF CL1 DURING PHASE I AND II

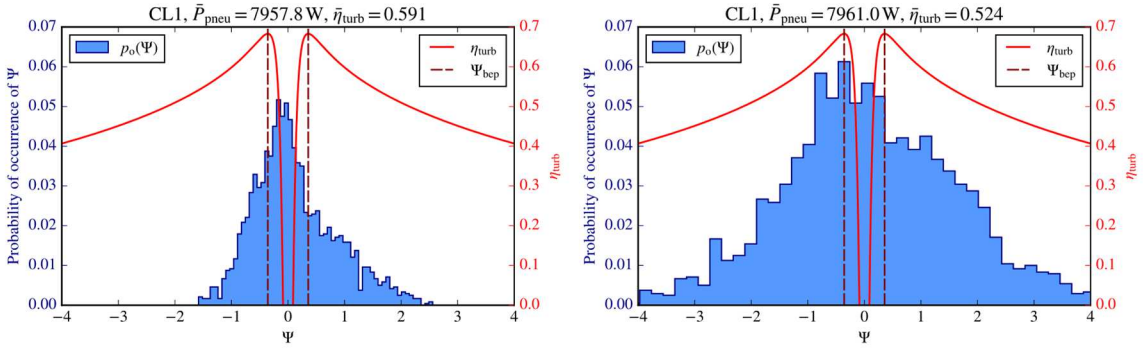

FIGURE 72 - PROBABILITY OF OCCURRENCE OF THE DIMENSIONLESS PRESSURE HEAD Ψ FOR CL1. COMPARISON BETWEEN A TEST PERFORMED IN FIRST CAMPAIGN (LEFT) WITH A TEST OF THE SECOND CAMPAIGN (RIGHT).

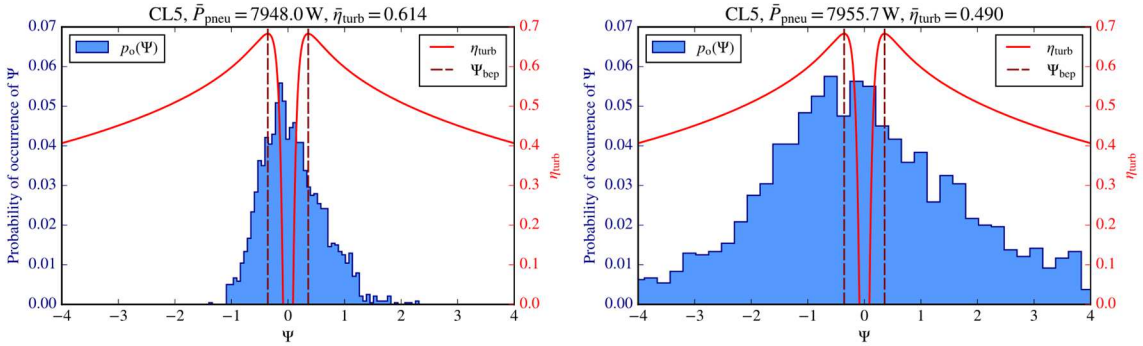

FIGURE 73 - PROBABILITY OF OCCURRENCE OF THE DIMENSIONLESS PRESSURE HEAD Ψ FOR CL5. COMPARISON BETWEEN A TEST PERFORMED IN FIRST CAMPAIGN (LEFT) WITH A TEST OF THE SECOND CAMPAIGN (RIGHT).

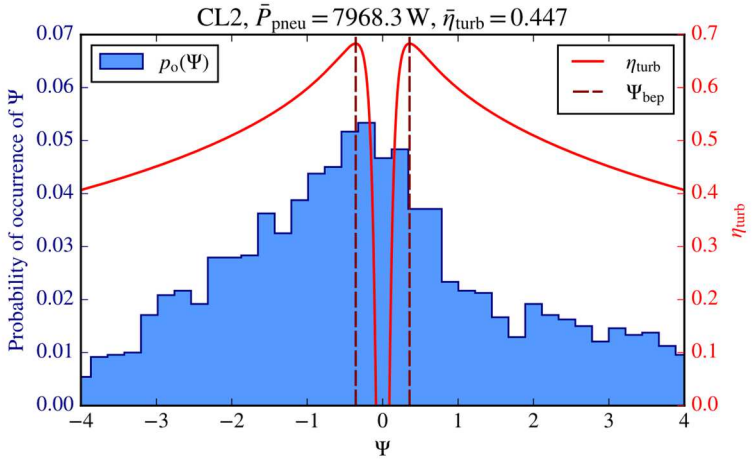

FIGURE 74 - PROBABILITY OF OCCURRENCE OF THE DIMENSIONLESS PRESSURE HEAD Ψ CONCERNING A TEST OF CL2 PERFORMED IN THE SECOND CAMPAIGN.

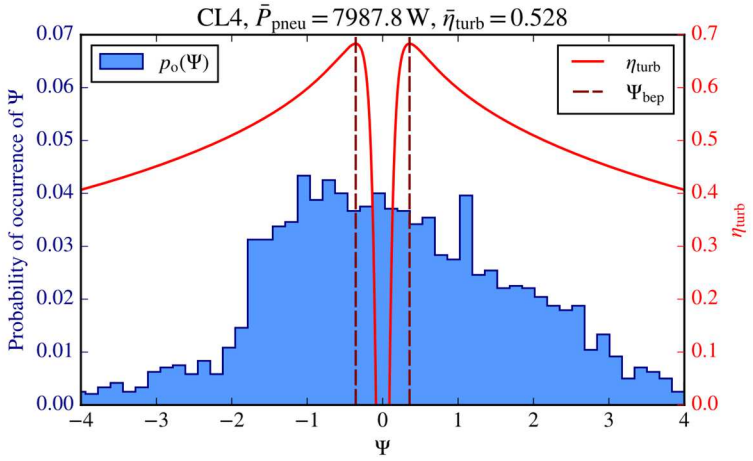

FIGURE 75 - PROBABILITY OF OCCURRENCE OF THE DIMENSIONLESS PRESSURE HEAD Ψ CONCERNING A TEST OF CL4 PERFORMED IN THE SECOND CAMPAIGN.

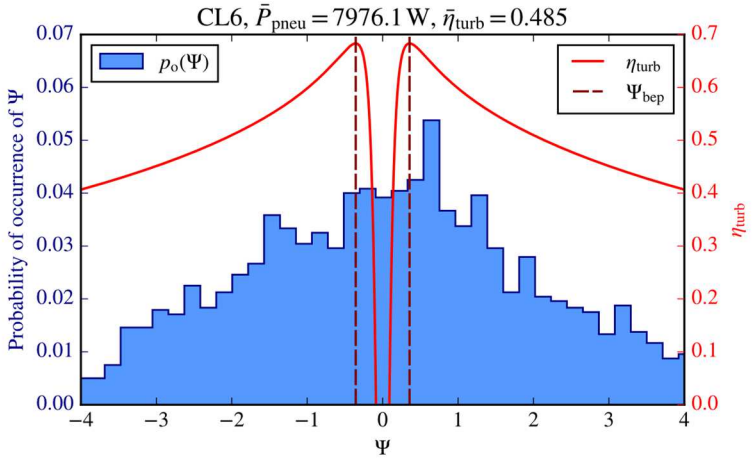

FIGURE 76 - PROBABILITY OF OCCURRENCE OF THE DIMENSIONLESS PRESSURE HEAD Ψ CONCERNING A TEST OF CL6 PERFORMED IN THE SECOND CAMPAIGN.

6.7.1.2.2 PTO EFFICIENCY IN PHASE II

The following comparison includes all the tests made during the second campaign, from January until the end of June. In total nearly 3360 experiments of ½ h were considered, all CLs considered. Figure 77 highlights these efficiencies for the observed testing period and classified into the different CLs in function of the mean pneumatic power. The plot truncates to average pneumatic power values in the interval [0-20kW] for sake of clarity. Also, tests with pneumatic power lower than 1 kW and generator efficiencies below 15% are not considered. Typically, these tests represent cases were the PTO was operating with almost no resource and are not relevant for the CL comparison. The global analysis considers the entire set of data. The figure draws the general trend on the performance of each control law. Again, a special attention is requested by the reader when analysing these results. Indeed, the actual PTO is sized for the next sea trials on the Marmok A5. The turbine diameter does not provide optimal damping in the Mutriku air chamber, and the generator here is oversized compared to the resource in Mutriku.

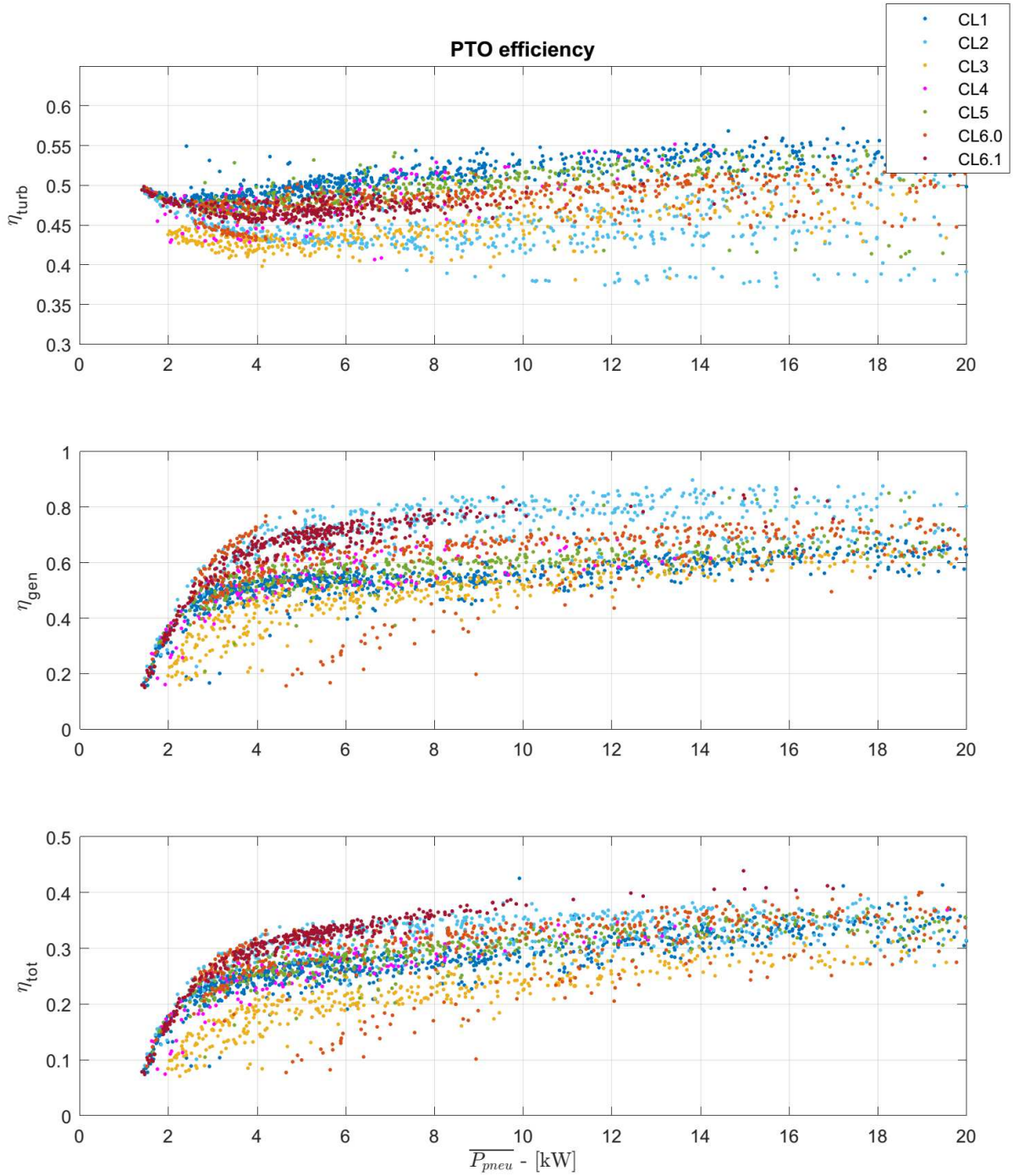

FIGURE 77. EFFICIENCIES OF THE BIRADIAL TURBINE AND GENERATOR IN PHASE II

The following boxplots allow a deeper analysis on each of the PTO efficiencies for all the control laws. In Figure 78, we are focusing on the turbine efficiency. The best algorithm is CL1 with an average efficiency over 51% then followed by CL5, CL6.0 and the latching CL4, are almost ending in a draw. CL2 is slightly higher than the latching strategy CL3. Looking at the maximum values, we can state that there is still room for improvement and if perfectly tuned for any wave condition, the best algorithms could reach efficiencies of almost 60%.

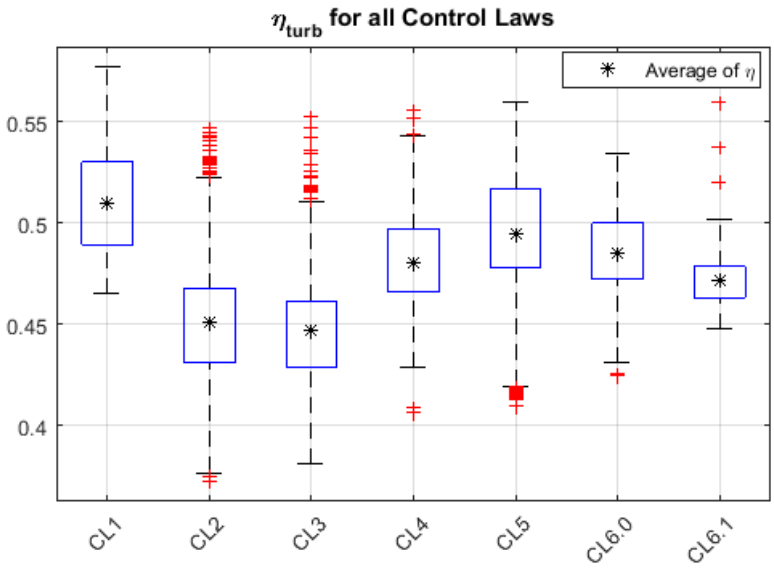

FIGURE 78. TURBINE EFFICIENCY FOR EACH CL

When focusing on the generator efficiency, this time the most efficient CL is #2, followed by CL6.1 and 6.0. The advantage brought by CL2 is that it allows more stable torque extraction. Knowing that the generator efficiency is a product of speed and torque, this behaviour reaches a better operational range of the generator. In the predictive CL6.1, the algorithm performs a global optimisation taking into account both the turbine and generator efficiency. Finally, in CL6.0 the $T - \Omega$ curve has been designed only with generator considerations. Comparing both Figure 78 and Figure 79, one can observe the stronger disparity of efficiency in the generator in respect to the turbine.

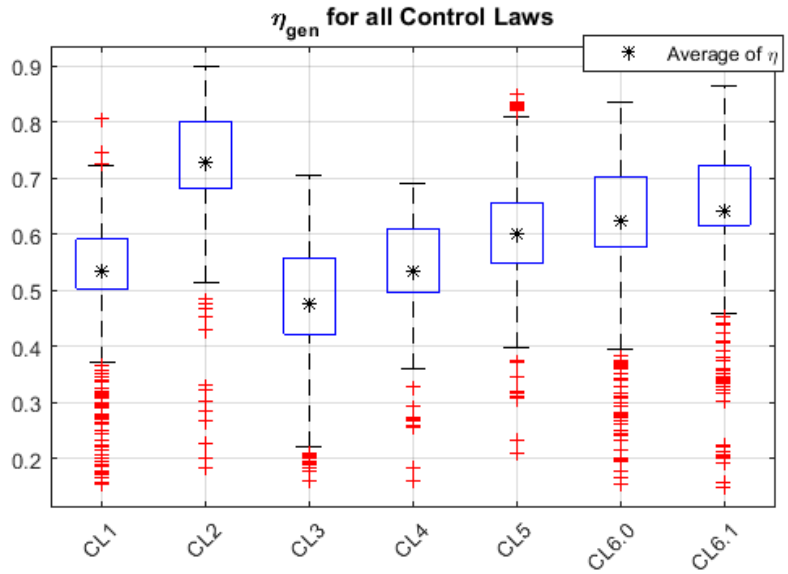

FIGURE 79. GENERATOR EFFICIENCY FOR EACH CL

Figure 80 presents the total PTO efficiency. The best algorithm is finally CL2, followed by CL6.1, CL6.0 and CL5. Note that they were the most performing ones when focusing on the generator efficiency. Meanwhile, CL1 maximised the turbine efficiency, the lack of consideration for the generator clamps its performance. The two latching controllers were not expected to be efficient in the Mutriku plant. This is reinforced when looking at these results of CL3. Still CL4 needs to be tested in the buoy offshore and presents a total efficiency slightly lower than CL1.

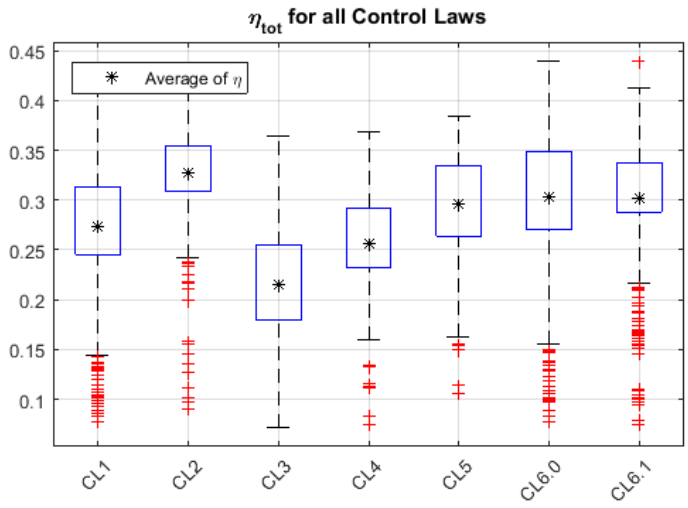

FIGURE 80. TOTAL PTO EFFICIENCY FOR EACH CL

There is less disparity between the CL regarding the turbine efficiency than the generator one. This proves that, regardless the complexity of the controller, this turbine operates at acceptable ranges. This was to be foreseen when looking at the turbine characteristic curves but operational results strengthen this good behaviour. However, controlling the generator seems more challenging and few CL set it at more efficient operation ranges. Also, this is due to the fluctuating wave resource. Conventional generators are not designed for this type of behaviour.

One conclusion of this analysis is that in the design of controllers, the turbine efficiency is often given prime priority to maximise the prime mover power capture. On the other hand, the efficiency of the generator is left aside. The ranking established when looking only at the turbine efficiency is somewhat shuffled when considering the generator. Any controller should be designed including all the components contributing to the energy conversion.

As a summary of the performance analysis, Table 20 presents global figures of efficiencies for each control law.

TABLE 20. GLOBAL PTO EFFICIENCY FOR ALL CLS DURING PHASE II

	CL1	CL2	CL3	CL4	CL5	CL6,0	CL6,1	Best
Eff Turbine	50.99 %	45.08 %	44.71 %	48.00 %	49.47 %	48.51 %	47.16 %	CL1
Eff Generator	53.45 %	72.86 %	47.61 %	53.31 %	60.03 %	62.30 %	64.18 %	CL2
Eff Total	27.39 %	32.71 %	21.44 %	25.68 %	29.67 %	30.28 %	30.22 %	CL2

6.7.2 RELIABILITY

Table 21 shows the summary of operation values of each CL in high operation conditions (high speed, generator overload and high temperature). Globally the common supervisory control in charge of the PTO safety performs well. It prevents turbine overspeed and torque higher than the nominal. All CL keeps the rotational speed below 2530 rpm. The peak-power control of CL1 operates to limit the control torque in order not to overshoot the generator power in comparison with other CLs. On the contrary, CL6.0 operates the PTO at highest load ratios.

TABLE 21. SUMMARY OF EXTREME OPERATING VALUES

	CL1	CL2	CL3	CL4	CL5	CL6.0	CL6.1
Overspeed (Ω > 230 rad/s)							
% of time in overspeed	0.022	0.057	0.056	0.006	0.117	0.051	0
t < 10 s	65	78	78	4	91	57	2
10.1 < t < 30 s	4	9	12	1	24	17	0
t > 30.1	0	0	0	0	5	2	0
Maximum speed (rad/s)	263.99	262.74	264.20	249.02	262.98	264.93	232.35
Overload in Power (P > 30 kW)							
% of time in overload	0.003	0.56	0.016	0.009	0.44	0.69	0.004
Number of times reached overload	24	152	65	18	101	199	9
t < 10 s	24	69	63	18	63	84	9
10.1 < t < 30 s	0	33	2	0	12	51	0
t > 30.1	0	50	0	0	26	64	0
Maximum power (kW)	33.83	46.95	46.37	41.5	46.83	47.1	37.11
Overload in Torque (T > 200 Nm)							
Number of times reached overload	0	0	0	0	0	0	0
Maximum torque (Nm)	152.20	200	200	179.28	200	200	200
Overtemperature (T > 70 °C)							
Number of times reached	0	0	0	0	1	0	0
Maximum temperature (°C)	65.2	68.10	66.40	57.50	73.10	68.10	58.09

Table 22 presents results to compare the reliance of the HSSV and gathers the number of individual test during when the valve was closed more than 10% of the time for sea states higher than $H_s = 1.6$ m. In this analysis, we want to understand how the CL relies on the HSSV during energetic SS. The latching strategies are away of the analysis because of the nature of the CL that needs to actuate the valve. Also, CL6.1 is not represented because there no SS above the studied H_s.

TABLE 22. HSSV RELIANCE

CL1	CL2	CL3	CL4	CL5	CL6.0
25	4	183	7	4	1

CL1 is the CL that most relies on the HSSV, this is a consequence of the peak-power control. While avoiding generator overloads, the control torque is not high enough to break the turbine and the rotational speeds reach the threshold ordering the activation of the HSSV. The energy captured in the OWC has to be dissipated.

6.7.3 POWER QUALITY

Table 23 summarises the main indicators used for evaluating the quality of electrical power; the variations of power levels using the standard deviation; and the Pk2avg that indicates the maximum power in respect to the average production. Both parameters are represented in function of the average electrical power and for both the generator and the grid power.

As it can be seen, the better power quality ratings are found with CL1, CL3 and CL4 as they present the lower value of mean standard deviation, both in generator power as well as in the grid ones. The higher peak power values are found in CL2, CL5 and CL6.0. Focusing on the max Pk2avg all CL ends up in a draw with high values. When analysing the individual figures in the subsections Power Quality for each CL, these values take place in low average powers. The consequence on the grid is thus minimal.

TABLE 23. MEAN AN MAX VALUES OF STANDARD DEVIATION AND PEAK TO AVERAGE OF

	CL1	CL2	CL3	CL4	CL5	CL6.0	CL6.1
Generator Power							
Mean standard deviation	1.85	3.96	2.05	1.68	3.07	4.06	3.58
Max standard deviation	5.93	11.09	6.01	5.86	11.33	12	11.91
Mean Peak to average	4.98	7.35	3.96	8.15	4.60	4.26	3.59
Max Peak to average	11.44	11.85	11.85	11.78	11.88	12	11.93
Grid Power							
Mean standard deviation	2.16	3.81	2.05	1.87	3.34	3.85	3.23
Max standard deviation	5.55	11.84	6.01	5.51	11.88	12	11.95
Mean Peak to average	2	10.36	4.27	9.90	7.85	2.71	0.58
Max Peak to average	11.51	11.99	11.91	11.86	11.96	12	11.93

6.7.4 EVALUATION CRITERIA

Each CL will be evaluated according to the criteria shown in Table 24, with a ranking number from 1 to 5 (1 = worst; 5 = best). The evaluation criteria are the following:

A – Ease of implementation: It refers to the necessities of hardware, sensors or processing requirements. It is described in Section 6.1 and then for all the CL in its respective Implementation subsection. For example, CL1 represents a few lines of codes in the PLC, best case. On the opposite, the predictive CL6.1 needs an external CPU to run and runs the numerical model of the plant based on inputs from the plant and the wave elevation measurement, worst case.

B – Reaction time: referred to the speed of execution of the code. 100 ms cycle time of PLC, the time of execution should be lower. The algorithms directly implemented into the PLC have the fastest response time, best score. On the opposite, those running on the external CPU are more subjected to delays due to data transfer and/or process

time. For CL6.1 for example, the online optimisation took around 4 PLC cycle time, this is the worst-case scenario.

C – Power production (kW) and PTO efficiency (%): It is related to the performance of each CL and refer to the section 6.7.1. The best performance will have the best score.

D – Power quality and grid integration compliances: The power quality is only assessed looking at electrical power peaks. A CL allowing high peaks or showing high power variations for significant load ratio is rated 1. See Power Quality section of each CL.

E – Reliability: It is the ability to compute and apply the control action when needed without any fault and by keeping the PTO integrity. All the CLs present values inside the operational ranges stated by the PTO manufacturer. Moreover, no failure was detected during the second campaign. Thus, this criterion can be evaluated in potential risk of damaging the PTO. The comparison is only based on extremal operational values of the generator power, the best ranking being the lowest maximal electrical power.

F – Sensitivity to data acquisition quality: It is the capacity of the control to run correctly with low-quality data. If the CL only works properly with high quality of data and relies on numerous inputs, its grade is 1. On the contrary, an algorithm able to perform with few inputs regardless the data quality has the highest grade. See the Implementation section on each CL.

G – Safety valve reliance: This is the ability of the controller to remain within operating constraints avoiding activation of the safety valve. The latching controllers are out of scope for this analysis.

TABLE 24. SCORING OF CONTROL LAWS EVALUATION CRITERIA

		CL1	CL2	CL3	CL4	CL5	CL6.0	C6.1	CL7
A	Ease of implementation	5	5	4	3	2	5	1	1
B	Reaction time	5	5	5	4	4	5	2	N/A
C	Production and PTO efficiency	3	5	1	2	4	4	5	N/A
D	Power quality	5	2	4	5	3	2	3	N/A
E	Reliability	5	3	3	4	3	3	4	N/A
F	Sensitivity to data acquisition quality	5	5	4	4	3	5	2	1
G	Safety valve reliance	2	4	N/A	N/A	4	5	N/A	N/A

7. CONCLUSIONS, LESSONS LEARNT AND RECOMMENDATIONS

The third task of WP4 has covered the implementation and testing in the open-sea Mutriku shoreline wave power plant of seven CLs along one year, operating with the novel biradial turbine developed in WP3. In previous tasks, these CLs had been customised for this scenario and validated with simulations as well as using dedicated dry electrical test rigs. Six adaptive control laws were operative, two of them being latching strategies, and one predictive controller, relying on an online upwave measurement, was tested.

For the performance assessment of these control laws, the wave resource was obtained from three different sources. Two pressure gauges were used for local measurement point, one with an offline data logger and the other with real-time communication; and a sea state estimation from a Simar Point from the institution Puertos del Estado was used when none of the previous were available. There are uncertainties linked to the measurement of the wave elevation using hydrostatic pressure sensors. Still, the installed pressure sensors were the best compromise between accuracy, ease of deployment/maintenance and ability to survive to the harsh Winter season. Therefore, the results are conditioned by these uncertainties but, as this work is dealing with a comparative analysis between the behaviour of CLs, the results are considered as valid. Although it was expected to test one additional predictive CL, it was not possible because it required an accurate estimation of the incoming waves to compute the excitation force that acted on the OWC. The pressure sensor installed at sea-bottom was not able to predict the amplitude of each wave component, and the direction of the wave crest. Without this information, it was not possible to estimate the excitation force with the required accuracy. As such, the control CL7 could not be implemented and tested at the Mutriku power plant.

Regarding implementation, CL4, CL5 and CL6.1 required the use of an additional PC to perform the computation of the control parameters while the rest of CLs are directly programmed in the PLC. Operation results have been analysed in terms of performance, reliability and power quality. While CL1, the base case scenario, was found to offer the best turbine efficiency, when considering the whole conversion chain CL2 offered the best total efficiency because it managed better generator considerations. It has been observed that this one is the fastest to respond to any change in the air chamber before the energy is converted from pneumatic to mechanical power. In the opposite, controllers based on rotational speed (CL1, CL4, CL5 andCL6) are more acting on reaction to the energy coming into the system after it is transformed into mechanical power. In terms of electrical power production, the predictive CL6.1 outperformed the other laws with an increase in power production by a global average of more than 30% in respect to CL1. This controller could only be tested in a limited number of sea states due to the late installation of the real-time wave elevation sensor. CL2 produced over 20% more electrical power than CL1. On the contrary, and as expected after the numerical studies of task 4.1, the latching strategies were ineffective. Since the water column

hydrodynamic response when analysing the RAO predicts a flat response with resonance conditions for wave periods between 8 to 18s. Under these conditions, latching control is ineffective thus phase control could not force resonance condition. Nonetheless, numerical simulations prove this type of control strategy may be quite effective in two degree-of-freedom devices such as the one that will be used in the next phase of the project.

Highest values of turbine average efficiency were obtained during the first campaign. This was due to poor selection of the CL1 and CL5 control parameters for the tests performed during the second campaign. Results also show that PTO performance cannot be optimized without looking at the generator side, especially when the generator is working at small loads.

The relatively low average generator efficiencies observed in the second campaign are not surprising since the generator was selected to fit the offshore resource and the production of the Marmok A5. Its nominal capacity is 30 kW while those coupled to the Wells turbines already installed are 18.5 kW rated power. When analysing the PTO performance, the reader is asked to remember that fact. In respect to WP4, the Mutriku testing phase allows to validate the feasibility of implementing these algorithms and operate the PTO safely. Also, this stage allows to have a hint about the most promising control strategies to be soon integrated in the Marmok A5.

During this one-year period of testing the biradial turbine at Mutriku valuable experience has been gained. The following items summarise the positive aspects that can serve as recommendations for future projects and also presents the challenges faced along the way.

- Reliable data acquisition and database access. When dealing with experimental work, operational data generated during the tests are of paramount importance. Operational data were collected and gathered in a cloud database accessible by all the partners thanks to developments in WP1. A tool to access the database through MySQL command facilitated the post-processing activities.
- A fully customisable control framework. The PLC control environment was designed so the developers had easy access to the real-time control section which simplified the deployment and customisation of the control algorithms.
- Testing real-time controllers with the innovative biradial turbine. This turbine was specifically manufactured for this project, and although designed for an offshore application on the Marmok A5, the control laws could be validated as well as some special features like the HSSV used for safety and latching control. For the first time, latching algorithms were operational in an OWC plant although there are best fitted for a floating device.
- Need of an accurate numerical model. All the controllers were previously customised with a numerical model based on linear wave theory. This model was as accurate as it could be at that time. Controllers had to be fine-tuned after implementation to correct the model assumptions.

- Generator failure. After a 3 months period, a shortcut in one of the phases damaged the generator. The quality of winding insulation associated with high voltage peaks generated by the electronics seemed to be the source of the failure. Then followed 4 months unavailability time before the PTO was back on operational conditions. On this second phase, the generator never failed, thanks to special care while rewinding and the installation of an electrical filter that forced to re-calibrate the low-level control in the power electronics.
- Reliability on some key operational data. During the tests, drifts in pressure sensors were discovered and had to be cancelled. Luckily the redundancy on these pressure sensors allowed to derive the value of these drifts that are essential to calculate the pneumatic and turbine powers. In addition, the electrical quantities at the input and output of the power electronics were questionable. A measurement campaign with a power analyser was needed to verify these assumptions and collect enough data to calibrate electrical values. Ideally, a torque meter and an electrical power analyser would have been useful to obtain the turbine and generator powers without relying on measurement uncertainties. But physical constraints did not allow the installation of a torque meter in the turbine shaft, and a power analyser was out of scope due to its important cost.
- Delays and failure on the wave elevation sensors. There was a lack of wave resource assessment along all the testing period because of a delay in the installation of the RBR pressure sensor, due to bad weather after obtaining the deployment permit. When the sensor was retrieved, we realised it stopped measuring at half the deployment period. The consequence of the analysis of operational data was the impossibility to group the results over the same resource measurement.
- Delay in the installation of the real-time wave measurement. The Isurki pressure sensor could only be installed during the last month of tests. This allowed a 2-week test of the predictive algorithm CL6.1 between the sensor setup and periods of low energetic seas. On the other end, CL7 could not be tested because of uncertainty on the wave elevation and the high reliance on the perfectly synchronised wave data during its travel between the sensor and the plant.
- Regarding the future tests in the OCEANTEC's Marmok A5 buoy, all the control laws need to be recalibrated due to the different hydrodynamics and available pressure head to the turbine.

8. ANNEX

8.1 GENERAL LAYOUT OF BIRADIAL INSTRUMENTATION IN THE MUTRIKU SCADA

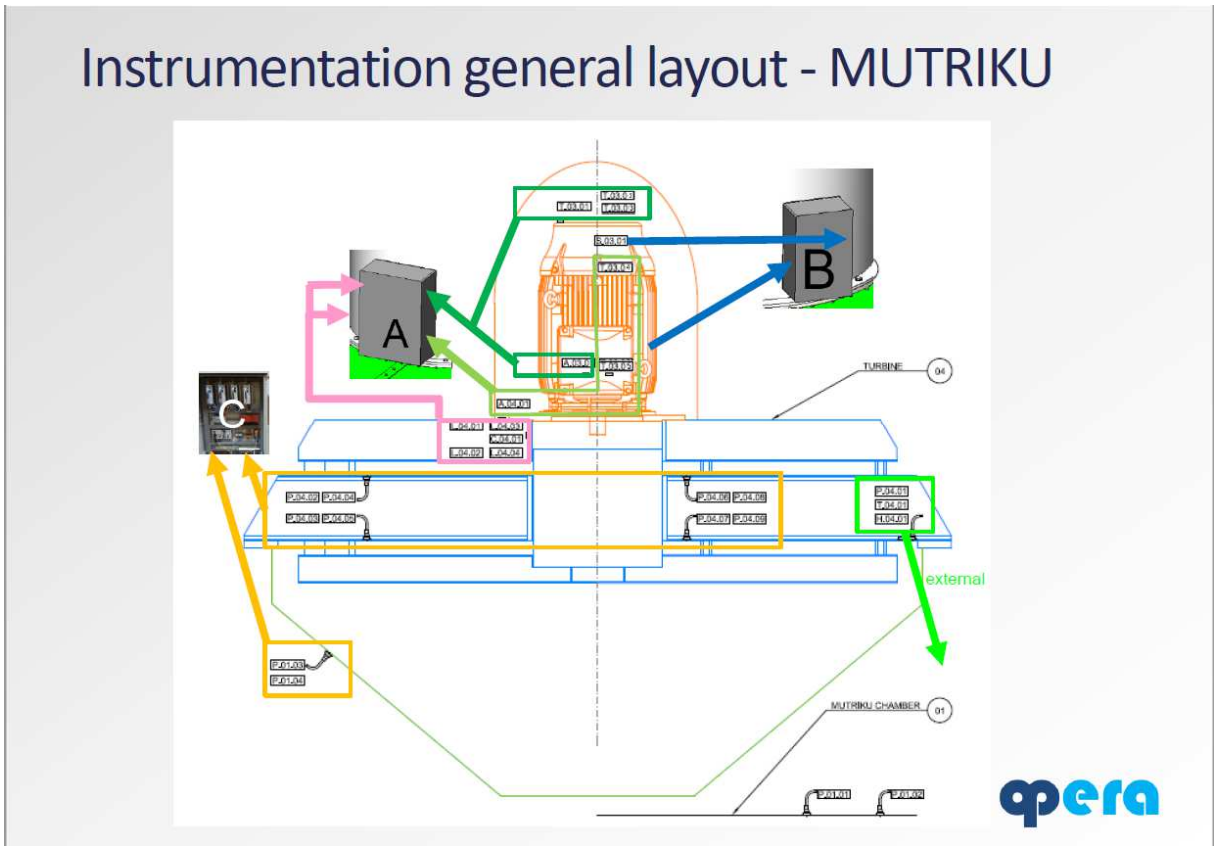

FIGURE 81. INSTRUMENTATION LAYOUT OF THE BIRADIAL TURBINE

8.2 ACCURACY OF PRESSURE SENSOR FOR CL7

In this section, the reason for not implementing CL7 in the Mutriku power plant will be explained. A few points are to be addressed, such as:

- Why the hydrostatic pressure is not the value measured by the pressure sensor measured at sea bottom.
- Correction of the pressure and the uncertainty of the results.
- Computing the tide from the pressure sensor measurements.
- The uncertainty of the angle of the wave crest with respect to the Mutriku breakwater.

8.2.1 WHY THE HYDROSTATIC PRESSURE IS NOT THE VALUE MEASURED BY THE PRESSURE SENSOR INSTALLED AT SEA BOTTOM

The topic addressed in this section has been already discussed in well-known books of Falnes [14] Holthuijsen [19], and Boccotti [20]. For the sake of completeness, the problem is also fully described in this section. The based is the Navier-Stokes equations and the linear wave theory.

Neglecting the viscous term from the momentum balance of the Navier-Stokes equations, it is found that

$$\rho \frac{\partial \mathrm{u}}{\partial t} + \rho \mathrm{u} \cdot \nabla \mathrm{u} = -\nabla p + \rho \mathrm{g} \tag{43}$$

To fully understand the reasoning why the hydrostatic pressure is not the value measured by the pressure sensor installed at sea bottom, let us first consider the case where the velocity $\mathbf{u}$ is zero. Under this condition, and knowing that gravity acceleration has only vertical component, the momentum balance along y (positive upwards) gives

$$\frac{\partial p}{\partial y} = -\rho g \tag{44}$$

Integrating along a vertical line from sea-bottom, $y = -\mathrm{h}$, to the sea-surface, $y = 0$, we get

$$\int_{-\mathrm{h}}^{0} \frac{\partial p}{\partial y}\, \mathrm{d}y = -\int_{-\mathrm{h}}^{0} \rho g\, \mathrm{d}y \tag{45}$$

$$\int_{-\mathrm{h}}^{0} \frac{\partial p}{\partial y}\, \mathrm{d}y = -\int_{-\mathrm{h}}^{0} \rho g\, \mathrm{d}y \tag{46}$$

$$p(0) - p(-h) = -\rho g h \tag{47}$$

$$p(-h) - p_{\mathrm{atm}} = \rho g h \tag{48}$$

Equation 43 is the well-known hydrostatic pressure relation. However, it is only valid under the condition that velocity u is zero. This is not the case of the ocean waves.

Let us now consider the general case where $\mathbf{u}$ is, in general, different from zero. Since the viscous term is assumed zero, we have $\nabla \times \mathbf{u} = 0$ which leads to the potential flow assumption where $\mathbf{u} = \nabla\phi$. The time derivative of the velocity vector is

$$\frac{\partial \mathrm{u}}{\partial t} = \frac{\partial(\nabla\phi)}{\partial t} = \nabla\left(\frac{\partial \phi}{\partial t}\right) \tag{49}$$

yielding the momentum balance along y

$$\frac{\partial}{\partial y}\left(\rho\frac{\partial\phi}{\partial t}+\frac{1}{2}\rho\mathrm{U}\cdot\mathrm{U}\right)=-\frac{\partial}{\partial y}(p+\rho g y) \tag{50}$$

where $\mathbf{g}=-g\nabla y$. Integrating from the sea-bottom $y=-h$ to the free-surface $y=\zeta$ gives

$$\int_{-h}^{\zeta}\frac{\partial}{\partial y}\left(\rho\frac{\partial\phi}{\partial t}+\frac{1}{2}\rho\mathrm{u}\cdot\mathrm{u}\right)\mathrm{d}y=\int_{-h}^{\zeta}-\frac{\partial}{\partial y}(p+\rho g y)\,\mathrm{d}y \tag{51}$$

Resulting:

$$\left(\rho\frac{\partial\phi}{\partial t}+\frac{1}{2}\rho\mathrm{U}\cdot\mathrm{U}\right)\Big|_{-h}^{\zeta}=-(p+\rho g y)|_{-h}^{\zeta} \tag{52}$$

Expanding

$$\rho\frac{\partial\phi}{\partial t}(\zeta)-\rho\frac{\partial\phi}{\partial t}(-h)+\frac{1}{2}\rho\mathbf{u}^2(\zeta)-\frac{1}{2}\rho\mathbf{u}^2(-h)=-p(\zeta)+p(-h)-\rho g\zeta-\rho g \tag{53}$$

We know that $p(\zeta)=p_{\mathrm{atm}}$ and from the boundary condition at the free-surface

$$\frac{\partial\phi}{\partial t}(\zeta)+g\zeta=0 \tag{54}$$

yields

$$p(-h)=p_{\mathrm{atm}}+\underbrace{\rho g h-\rho\frac{\partial\phi}{\partial t}(-h)}_{(a)}+\underbrace{\frac{1}{2}\rho\mathrm{u}^2(\zeta)-\frac{1}{2}\rho\mathrm{u}^2(-h)}_{(b)} \tag{55}$$

Neglecting the term (b) since $O(b)\sim(A/\lambda)\ll 1$, $O(a)\sim(A/\lambda)^2$ and $O(b)\ll O(a)$, gives

$$p(-h)=p_{\mathrm{ATM}}+\rho g h-\rho\frac{\partial\phi}{\partial t}(-h) \tag{56}$$

The velocity potential for a wave of frequency ω_m and amplitude $\tilde{A}_m$ is

$$\phi=\frac{g}{\omega}\frac{\cosh(k(y+h))}{\cosh(kh)}\tilde{A}_m\exp(-(kx-\omega t)) \tag{57}$$

Hereinafter, the tilde denotes a complex value used to include the wave phase. Considering $x=0$ and $y=-h$ at the measuring point results

$$\phi=\frac{g}{\omega_m\cosh(k_m h)}\tilde{A}_m\exp(\omega_m t) \tag{58}$$

The time derivative is

$$\frac{\partial\phi}{\partial t}=-\frac{g}{\cosh(k_m h)}\tilde{A}_m\exp(\omega_m t) \tag{59}$$

and the pressure relative to the local hydrostatic pressure, $p'_{\text{sensor}} = p(-h)'$, measured at the sea-bottom is

$$p'_{\text{sensor}} = p(-h) - p_{\text{atm}} - \rho g h = \frac{\rho g}{\cosh(k_m h)} \tilde{A}_m \exp(\omega_m t) \tag{60}$$

This last equation shows that the wave amplitude $\tilde{A}_m$ measurement, for a given frequency ω_m, based on a pressure sensor installed at sea-bottom requires the knowledge of the wave number. As such, the instantaneous wave height $\zeta(t)$ above the pressure sensor needs to be computed in the frequency domain. Performing a DFT of the pressure sensor signal we get the complex amplitudes

$$\tilde{p}'_m = \frac{1}{n} \sum_{j=0}^{n-1} p'_{\text{sensor}}(t_j) \exp\left(-2\pi \frac{mj}{n}\right) \tag{61}$$

The instantaneous wave height $\zeta(t_j)$ is computed from a IDFT

$$\zeta_j = \sum_{m=-n/2}^{n/2-1} \tilde{A}_m \exp\left(2\pi \frac{mj}{n}\right) \tag{62}$$

where the amplitude for each frequency needs to be corrected as a function of the wave number

$$\tilde{A}_m = \frac{\tilde{p}'_m}{\rho g} \cosh(k_m h) \tag{63}$$

The wave number k_m is evaluated from the dispersion relation

$$\frac{\omega_m^2}{g} = k_m \tanh(k_m h) \tag{64}$$

Note that $k_m = k_{-m}$ since $\omega_m^2 = \omega_{-m}^2$ in the dispersion relation.

Since the ocean waves can be decomposed as a sum linear sinusoidal waves respecting a given spectral distribution, we can compute the absolute pressure at sea-bottom for the crest and for the through, as a function of the period T_m of each component and tide value y_{tide}, from Eq. 55.

$$p_{\text{sensor}} = \pm \frac{\rho g}{\cosh(k_m h)} \left|\tilde{A}_m\right| + \rho h y_{\text{tide}} + p_{\text{atm}} \tag{65}$$

The plus sign is for the crest and the negative for the through. Let us assume a sinusoidal wave with an amplitude modulus of $\left|\tilde{A}_m\right| = 0.05\text{m}$. Probably this value over-estimates the amplitude of each spectral component but allow us to perform a conservative sensitivity analysis, see FFT of Figure 89. Note that the pressure sensor measures the absolute pressure at sea-bottom.

The pressure sensor installed upwave of the Mutriku power has a range of measurement of 0 to 30 mH_20, and a measurement error of 0.1% of the full-range, i.e., about 0.03 mH_20. Converting from mH_20 to Pascal ($p = \rho_w g h$), the measurement range is 0 to 301658 Pa with an error of $\varepsilon_p = 302$ Pa.

At first glance, the sensor specifications seem to be reasonably accurate. Let us check that this not the case. Since there is no information regarding the dynamic response of the sensor as a function of the frequency, let us assume that the measurement error is ε_p across all the frequencies.

Figure 82 plots the resultant absolute pressure at sea-bottom, as given by, for the wave crest and through, as a function of the wave period, for three tide values: $y_{\text{tide}} = 13.8\text{m}$, $y_{\text{tide}} = 10.8\text{m}$ and $y_{\text{tide}} = 7.8\text{m}$. The results plotted show that the pressure fluctuations resulting from the wave oscillations are very small in comparison with the absolute pressure. These differences decreases with the decrease of the wave period.

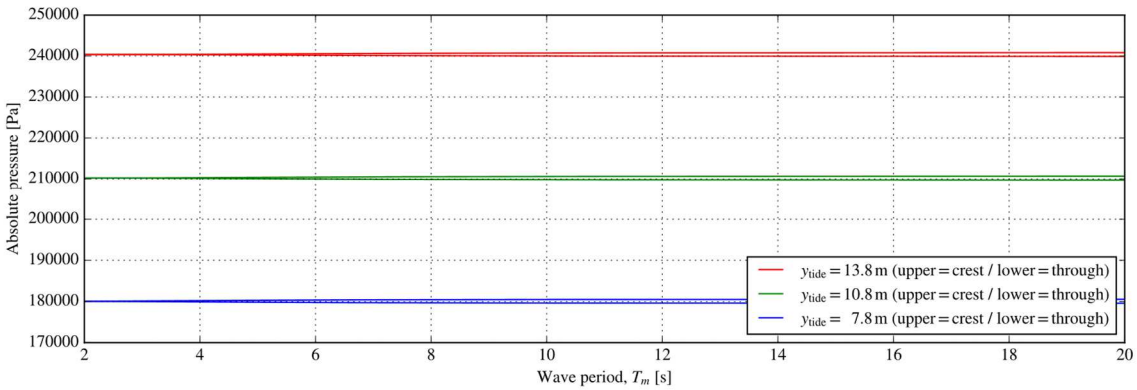

FIGURE 82. ABSOLUTE PRESSURE AT SEA-BOTTOM, AS A FUNCTION OF THE WAVE PERIOD, FOR THREE TIDE VALUES.

Figure 83 plots the relative pressure amplitude at sea-bottom due to the surface waves, together with the error bands of the signals. This figure evidences that, for wave periods below 8s, the pressure sensor is not able to measure anything besides noise. It is even difficult to distinguish the crests from the throughs. For frequencies higher than 8s, the pressure difference between the crest and through is less than 3 times the sensor error, thus limiting the accuracy of the measurements. The low acquisition rate of 4Hz does not allow the improvement of the accuracy through large sample time-averaging. Nevertheless, the pressure sensor is good for measuring the tide, a component with a period of about $T_m \approx 12\text{h}25\text{m}$.

Figure 84Figure 84 is similar to Figure 83Figure 83, but plotting the relative pressure as a function of the wave frequency. The plot shows that the sea-bottom pressure attenuation as a function of the water depth behaves like a low-pass filter.

In conclusion, it is not possible to accurately estimate the instantaneous wave height using a pressure sensor installed the sea-bottom, for the wave periods found on the sea and the values of the water depth of the deployment site.

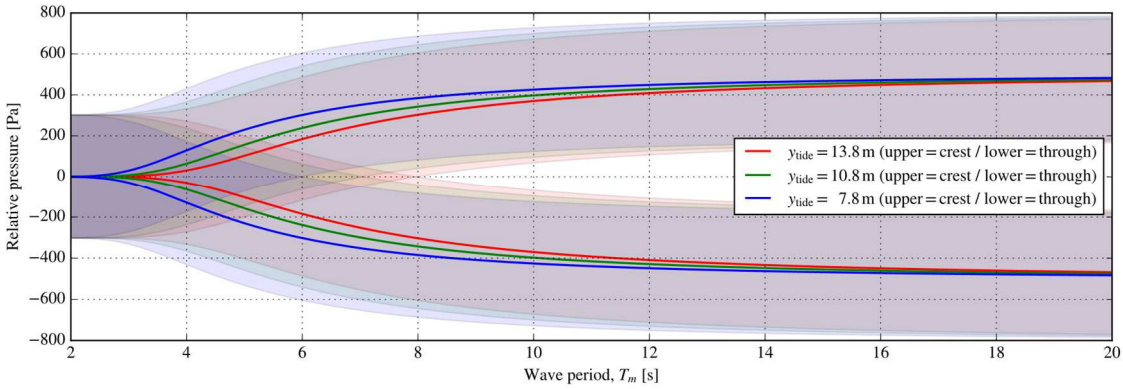

FIGURE 83. RELATIVE PRESSURE AT SEA-BOTTOM, AS A FUNCTION OF THE WAVE PERIOD, FOR THREE TIDE VALUES. THE ERROR BANDS OF THE SIGNALS ARE ALSO DEPICTED.

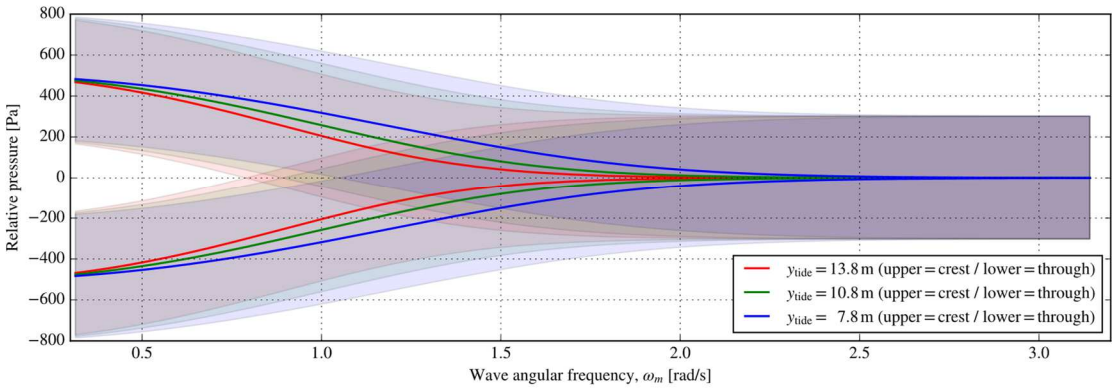

FIGURE 84. RELATIVE PRESSURE AT SEA-BOTTOM, AS A FUNCTION OF THE WAVE FREQUENCY, FOR THREE TIDE VALUES. THE ERROR BANDS OF THE SIGNALS ARE ALSO DEPICTED.

8.2.2 CORRECTION OF THE PRESSURE AND THE UNCERTAINTY OF THE RESULTS

In this section we evaluate the possibility of computing the wave amplitude from sea-bottom pressure measurements, i.e., applying Eq. 58 to determine the amplitude of the wave components. For this purpose, we can calculate the corrected value of the amplitude considering a pressure oscillation equal to the error of the pressure sensor.

A measurement of $\varepsilon_p = 302$ Pa corresponds, under hydrostatic hypotheses, to a water level error of

$$\varepsilon_h = \frac{\varepsilon_p}{\rho_w g} = 0.03 \text{ m} \tag{66}$$

Replacing ε_p in Eq. 58, we get the corrected water level error $\tilde{\varepsilon}_h$ as a function of the wave number k_m and tide level y_{tide}

$$\tilde{\varepsilon}_h(k_m, y_{\text{tide}}) = \frac{\varepsilon_p}{\rho g}\cosh(k_m y_{\text{tide}}) \quad (67)$$

Equation 62 allows us to assess the effect of the correction term $\cosh(k_m y_{\text{tide}})$, as depicted in Figure 85. Figure 86 plots the relative error E_r of $\tilde{\varepsilon}_h(k_m, y_{\text{tide}})$ with respect to hydrostatic assumption ε_h

$$E_r = \frac{\tilde{\varepsilon}_h(k_m, y_{\text{tide}}) - \varepsilon_h}{\varepsilon_h} \quad (68)$$

The curves plotted in Figure 85 show that the water motion acts as a low pass filter that damps pressure fluctuation for wave periods T_m lower than 14s. As such, it is almost impossible to accurately measure any wave height based on a sea-bottom installed pressure sensor for the wave periods of interest at Mutriku power. In other words, measurements report noise. Nevertheless, for larger periods, such as the ones associated with the tide (about 12 hours and 25.2 minutes), the error associate with these measurements is almost zero.

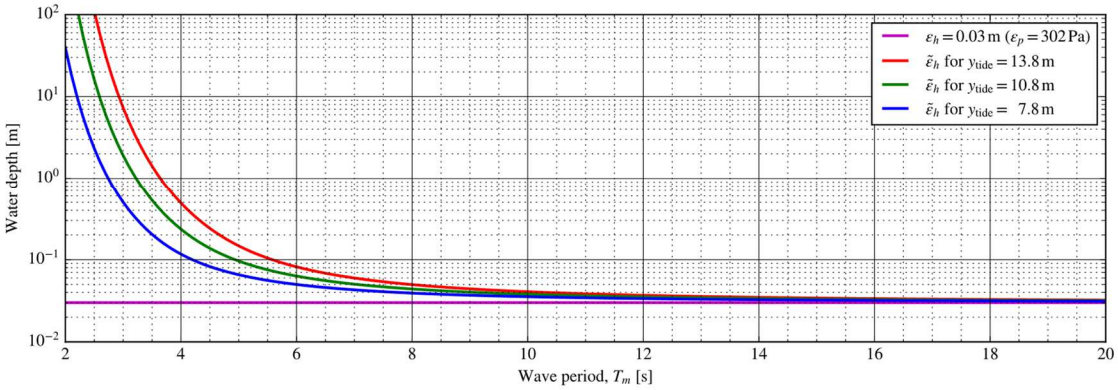

FIGURE 85. COMPARISON OF THE WATER LEVEL AS COMPUTED USING THE HYDROSTATIC PRESSURE ASSUMPTION WITH THE CORRECTED VALUE OBTAINED FROM EQ. 62

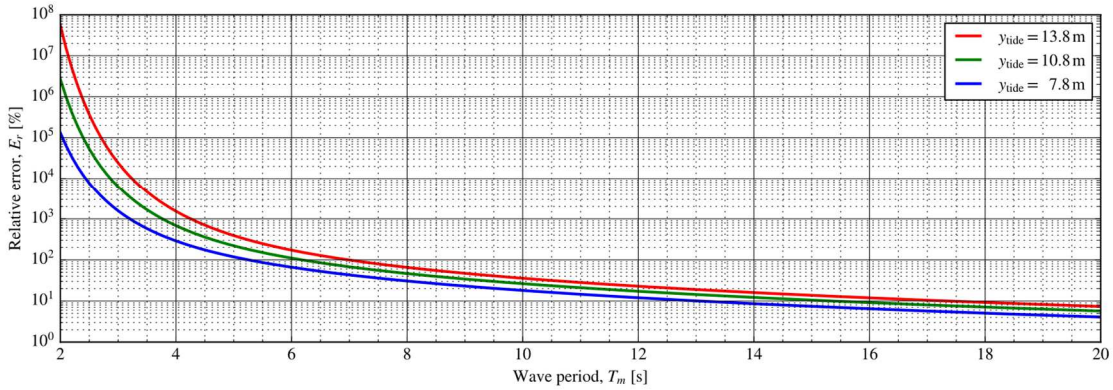

FIGURE 86. RELATIVE ERROR ε_r OF THE CORRECTED WATER LEVEL, WITH RESPECT TO THE HYDROSTATIC ASSUMPTION, AS FUNCTION OF THE TIDE.

As shown in the plots, for wave periods lower than 14s, the error introduced by computing the wave height using sea-bottom pressure measurements is too large to the results present any valuable information. Note that the energy of each wave component is proportional to the square of the amplitude.

8.2.3 COMPUTING THE TIDE FROM THE PRESSURE SENSOR MEASUREMENTS

As shown in the previous sections, the wave tide can be accurately predicted with the pressure sensor. The tide can be computed using a centred non-causal zero-phase low-pass filter. An example of such a filter, with 2801 points, is depicted in Figure 87. Figure 88 shows an example of raw wave data, the tide as computed with the low-pass filter of Figure 87, and the wave data with the subtraction of the tide values.

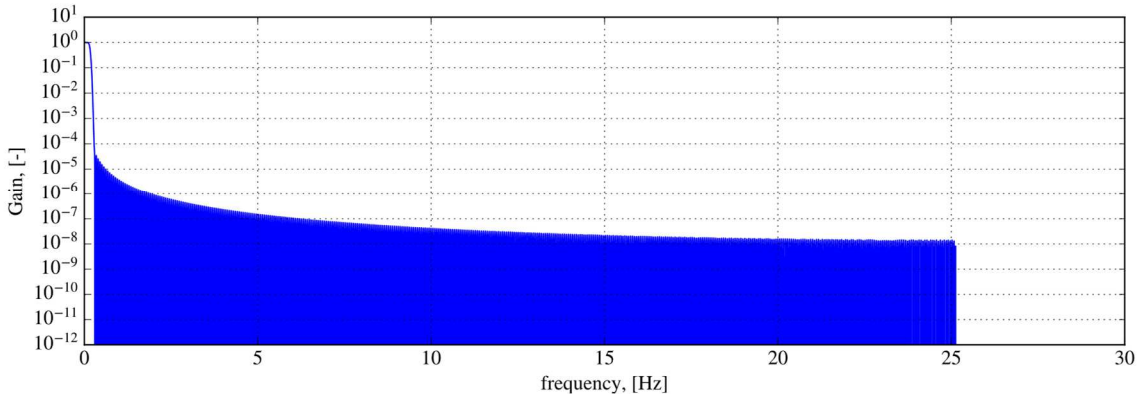

FIGURE 87. NON-CAUSAL ZERO PHASE LAG FILTER WITH 2801 POINTS.

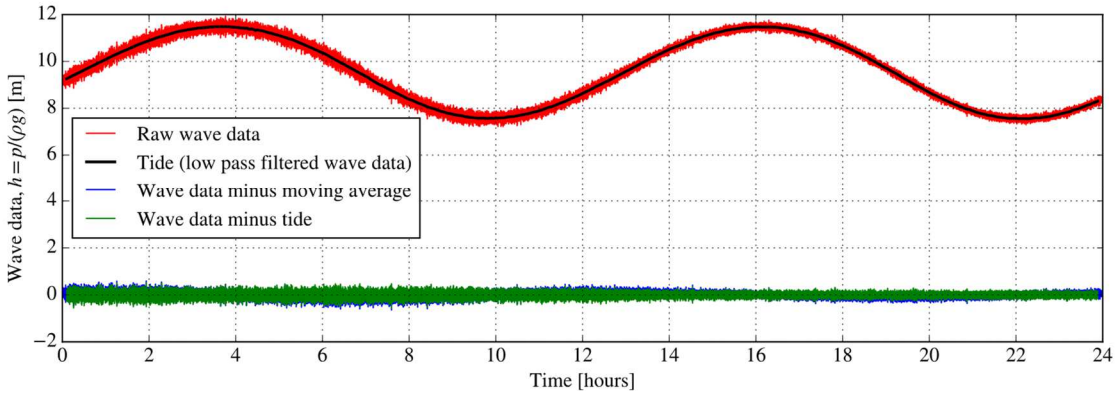

FIGURE 88. RAW WAVE DATA, TIDE COMPUTED WITH THE NON-CAUSAL ZERO LAG PHASE LOW PASS FILTER AND WAVE DATA WITH THE SUBTRACTION OF THE TIDE VALUES.

Figure 89 shows the Fast Fourier Transform of the wave data minus the tide, as computed with the non-causal zero lag low-pass filter of Figure 87, showing that for zero frequency the amplitude is zero. On the other hand, Figure 90 shows an analogous plot of the Fast Fourier Transform of the wave data minus the tide, as computed with a moving average, where it is clear a peak at zero frequency. This effect is also evident in Figure 88, where both signals (without the tide) do not overlap entirely. As such, the moving average may not be the best approach to estimate the wave height.

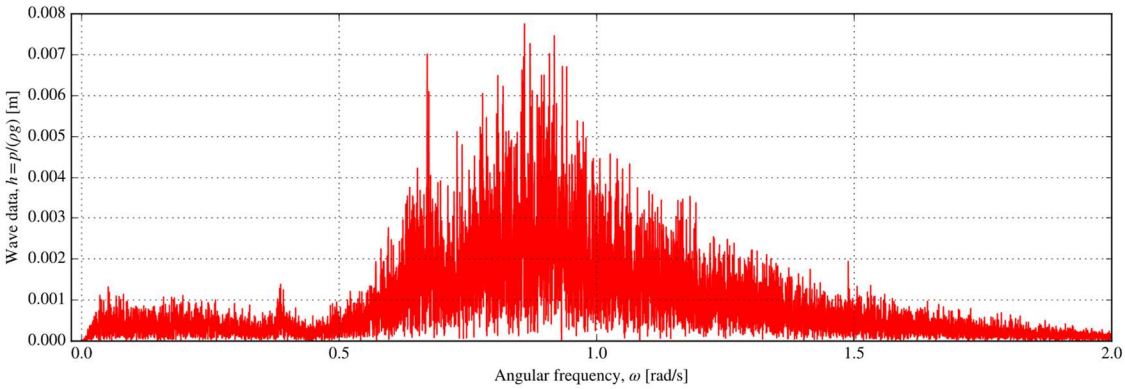

FIGURE 89. FFT OF RAW DATA MINUS THE TIDE AS COMPUTED WITH THE CENTRED NON-CAUSAL ZERO-PHASE LOW PASS FILTER.

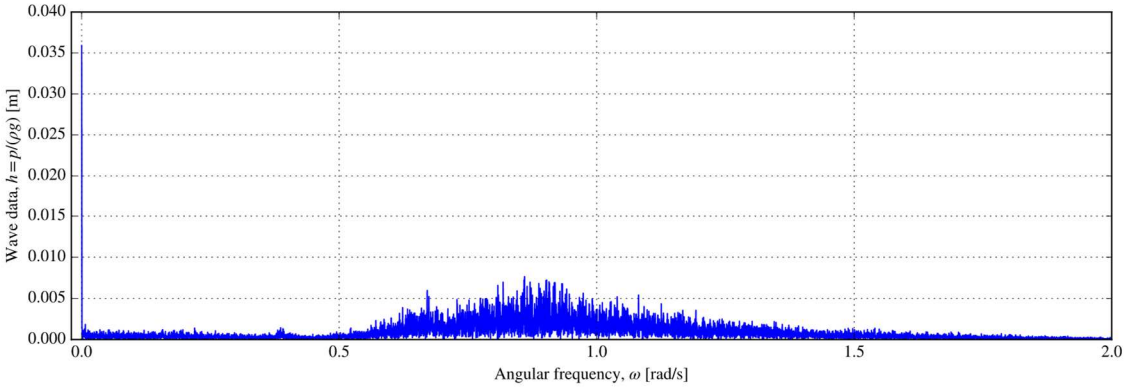

FIGURE 90. FFT OF RAW DATA MINUS THE TIDE AS COMPUTED WITH THE MOVING AVERAGE.

8.2.4 THE UNCERTAINTY OF THE ANGLE OF THE WAVE CREST WITH RESPECT TO THE MUTRIKU BREAKWATER

Another problem faced by an algorithm aiming to predict the waves is the uncertainty about the wave crest angle. Even if the pressure sensor could be used to estimate the wave height accurately, it is not possible to compute the wave crest angle with only one sensor, Figure 91. As a result, different wave crest directions will result in different time intervals between the instant of the pressure sensor measurements and the instant when the wave hits the power plant.

To accurately predict the wave crest angle, with respect to the power plant, it is necessary to have two or more sensors. Another associated problem is the uncertainty about the exact location of the sensor.

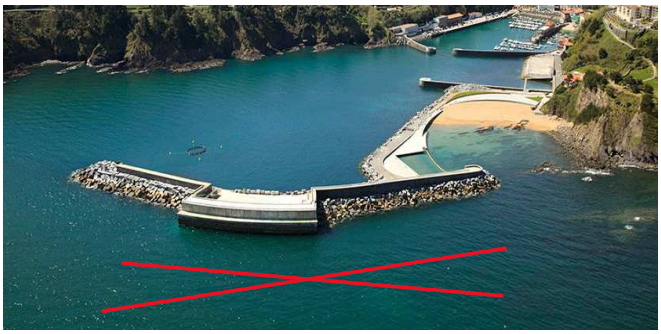

FIGURE 91. THE MUTRIKU POWER PLANT AND TWO POSSIBLE DIRECTIONS OF THE WAVE CREST.

9. REFERENCES

[1] Y. Torre-Enciso, I. Ortubia, L. I. López de Aguileta, and J. Marqués, 'Mutriku Wave Power Plant: from the thinking out to the reality', in *Proceedings of the 8th European Wave and Tidal Energy Conference*, 2009, pp. 319–329.

[2] Y. Torre-Enciso, J. Marqués, and L. I. López de Aguileta, 'Mutriku. Lessons learnt', in *Proceedings of the 3rd International Conference on Ocean Energy*, 2010.

[3] I. Heras-Saizarbitoria, I. Zamanillo, and I. Laskurain, 'Social acceptance of ocean wave energy: A case study of an OWC shoreline plant', *Renew. Sustain. Energy Rev.*, vol. 27, pp. 515–524, Nov. 2013.

[4] 'RBRvirtuoso'. [Online]. Available: https://rbr-global.com/products/standard-loggers/rbrvirtuoso-rbrduo.

[5] 'Deliverable D1.1 OPERA - Process Instrumentation Definition'. Jul-2016.

[6] 'Isurki CNC4200-MT3'. [Online]. Available: http://www.isurki.com/images/fichas-tecnicas/cnc4200_mt3-datasheet.pdf.

[7] 'Puertos del Estado - Oceanografía'. [Online]. Available: http://www.puertos.es/es-es/oceanografia/Paginas/portus.aspx.

[8] A. F. O. Falcão and L. M. C. Gato, '8.05 Air Turbines', 2012.

[9] 'Deliverable D3.3 OPERA - Turbine and electrical equipment performance and reliability in shoreline OWC wave plant'. Jul-2018.

[10] 'Deliverable D4.1 OPERA - Customisation of control laws'. Jul-2017.

[11] J. C. C. Henriques, A. F. O. Falcao, L. M. C. Gato, J. M. Lemos, and J. C. C. Portillo, 'Latching and Peak-Power Control of an Oscillating Water Column Based on a Discontinuous Galerkin Method', presented at the 12th EWTEC, Cork, Ireland, 2017, p. 9.

[12] J. C. C. Henriques, J. M. Lemos, V. Eça, L. M. C. Gato, and A. F. O. Falcao, 'A Discontinuous Galerkin Method for optimal and sub-optimal control applied to an oscillating water column wave energy converter', presented at the he 20thWorld Congress of the International Federation of Automatic Control, Toulouse, France, 2017.

[13] F.-X. Faÿ, M. Marcos, and E. Robles, 'Novel Predictive Latching Control for an Oscillating Water Column Buoy', presented at the 12th EWTEC, Cork, Ireland, 2017.

[14] J. Falnes, *Ocean waves and oscillating systems*. Cambridge University Press, 2002.

[15] B. Guo, R. J. Patton, S. Jin, and J. Lan, 'Numerical and experimental studies of excitation force approximation for wave energy conversion', *Renew. Energy*, Mar. 2018.

[16] J. C. C. Henriques, J. M. Lemos, L. Eça, L. M. C. Gato, and A. F. O. Falcão, 'A high-order Discontinuous Galerkin Method with mesh refinement for optimal control', *Automatica*, vol. 85, pp. 70–82, Nov. 2017.

[17] 'OPERA WP1 Technical Note on Database Column correlation to Process Instrumentation'. Jul-2018.

[18] Yokogawa, 'WT1600 Digital Power Meter - User's Manual'. .

[19] Puertos del estado, 'Conjunto de datos SIMAR'. 25-Jun-2015.

[20] J. C. Henriques, J. C. Chong, A. F. Falcão, and R. P. Gomes, 'Latching Control of a Floating Oscillating Water Column Wave Energy Converter in Irregular Waves', in *ASME 2014 33rd International Conference on Ocean, Offshore and Arctic Engineering*, 2014, p. V09AT09A017–V09AT09A017.

[21] J. C. C. Henriques, L. M. C. Gato, A. F. O. Falcão, E. Robles, and F.-X. Faÿ, 'Latching control of a floating oscillating-water-column wave energy converter', *Renew. Energy*, vol. 90, pp. 229–241, May 2016.

[22] L. H. Holthuijsen, *Waves in Oceanic and Coastal Waters*. Cambridge: Cambridge University Press, 2007.

[23] P. Boccotti, *Wave mechanics and wave loads on marine structures*. Amsterdam Boston Heidelberg: Butterworth-Heinemann, an imprint of Elsevier, 2015.